

Bottom Quark-Antiquark Production And Mixing In
Proton-Antiproton Collisions

A Dissertation
Presented to the Faculty of the Graduate School
of
Yale University
in Candidacy for the Degree of
Doctor of Philosophy

By
Zhaoou Yu

Dissertation Director: Michael Schmidt

March 2003

UMI Number: 3084391



UMI Microform 3084391

Copyright 2003 by ProQuest Information and Learning Company.

All rights reserved. This microform edition is protected against
unauthorized copying under Title 17, United States Code.

ProQuest Information and Learning Company
300 North Zeeb Road
P.O. Box 1346
Ann Arbor, MI 48106-1346

ABSTRACT

Bottom Quark-Antiquark Production And Mixing In Proton-Antiproton Collisions

Zhaoou Yu

Yale University

March 2003

The studies of bottom quark-antiquark production in proton-antiproton collisions play an important role in testing perturbative QCD. Measuring the mixing parameter of B mesons imposes constraints on the quark mixing (CKM) matrix and enhances the understanding of the Standard Model. Multi-GeV $p\bar{p}$ colliders produce a significant amount of $b\bar{b}$ pairs and thus enable studies in both of these fields.

This thesis presents results of the $b\bar{b}$ production cross section from $p\bar{p}$ collisions at $\sqrt{s} = 1.8$ TeV and the time-integrated average $B\bar{B}$ mixing parameter ($\bar{\chi}$) using high-mass dimuon data collected by CDF during its Run IB. There is a high concentration of muon pairs from inclusive semileptonic B decays in this data set. We take advantage of the long lifetime property of B hadrons and isolate the muons from B decays by studying the displacement of the muon pair trajectories. We use an Unbinned Maximum Likelihood Fitting method to fit the two dimensional impact parameter distribution for dimuons and thus obtain the fraction of dimuons that are from $b\bar{b}$. With this $b\bar{b}$ fraction and accounting for the detector acceptance and efficiencies, we obtain the $b\bar{b}$ production cross section as a function of the minimum transverse momenta of the b quarks. We also obtain the B mixing parameter by comparing the numbers of like-sign $b\bar{b}$ dimuons and opposite-sign $b\bar{b}$ dimuons.

The measured $b\bar{b}$ production cross sections are systematically higher than the Next-To-Leading-Order QCD predictions but are consistent with the CDF Run IA results [1]. The measured average B meson mixing parameter is $0.153 \pm .019$ and is within two standard deviations of the world average value.

Acknowledgments

My road to a Ph. D. degree was a long but exciting experience. There are many people to whom I would like to express my gratitude. First of all, I would like to thank my advisor Michael Schmidt. He showed me a great example of being a serious and responsible scientist and man. Also, his patience and understanding of my choices were really great help to a graduate student in a foreign country. I would also like to thank Colin Gay, Andrew Martin, Henry Kasha and other Yale colleagues. They made my research at Yale a treasurable memory that I will never forget. I would like to thank Jonathan Lewis, Kevin Pitts, Intae Yu and other colleagues in Fermilab. Without their help I would not be able to do my research in such a large collaboration. Last but not least, I would like to thank my family and my girlfriend. Their understanding and support accompanied me and encouraged me throughout the course to my degree. It is my honor to be able to say here: "Thank you all!"

Contents

Acknowledgments	ii
1 Introduction	1
2 Theory	3
2.1 Standard Model	3
2.2 Heavy Quark Production	5
2.3 $B\bar{B}$ Mixing Parameter	11
2.3.1 CKM Matrix	11
2.3.2 $B^0\bar{B}^0$ Mixing	14
3 Apparatus	17
3.1 Overview of the Apparatus	17
3.2 Accelerator	18
3.3 Collider Detector at Fermilab (CDF)	24
3.4 Central Tracking Chamber (CTC)	26
3.5 Silicon Vertex Detector (SVX')	29
3.6 Beam-Beam Counters	35
3.7 Central Muon Systems	35
3.8 Trigger System and Data Acquisition System	41
3.8.1 Level 1 Trigger	41
3.8.2 Level 2 Trigger	43
3.8.3 DAQ	44
3.8.4 Level 3 Trigger	44

4	Method	45
4.1	Goals and Data Selection	45
4.1.1	$b\bar{b}$ Production Cross Section	46
4.1.2	The Time Integrated Mixing Parameter $\bar{\chi}$	47
4.2	Impact Parameter Fitting Method	50
5	Data	62
5.1	Dimuon Data	62
5.1.1	The Sources of Dimuon Data.	62
5.1.2	Online Data Selection Criteria	65
5.1.3	Offline Data Selection Criteria	67
5.1.4	Studies on Dimuon Data Offline Selection	68
5.2	Monte Carlo Data	74
5.2.1	Software Packages and Parameters Selection	74
5.2.2	The Selection Criteria for the Monte-Carlo Data	80
5.2.3	Dimuon Trigger (DIMUTG)	81
5.3	Track Data from Prompt Source	81
6	The Measurement of $b\bar{b}$ Production Cross Section in $p\bar{p}$ Collision at $\sqrt{S} = 1.8$ TeV	84
6.1	Introduction	84
6.2	The Acceptance	87
6.2.1	Monte Carlo Weights for the Acceptance	88
6.2.2	Rapidity Constraints in Our Monte Carlo Simulations	89
6.2.3	The Results for the Detector Acceptances	91
6.2.4	A Comparison to BGenerator	91
6.3	Detector Efficiency ϵ_{CDF}	92
6.3.1	Using Upsilon's in the Efficiency Calculations	93
6.3.2	ϵ_{SVX}	94
6.3.3	ϵ_{CMP}	94
6.3.4	The Level 3 Efficiency ϵ_{L3}	97
6.3.5	Other Efficiencies	99

6.3.6	Accounting for Fake Tracks	100
6.3.7	Calculating the Cross Sections	106
7	The Time-Integrated $B\bar{B}$ Mixing Parameter $\bar{\chi}$	113
7.1	Wrong-Sign Cascade Muons Ratio r_{ws}	113
7.2	N_{ls} and N_{os}	115
7.3	Comparisons with Other Analysis	120
8	Conclusion	121
A	The Maximum Likelihood Fitting Method and Smoothing Technique used in the Impact Parameter Fitting Method	123
A.1	The Choice of Impact Parameter Fitting Method	123
A.2	Motivation for Smoothing	125
A.3	The Smoothing Technique	125
B	My participation in the CDF experiment	129
	Bibliography	136

List of Tables

2.1	Generations of Fermions	4
2.2	Table of the Bosons	4
3.1	The SVX layers' Radius	31
3.2	Some SVX Parameters	32
4.1	Right Sign, Wrong Sign Probabilities	49
4.2	Mixing, No Mixing Probabilities	50
4.3	Dimuon Charge Combination	50
4.4	The independent decay and mixing in both of the dimuon legs result in LS and OS dimuon events. Summing up the LS cells and dividing it by the sum of the OS cells gives Equation 4.2.	51
5.1	By requiring 3 SVX hits, the background reduces more than the Υ signals do.	72
5.2	The world average fractions of b-hadrons determined from Reference [2] as direct measurements.	77
5.3	World average cascade b semileptonic decay rates from Reference [2] .	79
5.4	The central values of combined reweighting factors for Pythia and QQ outputs.	80
6.1	Three bins chosen for $b\bar{b}$ cross section measurements. The order of the muons are determined randomly without preference.	84
6.2	$p_T(b)_{min}$ for the three $p_T(\mu)$ bins.	85
6.3	The central values of the combined reweighting factors for B hadrons from Pythia and QQ outputs.	89

6.4	The central values of the combined reweighting factors for D hadrons from Pythia and QQ outputs.	89
6.5	Acceptances and uncertainties in different muon p_T bins determined from Pythia + QQ generator level dimuon Monte Carlo	91
6.6	Acceptances and assigned uncertainties in different p_T bins as determined from BGenerator + QQ generator level dimuon Monte Carlo. .	92
6.7	The list of (di-)muon event efficiencies and their sources.	100
6.8	$N_{b\bar{b}-1CMP}/N_{b\bar{b}-2CMP}$ under different circumstances.	101
6.9	The number of real $b\bar{b}$ dimuon events (\tilde{N}) is the number of $b\bar{b}$ events from the impact parameter fit (N) times $P^2(\mu)$. We can see that the number and fraction of fake dimuon events for LS and OS are equal within the uncertainties.	106
6.10	$N_{b\bar{b}}$ from the fittings in Figures 6.10, 6.11 and 6.12	110
6.11	$\tilde{N}_{b\bar{b}}$ is from $N_{b\bar{b}}$ after accounting for the fakes.	110
6.12	The $b\bar{b}$ cross sections and assigned uncertainties in the three independent p_T bins.	111
7.1	The result for r_{ws} and its uncertainties	114
7.2	The value for f_{seq} and its uncertainties	115
7.3	Results of the fittings accounting for fakes.	116
7.4	The value for R and the assigned uncertainties.	116
7.5	The value for $\bar{\chi}$ and the assigned uncertainties.	120

List of Figures

2.1	Feynman Diagrams of Leading Order Heavy Quark Production	8
2.2	Feynman Diagrams of Next-to-Leading Order Heavy Quark Production	9
2.3	The CKM triangle is a geometric representation of the unitarity of CKM matrix.	13
2.4	Mechanisms of $B^0\bar{B}^0$ Mixing	15
3.1	The Online Luminosity of CDF Run I Experiment	18
3.2	The Fermilab accelerator has five parts that produce protons and an- tiprotons and accelerate them to 900 GeV	19
3.3	Flow Chart of Accelerator Complex from Steve Holmes' Paper [3] . .	22
3.4	Diagram showing production of antiprotons in the \bar{p} source	23
3.5	The CDF detector (3 Dimensions)	27
3.6	The CDF detector (Quadrant View)	28
3.7	End view of the CTC showing the wire slots. The tilt and overlap of the cells is shown by these slots. Every second slot contains sense wires.	30
3.8	One barrel of SVX (isometric view)	33
3.9	SVX ladder 2 layer module	34
3.10	Central muon coverage in azimuth(ϕ) and pseudorapidity(η)	36
3.11	Central Muon Drift Cell	38
3.12	Central muon chambers location on the central calorimeter	39
3.13	This is an example of a track through the CMU wedge. The dashed line shows the offset of the first and third layers. $ t_4 - t_2 $ provides a rough measurement of p_T . Same thing happens for layers 1 and 3. . .	40

3.14	The DAQ (left hand side) and Trigger Systems (right hand side). Bold arrows show data flow, thin ones control lines and fast outputs. The Scanner Manager and Scanner CPUs are part of the hub feeding Level 3. "FRED" is logic combining Level 1 and Level 2 decisions. The Trigger Supervisor is the control system for the trigger logic through Level 2.	42
4.1	Feynman Diagram showing $b \rightarrow c, \bar{c}$. This process produces a muon carrying the same sign of charge as its ancestor b quark without going through a direct decay.	49
4.2	The Impact Parameter is defined as the shortest distance of the primary vertex to the decay product track. The distance from the primary vertex to the secondary vertex is called the decay length and is proportional to the lifetime of the particle.	52
4.3	The IP distribution of muons of direct and sequential b decays (cm) .	54
4.4	The IP distribution of muons of direct c decays (cm)	55
4.5	The IP distribution of tracks in Photon Jet Data	56
4.6	Normalized and smoothed Impact Parameter Frequency Distributions for the three types of components and their comparison. As we can see, b muons have the longest impact parameters.(X axis are in cm) .	57
4.7	2-d Impact Parameter Frequency Distributions of the 5 templates. (x, y are in cm)	59
4.8	Fit of data sample of mixture of 5000 bb, 5000 cc and 5000 jj events .	61
5.1	Mass Spectrum of OS and LS dimuons from CDF Run IB dimuon Data Set (after all selection criteria). We can see the existence of Υ 's in the OS dimuon signals.	69
5.2	We compare the number of Υ 's under 2 or 3 SVX hits requirements. This figure shows that background signal reduces somewhat more than the muon signals after applying 3 SVX hits criteria.	70
5.3	2-dimensional Impact Parameter Distributions for dimuon data. Shown here are the distributions for Over All, Like-Sign (LS) and Opposite-Sign (OS) Dimuon Impact Parameter Distributions	71

5.4	Dimuon Data Impact Parameter Distribution changes with reducing the max_residual and removing muons. We use the last one for the Impact Parameter Distribution in our analysis.	73
5.5	p_T spectrum of b, c quarks that produce muons in our IP templates. Since our templates requires $p_T(\mu) > 3$ GeV, most of the quarks have a relative high p_T	76
5.6	Monte Carlo $b\bar{b}$ Data Impact Parameter Distribution changes with reducing the max_residual and removing muons. We use the last one for the impact parameter distribution in our analysis.	78
5.7	Validation of some cuts on prompt data (cm)	83
6.1	Quark p_T distribution given different muon p_T . The dashed line in the figure indicates the minimum quark momentum $p_T(b)_{min}$. 90% of the muons in that specific $p_T(\mu)$ bin originate from a b quark with a $p_T(b)$ greater than $p_T(b)_{min}$	86
6.2	Quark rapidity distributions before (above) after (below) the CMU-P Fiducial requirements and 3 GeV/c p_T requirement. The rapidity distribution shrinks to $(-1, 1)$ after the requirements.	90
6.3	Transverse opening angle $\Delta\Phi$ of dimuon events from different sources. We can see they have very similar kinematics.	95
6.4	The figures for calculating the SVX efficiencies. We obtain the efficiencies by counting the number of upsilons in the mass spectrum before and after the criteria.	96
6.5	Upsilons before and after requiring the second CMP	98
6.6	Impact parameter fit for the like-sign dimuon data with both legs CMP fiducial and having CMU hits, we fit the subset of only 1 CMP hit (this plot) and the subset of 2 CMP hits (next plot) to obtain the b-muon fractions and calculate $P(\mu)$	102
6.7	Impact parameter fit for the like-sign dimuon data with both legs CMP fiducial and having CMU hits, we fit the subset of only 1 CMP hit (last plot) and the subset of 2 CMP hits (this plot) to obtain the b-muon fractions and calculate $P(\mu)$	103

6.8	Impact parameter fit for the opposite-sign dimuon data with both legs CMP fiducial and having CMU hits, we fit the subset of only 1 CMP hit (this plot) and the subset of 2 CMP hits (next plot) to obtain the b-muon fractions and calculate $P(\mu)$	104
6.9	Impact parameter fit for the opposite-sign dimuon data set with both legs CMP fiducial and having CMU hits, we fit the subset of only 1 CMP hit (last plot) and the subset of 2 CMP hits (this plot) to obtain the b-muon fractions and calculate $P(\mu)$	105
6.10	Impact Parameter Fitting in the First Subset. We use the convoluted bb muon impact parameter template in the fitting.	107
6.11	Impact Parameter Fitting in the Second Subset. We use the convoluted bb muon impact parameter template in the fitting.	108
6.12	Impact Parameter Fitting in the Third Subset. We use the convoluted bb muon impact parameter template in the fitting.	109
6.13	The Cross Sections Measured in Run IB compared to Run IA and the NLO QCD prediction. The x axis is the lower boundary of the b quark p_T . The y axis is the cross section.	112
7.1	The impact parameter fit for all events (LS + OS)	117
7.2	The like-sign impact parameter fit	118
7.3	The opposite-sign impact parameter fit	119
A.1	This is a small section of our $b\bar{b}$ dimuon histogram sample (magnified). We can see there are statistical fluctuations in the bins. These fluctu- ations are more obvious when we go to higher IP or smaller bins. The smoothing technique makes better use of our knowledge of the physical distribution and provides a better approximation of the IP distribution.	126
A.2	The way we do the smoothing is to take a weighted average of the neighbouring Y_i 's. The weights are chosen to be of a Gaussian shape.	128
B.1	The protocol between the Trigger Manager and the Scanner Manager. (1)	130
B.2	The protocol between the Trigger Manager and the Scanner Manager. (2)	131

Chapter 1

Introduction

The Standard Model of elementary particles and their interactions has two basic components: the unbroken $SU(3)$ color gauge theory, known as Quantum Chromodynamics (QCD) and the spontaneously broken $SU(2) \times U(1)$ electroweak theory. Today, although QCD remains an “unsolved” theory, with no single approximation method applicable to all length scales, the studies of perturbation theory in quantum chromodynamics, i.e. perturbative QCD, or pQCD, is so far very successful in describing a large set of high-energy, large-momentum-transfer cross sections and has proved an invaluable tool in the study of the strong interactions. An important area of research in pQCD is the study of heavy-quark production in the high-energy colliders where protons and antiprotons collide in the multi-GeV energy range.

The phenomenon of neutral mesons changing from their particle to their antiparticle state under weak interaction is another remarkable consequence of the standard model. The hadrons that can undergo particle-antiparticle mixing include K^0 , D^0 , B^0 and B_s^0 , which are copiously produced in high energy experiments. Gell-Mann and Pais [4] predicted in 1955 the existence of $K^0 - \bar{K}^0$ mixing, which was later confirmed by Lande *et al.* at Brookhaven [5]. This subject has been extensively studied in the B system in various experiments including UA1, ARGUS, CLEO, BABAR, BELLE, and CDF. By studying the mixing of the hadrons produced in high energy experiments, we can impose constraints on the elements of the quark mixing matrix - the Cabbibo-Kobayashi-Masakawa (CKM) matrix - and thereby gain a better

understanding of the Standard Model.

At the Tevatron of the Fermi National Accelerator Laboratory (FNAL), protons and antiprotons collide with a center of mass energy $\sqrt{s} = 1.8$ TeV. According to QCD [6] [7], the gluons and quarks that form the protons collide at an energy level of a few hundred GeV. At this energy level, bottom quarks (b) are generated with a significant cross section ($\sim 30\mu b$ [8]) during the collisions, thus enabling the measurements of the bottom quark production cross section and the studies of the B meson mixing at FNAL. In our analysis we use the Fermilab Run IB (from 1993 to 1996) inclusive B meson decay data to study bottom quark production and compare our results with the pQCD predictions. The same data set is used for the studies of the B^0 and B_s^0 mixing parameters.

The structure of this thesis is as follows: Chapter 2 discusses the theoretical basis for our analysis. Chapter 3 describes in detail the relevant experimental apparatus used to produce our data. Chapter 4 describes the mathematical and computing methods used in our analysis. Chapter 5 describes the experimental and Monte Carlo data used in the analysis. Chapter 6 and 7 presents the details of the analysis and the final results and discusses the systematic uncertainties of the results. Chapter 8 gives a brief summary of the conclusion of our analysis. Appendix A describes a mathematical tool used in the analysis.

Chapter 2

Theory

2.1 Standard Model

The physical world's complexity and diversity has always been a challenge to man's intelligence since ancient times. A common approach was to search for the simplicity underneath the seemingly overwhelming complexity of the material world. In approximately 500 BC, Laozi wrote in his Bible of Taoism (Dao De Jin) that: "Tao generates one, one generates two, two generates three, and three generates everything in this world." [9] Modern scientists believe that the world is composed of elementary particles. These elementary particles fall into two classes: fermions and bosons. This diverse and ever-changing world is nothing but fermions interacting with each other via exchange of bosons.

Fermions can be grouped into three generations, each generation including two types of quarks and two types of leptons (and their anti-particles as indicated in Table 2.1). Bosons can be classified into four groups, each corresponding to one of the four different types of interactions among fermions: gravitational, weak, electromagnetic, and strong. Table 2.2 shows the details of these interactions and their bosons.

Although free leptons are relatively stable and easy to identify in isolation, their counterparts, free quarks, have never been found in experiments. So far we have only detected hadrons, particles composed of either two quarks, called mesons ($q\bar{q}$), or three quarks, called baryons (qqq), in high energy experiments. By observing the

Generations	1	2	3	Charge
quarks	up (u)	charm (c)	top (t)	$\pm\frac{2}{3}$
	down (d)	strange (s)	bottom (b)	$\pm\frac{1}{3}$
leptons	electron (e)	muon (μ)	tau (τ)	± 1
	e neutrino (ν_e)	μ neutrino (ν_μ)	τ neutrino (ν_τ)	0

Table 2.1: Generations of Fermions

Interactions	Gravity	Weak	E&M	Strong
bosons	(Graviton, G)	W^\pm, Z^0	Photon (γ)	Gluon (g)
Coupling Strength	Gm_p^2 $\sim 6 \times 10^{-39}$	$G_F m_p^2$ $\sim 10^{-5}$	α $\sim \frac{1}{137}$	α_s ~ 1
Range (meters)	∞	10^{-18}	∞	10^{-15}
Quantum Number	Mass	Weak Isospin	Charge	Color
Theory	In Progress	EW (QED)		QCD

Table 2.2: Table of the Bosons

physical properties of these hadrons, we are able to deduce the properties of the invisible quarks.

The way the quarks “stick” together and become hadrons is through the exchange of gluons, the bosons that mediate the strong interactions. The hadrons can interact with each other and with leptons through exchange of the other three types of bosons. We describe such exchanges with quantum field theories. These theories require local gauge invariance, causality, renormalizability and locality. Due to the gauge invariance of the fermion fields, the relevant phases can be chosen arbitrarily without affecting any observables. This symmetry leads to the conservation of quantum numbers. Gauge bosons naturally arise in these theories from the requirement of local gauge invariance.

In principle, for each elementary interaction there should be a quantum field theory describing it. A universally accepted quantum field theory describing the interaction

of gravity does not exist yet. The quantum field theory for electromagnetic interactions is called Quantum Electrodynamics (QED), which is a local gauge theory where the symmetry group of gauge transformation is an unitary group in one dimension ($U(1)$). The quantum field theory for the weak interactions is the Glashow-Salam-Weinberg theory, which unifies the electromagnetic interactions and weak interactions by $SU(2)_L \times U(1)$ symmetry. In this theory, spontaneous symmetry breaking is introduced to retain renormalizability and thus results in the weak interaction bosons, W^\pm and Z , acquiring mass. The quantum field theory for strong interactions is Quantum Chromodynamics (QCD), in which gauge transformations are operating on color charges of a $SU(3)$ symmetry group. There are three color charges (red, blue and green) and their anti-color charges in QCD, but these color charges are not directly observable because colored free quarks must combine to form colorless hadrons ($q\bar{q}$ or qqq).

The combination of QCD and electroweak theory is the Standard Model. It has $SU(3) \times SU(2)_L \times U(1)$ gauge invariance and is the basic framework of today's particle physics. There is a rich body of experimental evidence supporting this model. [10]

On the other hand, our incomplete understanding of flavor physics [11] [12], CP violation, the stability of the Higgs, the new $g_\mu - 2$ result [13], neutrino oscillations and masses [14] and dark matter [15] suggest the incompleteness of the Standard Model and therefore have made it necessary to study more of the different aspects within and beyond the Standard Model.

2.2 Heavy Quark Production

In experimental high energy physics, a major experimental approach in the studies of elementary particles is to build large accelerators that accelerate and collide elementary or semi-elementary particles. By observing the outcome of these collisions, we can test various aspects of the Standard Model. The Fermilab Tevatron is one of these colliders. It collide protons and anti-protons at high energy ($\sqrt{s} = 1.8$ TeV).

Since p and \bar{p} are hadrons composed of three quarks, $p\bar{p}$ collisions can be studied in similar ways as the other hadron collisions. In principle, the scattering process among

the hadrons during the collisions can be considered as the sum of 1 on 1 interactions among the many individual quarks and gluons that form the two hadrons. These constituent quarks and gluons are collectively called partons. During the hadron collisions, new quarks, antiquarks and gluons are created. In theory, the cross section for heavy quark-antiquark production in hadron collisions can be written as Equation (2.1): [16]

$$d\sigma^{h_1, h_2} = \sum_{i,j} \int dx_1 dx_2 d\sigma_{ij}(x_1 P_1, x_2 P_2, k_1, k_2, m, \mu) f_i^{h_1}(x_1, \mu) f_j^{h_2}(x_2, \mu) \quad (2.1)$$

In this equation,

- $h_{1,2}$ are the incoming hadrons
- $x_{1,2}$ are the momentum fractions of partons in $h_{1,2}$
- $P_{1,2}$ are $h_{1,2}$'s momenta
- $k_{1,2}$ are the momenta of the quark and antiquark
- m is the mass of the heavy quark
- μ is the subtraction scale for removing divergences arising from QCD
- $d\sigma_{i,j}$ is the short distance parton-parton cross section for heavy quark production and can be calculated with perturbative methods.
- The function f is the wave function (structure function) of the incoming partons.

The strength of the strong interaction in the collision is characterized by α_s , which can be written as:

$$\alpha_s = \frac{1}{B \ln(q^2/\Lambda^2)} \quad (2.2)$$

where B is a constant, Λ is the parameter representing the scale at which the coupling constant becomes strong, and q^2 is the momentum transfer of the interactions. QCD is known to have the property of asymptotic freedom: when q^2 is very large then α_s is small. In the asymptotic regime, the cross section $\sigma_{i,j}$ can be expressed in terms of an expansion in α_s . The next-to-leading order approximation calculation of the

cross section for inclusive $b\bar{b}$ production was carried out by Nason, Dawson and Ellis (NDE) [17]. The fully exclusive parton cross section for all heavy $q\bar{q}$ was calculated to the order of $O(\alpha_s^3)$ by Mangano, Nason, and Ridolfi (MNR) [8].

In this analysis, we study the $b\bar{b}$ production cross section in $p\bar{p}$ collisions at $\sqrt{s} = 1.8$ TeV (energy of the center of mass). This energy level is high enough for the heavy quark production cross section to be well approximated with a power series expansion.

As indicated by the Feynman diagrams in Figures 2.1 and 2.2, there are three different types of heavy quark production mechanisms: gg , gq and $q\bar{q}$.¹ At just above the $b\bar{b}$ production energy threshold, valance quarks which have the larger part of the momentum fraction compared to the gluons produce the majority of the $b\bar{b}$ pairs. However at Fermilab $p\bar{p}$ collide at the energy of $\sqrt{s} = 1.8$ TeV which is much higher than the $b\bar{b}$ production energy threshold. At this energy level, gluons which have the smaller part of the momentum fraction carry sufficiently high energy and produce the majority (95%) of $b\bar{b}$ pairs.

It is well known that a variety of measurements of the integrated cross section vs. b quark transverse momentum at the Tevatron by both the CDF [18] [19] and D0 [20] experiments yield results which are systematically larger, by a factor of about two or more than the NLO QCD predictions.

These results hold for inclusive b quark cross sections for both central and more forward production and also hold for exclusive B meson production. Results more recently published by CDF for the differential cross section for $B^+ \rightarrow J/\psi K^+$ production [21] from Run I data quantify the discrepancy in the ratio of the observed to predicted cross section as $2.9 \pm 0.2 \pm 0.4$. From this and other differential cross section measurements, it appears that the discrepancy between data and theory appears to largely in normalization; the spectral shapes are generally in good agreement.

The observed discrepancy is not restricted to hadroproduction experiments at 1800 GeV. The early measurements made by the UA1 Collaboration of b quark production at $\sqrt{s} = 630$ GeV [22] [23] [24] gave results that did not seem to show a marked

¹The figures do not show all of the production modes. There could be internal loops in the b production in the collisions but they are not shown here.

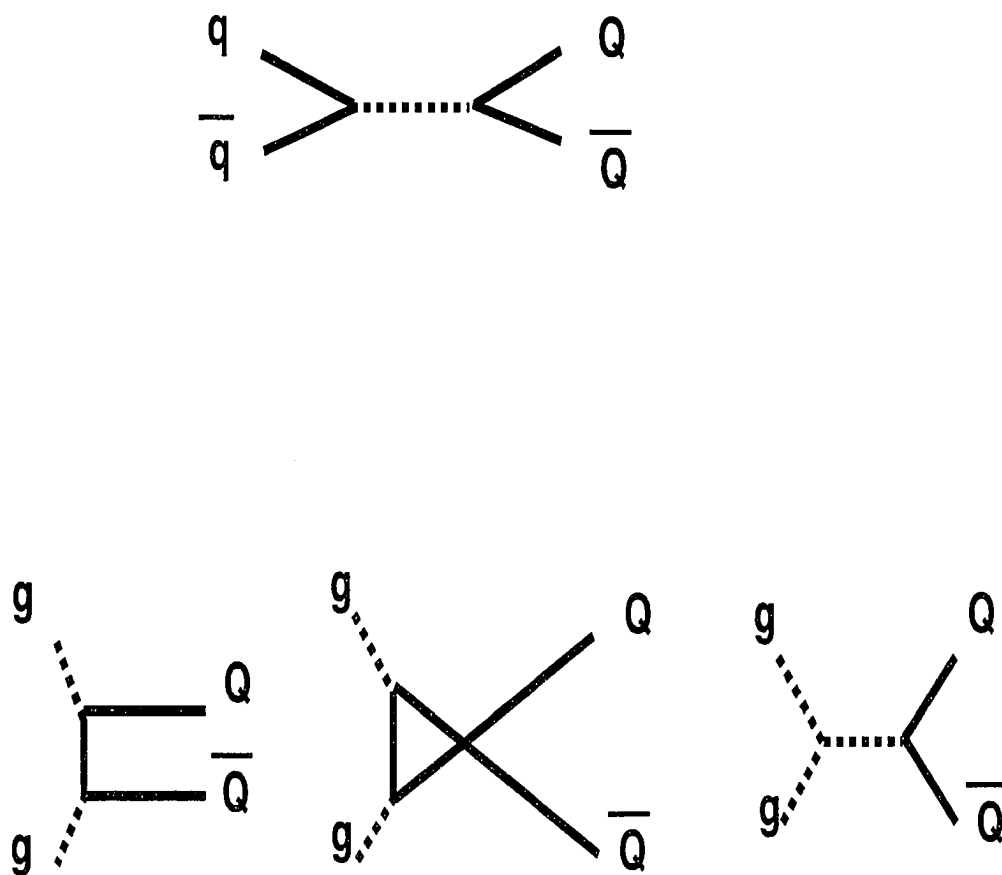


Figure 2.1: Feynman Diagrams of Leading Order Heavy Quark Production

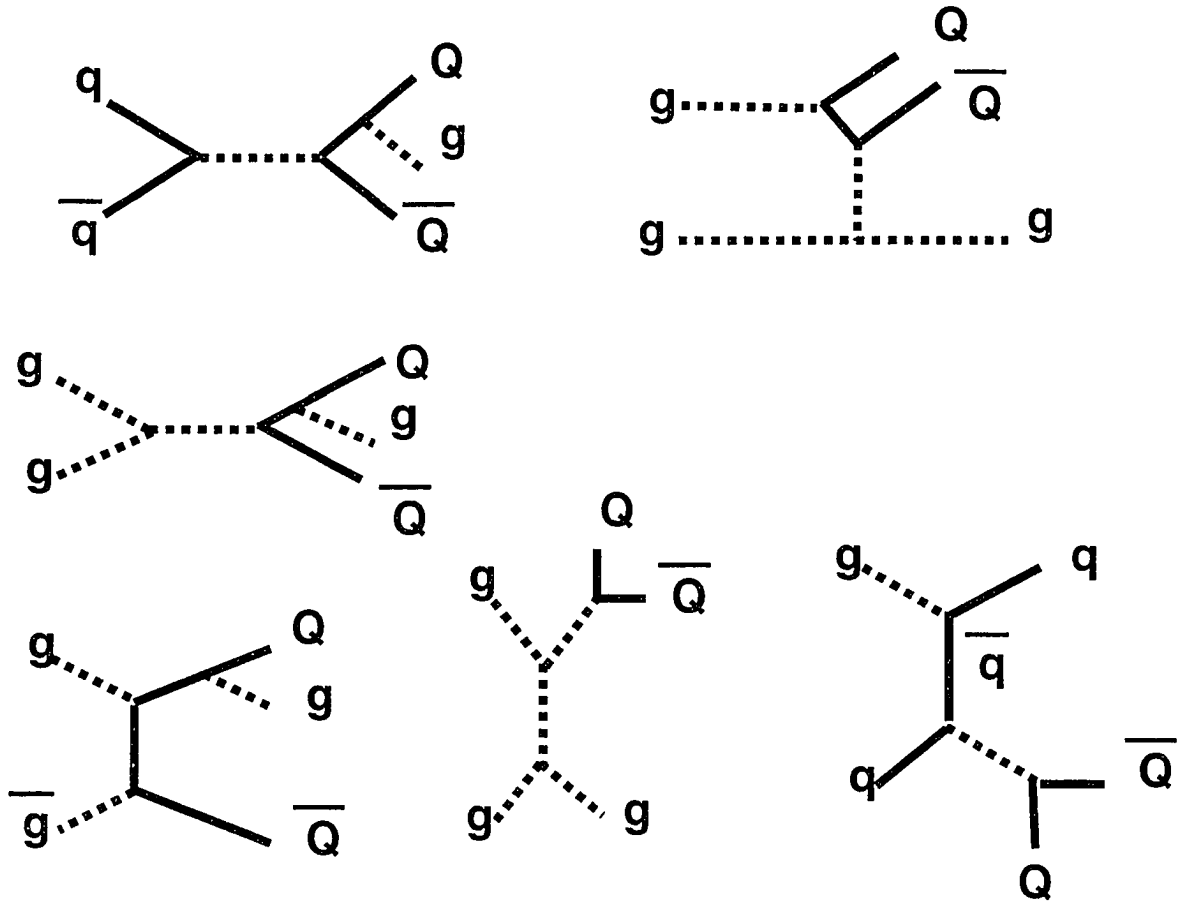


Figure 2.2: Feynman Diagrams of Next-to-Leading Order Heavy Quark Production

departure from theoretical predictions at the time.[25] [26] In order to compare with the UA1 results more directly, the Fermilab Tevatron ran at an energy of $\sqrt{s} = 630$ GeV for 9 days and CDF measured [27] the ratio of the bottom quark production cross sections at $\sqrt{s} = 630$ GeV and $\sqrt{s} = 1800$ GeV. The ratio $\sigma(630)/\sigma(1800) = 0.171 \pm .024 \pm .012$, is in good agreement with NLO QCD predictions. The bottom quark production cross section obtained by CDF is still above, but in marginal agreement with the UA1 results. Both UA1 and CDF results are above the NLO QCD prediction for 630 GeV, using modern structure functions, though the UA1 results are within their uncertainty of the central value for the predictions.

The discrepancy between data and theory for b production in hadronic interactions is in contrast to the good agreement for the case of top quark production at the Tevatron (note however that the production of $t\bar{t}$ pairs at the Tevatron receives important contributions from the annihilation of valence quark-antiquark pairs). The nominal expectation was that the mass of the b quark (4.5 to 5 GeV/ c^2) is large enough that the intrinsic momentum scale for the interactions leading to production would be such that pQCD would give converging results. However, quantitatively large uncertainties are present in the calculation for bottom (as well as charm) hadroproduction cross sections.[28] [29] The main issue appears to be neglected higher order terms in the perturbative expansion. The QCD order α_s^3 calculations for b quark hadroproduction are above 100% of the Born term, and it is possible that higher order terms could give comparable contributions. It is also necessary to consider possible non-perturbative effects. Large uncertainties can arise from scale dependence for the perturbative expansion of the various parton subprocesses when trying to account for both renormalization and factorization scale variations.

An important source of uncertainty may reside in the proper understanding of the non-perturbative fragmentation (QCD) process by which B hadrons are formed from b quarks. The effect of fragmentation is to modify (reduce) the momentum carried by the B hadron originating from a b quark. The effect is intrinsically not large, being of order of the hadronic scale (few hundred MeV) divided by the b quark mass. Nevertheless, since the b quark cross section has a steeply falling spectrum in transverse momentum, and almost all measurements need to impose a minimum

transverse momentum requirement, the effects must be carefully considered. Recent work [30] suggests that leading-log calculations of the observable B hadron spectrum may not be sufficient when comparing to next to leading-log calculations. Specifically it is believed that the fragmentation functions determined largely in $e^+e^- \rightarrow Z^0 \rightarrow b\bar{b}$ reactions may need to be re-evaluated using a next to leading-log formalism in order to be properly incorporated in a comparison of data and theory in hadroproduction. The authors find that they are able to reduce the discrepancy from 2.9 to 1.7 for the B^+ CDF results mentioned above.

The measurement reported in this thesis is of importance in this discussion, because it provides a measurement of the $b\bar{b}$ cross section. It is expected that this measurement, because of the kinematic selections imposed, should be less sensitive to higher order terms.[31] We will compare our measured $b\bar{b}$ production cross section with theoretical results and previous CDF measurements.

2.3 $B\bar{B}$ Mixing Parameter

2.3.1 CKM Matrix

In the studies of weak interactions in B physics, it is very important to understand the quark mixing matrix. It is found that the strong (flavor) eigenstates are not the same as the weak interaction eigenstates. Weak interactions can violate flavor quantum number such as strangeness (S). For example, changes in strangeness ($\Delta S = 1$) due to the weak interactions have been observed in experiments. The suppressed decay rate for $\Delta S = 1$ decays compared to $\Delta S = 0$ decays is explained by the Cabbibo angle $\theta_c = 0.2205 \pm 0.0018$ [32]. In general, to account for all flavor changes, we need to apply a unitary transformation matrix to rotate the set of the strong eigenstates into the weak eigenstates.

$$\begin{pmatrix} \bar{u} & \bar{c} & \bar{t} \end{pmatrix} \begin{pmatrix} d' \\ s' \\ b' \end{pmatrix} = \begin{pmatrix} \bar{u} & \bar{c} & \bar{t} \end{pmatrix} U \begin{pmatrix} d \\ s \\ b \end{pmatrix} \quad (2.3)$$

The unitary matrix for this transformation is called the Cabbibo-Kobayashi-Maskawa (CKM) matrix [33]:

$$\begin{pmatrix} d' \\ s' \\ b' \end{pmatrix} = \begin{pmatrix} V_{ud} & V_{us} & V_{ub} \\ V_{cd} & V_{cs} & V_{cb} \\ V_{td} & V_{ts} & V_{tb} \end{pmatrix} \begin{pmatrix} d \\ s \\ b \end{pmatrix} \quad (2.4)$$

where (d, s, b) are the strong eigenstates and (d', s', b') are the weak eigenstates.

Respecting unitarity and adjusting arbitrary phases, without losing generality, we can reparametrize the CKM matrix with 4 variables [34]: A, λ, ρ, η .

$$\begin{pmatrix} V_{ud} & V_{us} & V_{ub} \\ V_{cd} & V_{cs} & V_{cb} \\ V_{td} & V_{ts} & V_{tb} \end{pmatrix} = \begin{pmatrix} 1 - \lambda^2/2 & \lambda & A\lambda^3(\rho - i\eta) \\ -\lambda & 1 - \eta^2/2 & A\lambda^2 \\ A\lambda^3(1 - \rho - i\eta) & -A\lambda^2 & 1 \end{pmatrix} \quad (2.5)$$

This reparameterization is correct to the order of λ^4 where $\lambda = \sin \theta_c$.

Figure 2.3 is a geometric representation of the relationships (Equation 2.6) among the CKM matrix elements due to the unitarity of the CKM matrix. In this representation on the complex plane, $V_{cd}V_{cb}^*$ is rescaled to 1 so that the apex of the triangle is located at (ρ, η) .

$$V_{ud}V_{ub}^* + V_{cd}V_{cb}^* + V_{td}V_{tb}^* = 0 \quad (2.6)$$

The complex phase in the CKM matrix caused by η leads to CP violation in the Standard Model because the Lagrangian of weak interactions between quarks is not Hermitian. The angles of the CKM triangle α, β and γ are related to the phase and can be measured in CP violating B-decays. Furthermore, the non-closure of this triangle i.e. $\alpha + \beta + \gamma \neq \pi$ would suggest that our understanding of CP violation within the Standard Model is incomplete. Physics beyond the Standard Model can be further investigated, for example, by measuring CP asymmetries in several B decays that depend on the same unitarity angle or studying decays where zero asymmetries are expected in the Standard Model.

The determination of CKM matrix is crucial for a full definition of the Standard Model and may reveal a underlying structure of new physics.

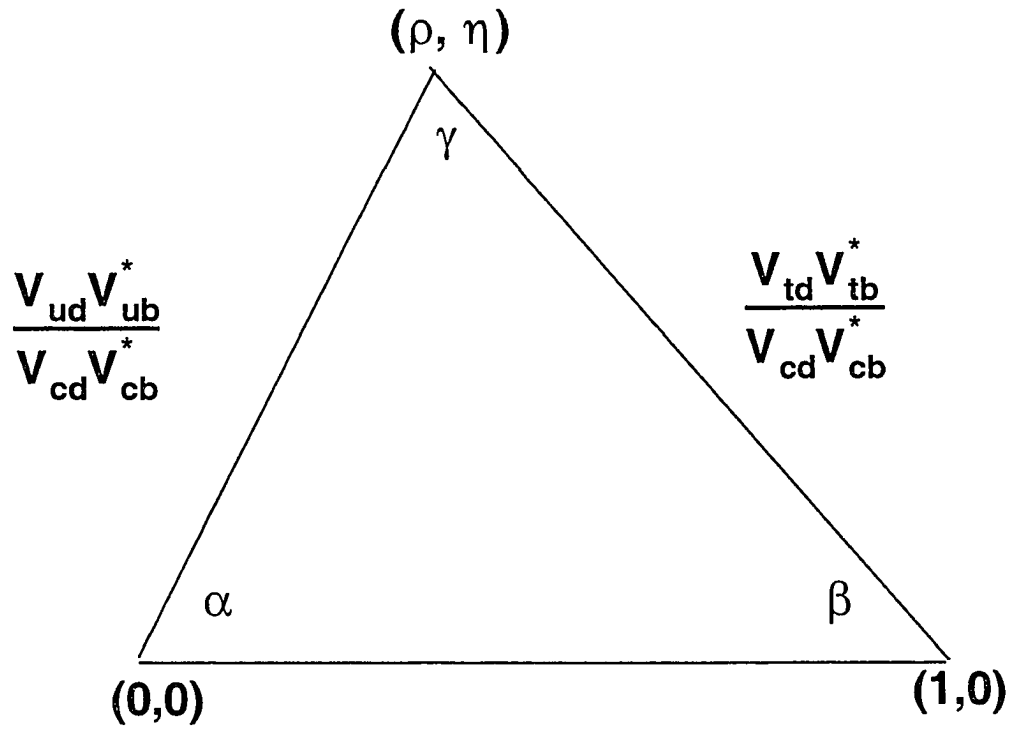


Figure 2.3: The CKM triangle is a geometric representation of the unitarity of CKM matrix.

2.3.2 $B^0\bar{B}^0$ Mixing

The fact that the electroweak eigenstates are different from the flavor eigenstates results in the possibility that particles created under the strong interaction will mix under the electroweak interactions. B^0 's created in the $p\bar{p}$ collision are flavor eigenstates (Figure 2.1 and 2.2). After leaving the center of collisions, they will transform under the weak interaction according to the CKM matrix elements. Figure 2.4 shows the two possible ways for a B^0 to mix with a \bar{B}^0 through second order W-exchanges. The weak eigenstates of the neutral B mesons, B_1 and B_2 , are linear combinations of B^0 and \bar{B}^0 as follows:

$$\begin{aligned} |B_1\rangle &= \frac{1}{\sqrt{2}}(|B^0\rangle + |\bar{B}^0\rangle) \\ |B_2\rangle &= \frac{1}{\sqrt{2}}(|B^0\rangle - |\bar{B}^0\rangle) \end{aligned} \quad (2.7)$$

When a flavor eigenstate $|B^0\rangle$ is created, it evolves under electroweak interactions. From equation 2.7, we obtain:

$$|B^0\rangle = \frac{1}{\sqrt{2}}(|B_1\rangle + |B_2\rangle) \quad (2.8)$$

Since $|B_1\rangle$ and $|B_2\rangle$ evolve over time in the following manner:

$$\begin{aligned} |B_1(t)\rangle &= e^{iM_1t - \Gamma_1t} |B_1(0)\rangle \\ |B_2(t)\rangle &= e^{iM_2t - \Gamma_2t} |B_2(0)\rangle \end{aligned} \quad (2.9)$$

where M_1 and M_2 are the characteristic mass of the eigenstates. The probability of transformation at time t is given by:

$$P(B^0 \rightarrow \bar{B}^0)(t) = \frac{1 - \cos(\Delta mt)}{2} e^{-\Gamma t} \quad (2.10)$$

Here the Δm is the difference between the masses of the weak eigenstates ($\Delta m = |M_1 - M_2|$) and Γ is the average decay width of the two states ($\Gamma = \frac{\Gamma_1 + \Gamma_2}{2}$). The time integrated probability (also called the mixing parameter) is:

$$\chi_{(d,s)} = \int dt P(B_{(d,s)}^0 \rightarrow \bar{B}_{(d,s)}^0)(t) = \frac{1}{2} \frac{x_{(d,s)}^2}{1 + x_{(d,s)}^2} \quad (2.11)$$

Here $x = \Delta m/\Gamma$ is the dimensionless mixing parameter. Both B^0 and B_s^0 can mix, but with different mixing parameters, because Δm is different for the two species.

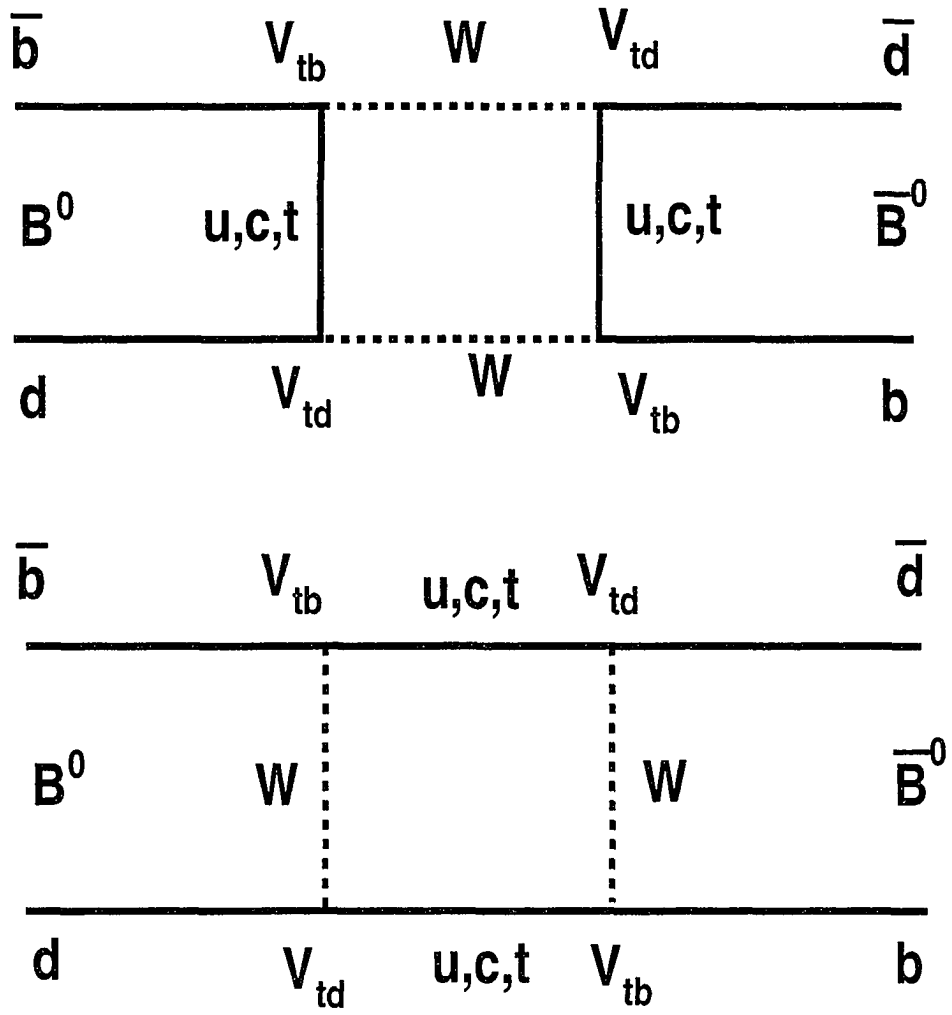


Figure 2.4: Mechanisms of $B^0 \bar{B}^0$ Mixing

The Δm for $B^0\bar{B}^0$ and $B_s^0\bar{B}_s^0$ mixing can be written respectively as:

$$\begin{aligned}\Delta m_d &= C_d |V_{tb}^* V_{td}|^2 \\ \Delta m_s &= C_s |V_{tb}^* V_{ts}|^2\end{aligned}\tag{2.12}$$

Here C_d and C_s are constants derived from QCD corrections, meson decay constants, the top quark mass, and the weak coupling constant. The V 's are the CKM matrix elements. Since C_d and C_s involve hadronic factors that are hard to obtain experimentally while the ratio of them is easier to predict [35], it is advantageous to exploit the relation:

$$\frac{\Delta m_s}{\Delta m_d} = \frac{C_s}{C_d} \left| \frac{V_{ts}}{V_{td}} \right|^2\tag{2.13}$$

In fact, $C_d/C_s \approx 1.19 \pm 0.10$ and roughly cancel out each other [35], therefore by measuring the ratio of mixing parameters for B^0 and B_s , we will be able to put constraints on the CKM elements.

Several experiments have measured Δm_d . [36] [37] [38] [39] [40] [41] with consistent results. Combining all published measurements, [42] [43] [44] [45] [46], and accounting for all identified correlations yields $m_d = 0.478 \pm 0.012(stat) \pm 0.013(syst)ps^{-1}$.

$B_s\bar{B}_s$ oscillation has also been the subject of many recent studies from ALEPH [47], CDF [48], DELPHI [49], OPAL [50] and SLD [51]. No oscillation signal has been found so far. The most sensitive analyses appear to be the ones based on inclusive lepton samples, and on samples where a lepton and a D_s meson have been reconstructed in the same jet. The combined results of limits on Δm_s is $m_s > 13.1ps^{-1}$ at 95% CL [32].

The average time-integrated B mixing parameter we measure is the weighted average of χ_d and χ_s as indicated in Equation 2.14.

$$\bar{\chi} = f_d \times \chi_d + f_s \times \chi_s\tag{2.14}$$

Chapter 3

Apparatus

3.1 Overview of the Apparatus

Fermilab, whose full name is Fermi National Accelerator Laboratory (FNAL), [52] is located in the western suburbs of Chicago, Illinois, covering about 6,800 acres of land. The major component of Fermilab is its accelerator, the Tevatron. Protons and antiprotons circulate in opposite directions at an energy of 900 GeV in the Tevatron and collide at two sites, CDF (Collider Detector at Fermilab) and D0, where particle detectors were built to study the collision results. Due to the richness of the $p\bar{p}$ collision products, several physics groups specializing in Top, QCD, Electroweak, Exotic, and Bottom are formed to make full use of the collision data. Our analysis is one of the projects of the Bottom Physics Group of CDF.

The last run of Tevatron from year 1992 to 1996 is called Run I, which is divided into three periods, Run IA (8/92-8/93), Run IB (8/93-8/95) and Run IC (8/95-2/96). There have been many important results in Run I, among which the most prominent one was the discovery of the top quark in 1994. Our analysis is based on data collected from CDF during Run IB.

In this chapter, we provide general features and capabilities of our apparatus as well as details of the detector components relevant to our analysis.

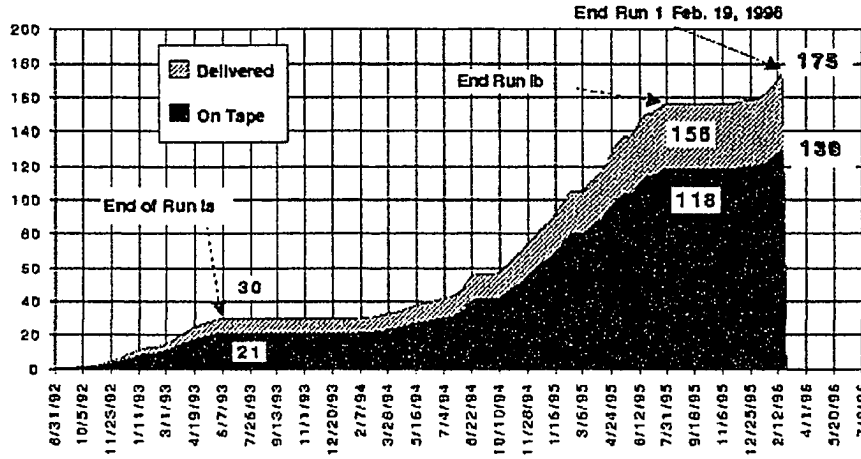


Figure 3.1: The Online Luminosity of CDF Run I Experiment

3.2 Accelerator

The Fermilab Tevatron, depicted in Figure 3.2, consists of five accelerators and a pair of rings. To achieve the head-on $p\bar{p}$ collisions at high energy, we start with ionizing Hydrogen atoms. Then these ions are put through a series of accelerations before electrons are stripped off. The resulting high energy protons are on one hand used as the p source of $p\bar{p}$ collision in Tevatron and, on the other hand, used to produce antiprotons by colliding them against nickel targets. The antiprotons are collected and accelerated to 900 GeV to collide with the high-energy protons in Tevatron.

The first accelerator is called the preaccelerator. It consists of a negative hydrogen ion source, a Cockcroft-Walton generator, an electrostatic accelerating column, and a transport line. In the negative hydrogen ion source, hydrogen from a gas bottle is injected into a magnetron surface-plasma H^- source comprised of a central cathode surrounded by an anode with a magnetic field passing through the apparatus. Hydrogen atoms are absorbed into this 1 mm-wide dense plasma gap and pick up electrons that are confined by strong electromagnetic fields in this gap. Free H^- ions are produced by colliding energetic particles, such as protons, against the cathode surface

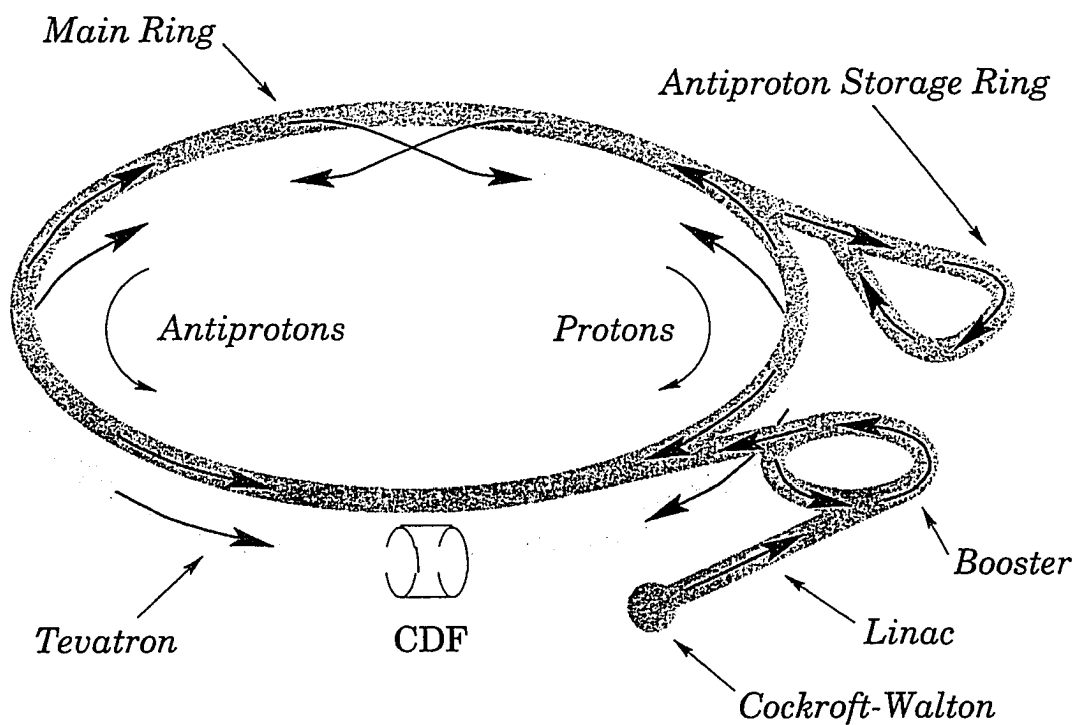


Figure 3.2: The Fermilab accelerator has five parts that produce protons and antiprotons and accelerate them to 900 GeV

into which the H atoms are absorbed. H atoms leaving the cathode surface have a small chance of acquiring an electron from the cathode and become H^- ions. The energetic protons also have a chance to pick up two electrons and become H^- ions. There is an aperture in the anode through which H^- ions and other particles can escape. These particles are then accelerated by an extraction plate before a magnetic bend is used to sift out H^- ions. A commercial Cockcroft-Walton generator is then used in this preaccelerator to accelerate the H^- ions to 750 keV.

The second accelerator is called the Linac. It is an Alvarez drift-tube accelerator of 150 m in length and produces pulsed 200 MeV beams of H^- ions. It includes 9 electrically resonant, cylindrical, oxygen free, high conductivity, copper clad steel tanks, each of which is driven by a RF system resonating at 201.24 MHz and delivering 5 MW in 400 μ s pulses. [53] There are drift tubes suspended in the center of the tanks with gaps between the tubes for acceleration of the H^- ions. Within the tube, focusing-defocussing quadrupole magnets are built to reduce space charge and other disruptive effects. An RF debuncher is used to reduce the H^- 's momentum spread at the end of the Linac.

The third accelerator is the Booster, which is an 8 GeV fast cycling proton synchrotron of 75.5 m in radius. Here, the H^- beam from Linac is stripped of all electrons while merging with the proton beam already circulating in the Booster. The H^- beam first goes through a dogleg, which is actually 2 dipoles of opposite polarity displacing the H^- and proton beams into a common path. Then, the beam goes through a stripping foil before being put through another dogleg (orbital bump magnet) where protons are captured and H^- and H are directed to a beam dump. About 3×10^{12} protons are collected in 6 turns of the 15 Hz synchrotron before the orbital bump magnets turn off and the RF turns on to accelerate them to 8 GeV.

The fourth accelerator is the Main Ring. It is a 400 GeV proton synchrotron of radius 1 km. In the Main Ring, the protons are used for two purposes: 150 GeV protons for injection to the Tevatron and 120 GeV protons for antiproton production. Protons from the Booster are captured and injected into the Main Ring for acceleration. Here, several bunches of protons or antiprotons are coalesced by counterphasing the RF stations and then restoring the normal RF, capturing the bunch. 15 proton

bunches and 11 antiproton bunches are coalesced before injecting to the Tevatron.

The antiproton stacking is achieved by capturing protons from the Booster and accelerating them to 120 GeV in the Main Ring before extraction to the \bar{p} source. The \bar{p} source consists of a target station, Debuncher ring, Accumulator ring and transport lines. (Figure 3.4) First the Main Ring protons are directed edge-on to a disk target made of nickel. The result of the reactions of the 120 GeV proton beam with the nickel target includes antiprotons of about 8 GeV. (The 8 GeV energy was chosen to match the Booster proton energy before going into the Main Ring and a 120 GeV proton beam is the most efficient way to generate 8 GeV antiprotons.) The secondary particles from p and nickel reactions then pass through a cylindrical lithium lens that carries a longitudinal 0.5 MA pulsed current. The current produces azimuthal magnetic fields that focus the antiprotons in space. After that, a pulsed dipole magnet selects 8 GeV \bar{p} into a transport line to the Debuncher. The Debuncher reduces the \bar{p} momentum spread through RF bunch rotations and adiabatic debunching. It also reduces the transverse profile of the beam through betatron stochastic cooling. [54] The Accumulator is in the same tunnel as the Debuncher but slightly smaller. Its shape is close to a triangle with 6 short straight sections at the vertices. These sections give alternating high and low dispersion regions and cool the particles into small orbits. The Accumulator's RF adiabatically captures particles from the Debuncher, cools them to 60 MeV and puts them into the tail of the "stack". Then the beam bunches are debunched adiabatically before momentum stochastic cooling decelerates the \bar{p} 's into the stack over a period of about an hour. In the stack core, the \bar{p} 's are controlled by momentum cooling and betatron cooling. When enough antiprotons are collected, a portion (about 1/2) of them are injected into the Main Ring to be accelerated to 150 GeV.

The last and most important accelerator is the Tevatron. Bunches injected from the Main Ring are boosted to 900 GeV here, making it the highest-energy accelerator in the world. The Tevatron is of the same size as the Main Ring ($r = 1$ km) and lies approximately 65 cm under it. When it was built, the Tevatron was the first large scale superconducting synchrotron in the world. Six proton bunches and six antiproton bunches circulate in the Tevatron and collide in two luminous regions: CDF and

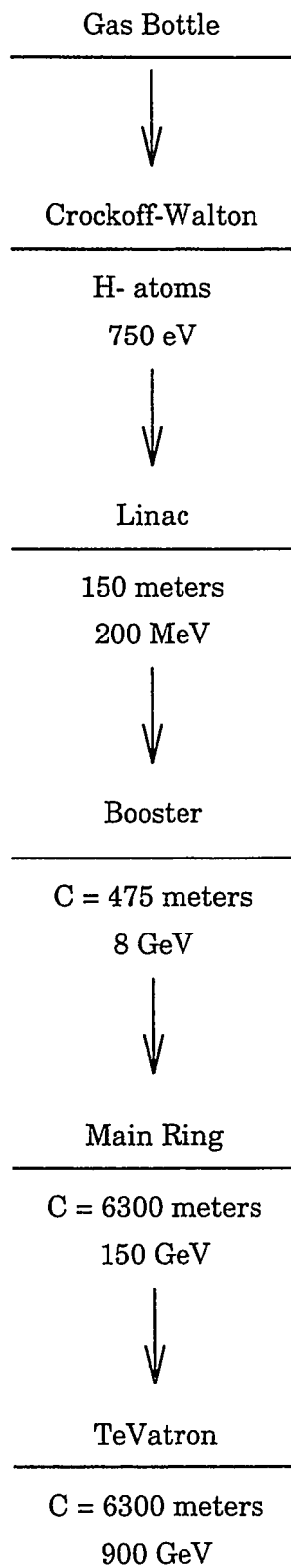


Figure 3.3: Flow Chart of Accelerator Complex from Steve Holmes' Paper [3]

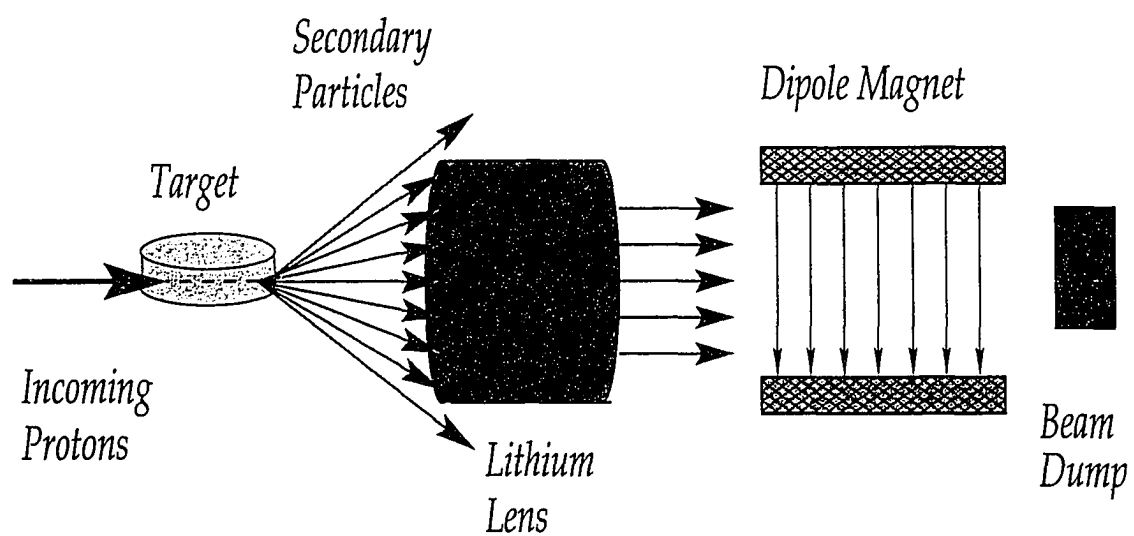


Figure 3.4: Diagram showing production of antiprotons in the \bar{p} source

D0, where low- β quadrupoles squeeze the beam cross section into a two-dimensional Gaussian distribution with a standard deviation of $35\mu\text{m}$. In the longitudinal direction, the bunches have a standard deviation of about 30 cm. The luminosity at CDF continued to increase over time during the whole Run I period. (Figure 3.1)

In order to study the physics of the high energy collisions of protons and antiprotons, large detectors are built around the collision spot.

3.3 Collider Detector at Fermilab (CDF)

The Collider Detector at Fermilab is a general purpose detector designed to study the energy, momentum, and the identity of particles produced in $p\bar{p}$ interactions at the Tevatron. It is approximately 27 meters long, 10 meters high, and weighs about 5000 tons. Figure 3.5 shows a 3-d diagram of CDF. The longitudinal axis of CDF is usually chosen to be the z axis in our research. The transverse plane perpendicular to z is the $x - y$ plane or $r - \phi$ plane if polar coordinates are chosen. The major part of CDF consists of the following parts (starting from the center): the Silicon Vertex Detector (SVX), the Vertex Time Projection Chamber (VTX), the Central Tracking Chamber (CTC), a super conducting solenoid, electromagnetic and hadronic calorimeters, and muon chambers. Farther forward, there are the plug and forward calorimeters, the beam-beam counters, and the Forward Muon System (FMU). There are also trigger and data acquisition systems that process the signals from all detector subsystems.

Particles that can be individually identified in CDF are primarily photons, electrons, and muons. We can therefore classify the detector subsystems into tracking (to measure momentum), calorimetry (to measure energy), and the muon system (to identify muons). The combination of tracking and calorimetry identifies the electrons and photons. With muon system we can identify muons.

The tracking systems consist of the SVX, VTX, CTC and the superconductive solenoid. It measures the momentum of charged particles. The solenoid coil [55] creates a 1.41 T magnetic field in the beam direction to bend the charged particles' tracks for measurements. It is cooled by forced flow of 2-phase helium. The Central Tracking Chamber (CTC) is an 84-layer cylindrical drift chamber which provides 3-d

tracking for charged particles. The Vertex Time Projection Chamber (VTX) has 28 modules and covers the radial region from radius 8 cm to 50 cm surrounding the SVX region. It determines the interaction vertex z position with 1 mm resolution. (The spread of z in the interactions is a Gaussian distribution with $\sigma = 26.65$ cm [56].) The Silicon Vertex Detector (SVX) consists of 4 layers of silicon vertex strip detectors and provides precision tracking in the $r - \phi$ plane. It has very good resolution ($\sim 20\mu\text{m}$) and can measure displaced secondary B decay vertices. The accurate measurement of this displacement is very important to our analysis.

The calorimeter systems consist of electromagnetic and hadronic calorimeters. They include the Central ElectroMagnetic calorimeter (CEM), the Central Strip Chambers (CES) and the Central Hadron Calorimeter (CHA). These calorimeters consist of projective towers uniformly segmented in the $\eta - \phi$ space, i.e. pseudorapidity - azimuth angle space. Each tower points at the interaction region and has a segmentation of $0.1(\eta) \times 15^\circ(\phi)$ in the central region. The particles generated at the collision region interact with these calorimeters and have their energies measured here.

The CEM towers provide longitudinal energy samples where lead sheets are interleaved with scintillator layers. The lead sheets are the absorbers and scintillators are the active medium. Light signals from the scintillators are collected using acrylic light guides at the corner of the tower and measured by photomultiplier tubes. The electromagnetic energy measured here has resolution $\sigma_E/E = 0.135/\sqrt{E \sin \theta}$ where θ is the polar angle from the z axis.

The CES is a proportional strip chamber used to determine the position and transverse development of electromagnetic shower. [57] Its chambers are located at 6 radiation lengths depth within the electromagnetic calorimeter volume in order to be sensitive to maximum shower development.

The CHA is composed of 32 layers of interlaced steel plates and scintillators. It is 4.7 absorption lengths in depth and absorbs 95% of hadronic showers at 50 GeV. The energy resolution of the CHA is $0.35/(\sqrt{E} + 0.04)$.

The muon systems consist of the Central Muon Detector (CMU), the Central

Muon Upgrade (CMP), and the Central Muon Extension (CMX). CMU is a 4-layer drift chamber detector that identifies muons and determines muon momentum. Muons surviving the calorimeters can be detected by the CMU and be identified here. CMP has similar functions but because of the steel absorber (~ 3 interaction lengths) between CMU and CMP that absorbs most of the hadronic punchthroughs, CMP has purer signals of muons. CMX covers rapidity areas that is not covered by CMU and CMP. (CMU-P covers $|\eta| \leq 0.7$ and CMX covers $|\eta| \in (0.7, 1.0)$). In the transverse plane, both CMU and CMP cover most of the azimuthal regions except some blank areas that are reserved for technical reasons. (See Figure 3.10)

The plug and forward calorimeters, beam-beam counters and the FMU are also important component of CDF. However, we do not use their information in our analysis except that the integrated luminosity of our experiment needs to be measured with the help of the beam-beam counter.

The trigger and data acquisition system of CDF has three levels. The first two of them consist of FASTBUS based trigger hardware and the third one consists of a software processor farm. They serve as data filters and converters so that the data written to the storage are valuable data worthy of further offline studies.

The detailed information on the detector CDF is available in various sources [1]. In the following sections, we will discuss the CDF components that are most important to our analysis.

3.4 Central Tracking Chamber (CTC)

In our analysis, we need to precisely measure the momenta of the muons and other charged particles. The measurement is carried out by the tracking detectors. The CTC is the main tracking device in the CDF detector and is the only one that provides 3-d tracking information. The CTC is an 84-layered cylindrical drift chamber with an outer diameter of 2760.0 mm and a length of 3201.3 mm including the endplates. The inner diameter of the chamber is 554.0 mm, leaving space for SVX and VTX. The whole CTC is immersed in an 1.41 T axial magnetic field from a superconducting solenoid. The nonuniformity in the strength of the magnetic field is up to 10^{-4} in

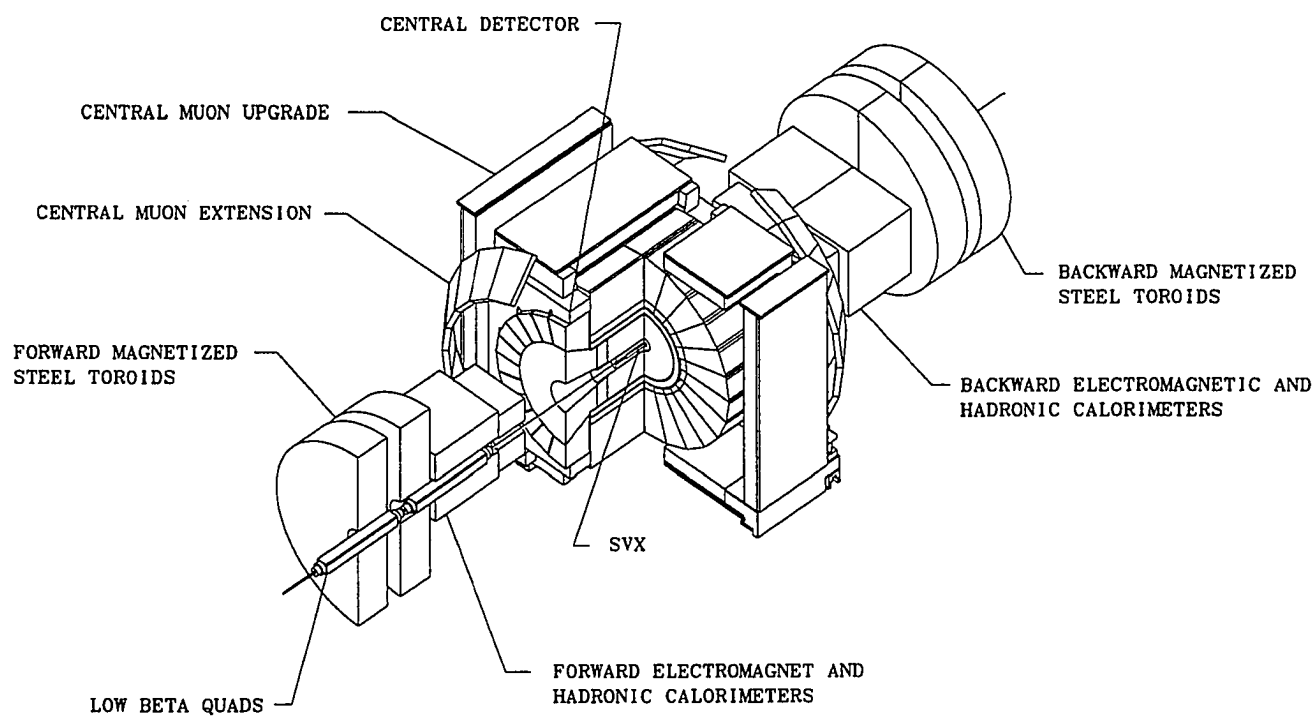


Figure 3.5: The CDF detector (3 Dimensions)

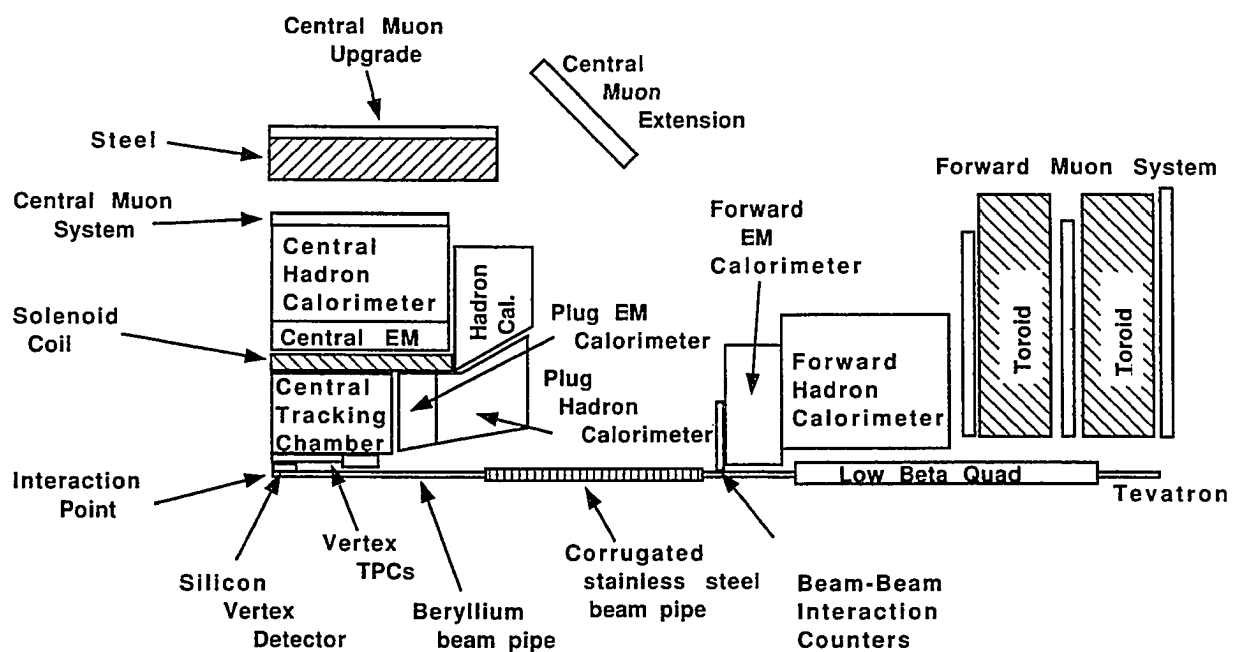


Figure 3.6: The CDF detector (Quadrant View)

time, 3×10^{-3} along the axis and 8×10^{-3} radially. The precision of the CTC momentum measurement is $\delta p_T/p_T \approx 10^{-3} p_T$ at 90° to the z axis. The CTC uses 5 axial superlayers of sense wires interlaced with 4 small angle ($\pm 3^\circ$) stereo superlayers. Small angle stereo layers provide the desired z pointing resolution of $3 - 4$ mm to match the Electromagnetic calorimeter resolution.

The superlayers are large drift cells with 12 sense wires per axial superlayer and 6 sense wires per stereo superlayer. The drift cell segmentations in the tracking volume has a maximum drift time of about 800 ns (compared to the $3.5 \mu\text{s}$ crossing time between the $p\bar{p}$ interactions) and allows relatively large number of measurements per track. Using multiple sense wires in one cell enables the identification of ambiguous or corrupted information via the observations of the correlated information among neighboring sense wires.

The drift cells are tilted by 45° . (Figure 3.7) This is an important feature of the CTC because it reduces the the dead space and allows the time-to-distance relationship to be linear at the end of the cells. Since we chose a 1.41 T magnetic field, a relatively low electric field (just high enough to saturate the drift velocity) in the chamber operation, and a gas mixture of Argon/Ethane/Ethanol 49.6/49.6/0.8%, we end up with a large Lorentz angle, β , for the drift trajectories ($\beta = 0$ when $B = 0$). The tilt of drift cells makes the drift trajectories approximately azimuthal. The overlap of the drift cells makes radial tracks passing close to at least one sense wire in every superlayer, sampling the whole range of drift times in each superlayer.

3.5 Silicon Vertex Detector (SVX')

The SVX' is a silicon microstrip vertex detector providing high precision $r - \phi$ plane tracking for CDF Run IB. (Figure 3.8) It is very important to our analysis because our Impact Parameter Fitting Method is built on the fact that B mesons have a long life time and produce particles with large impact parameters and therefore stand out in the secondary vertices distribution.

As an improved version of an earlier incarnation of Silicon Vertex Detector used in Run IA, SVX' has many advantages. The SVX' replaced the older SVX after a

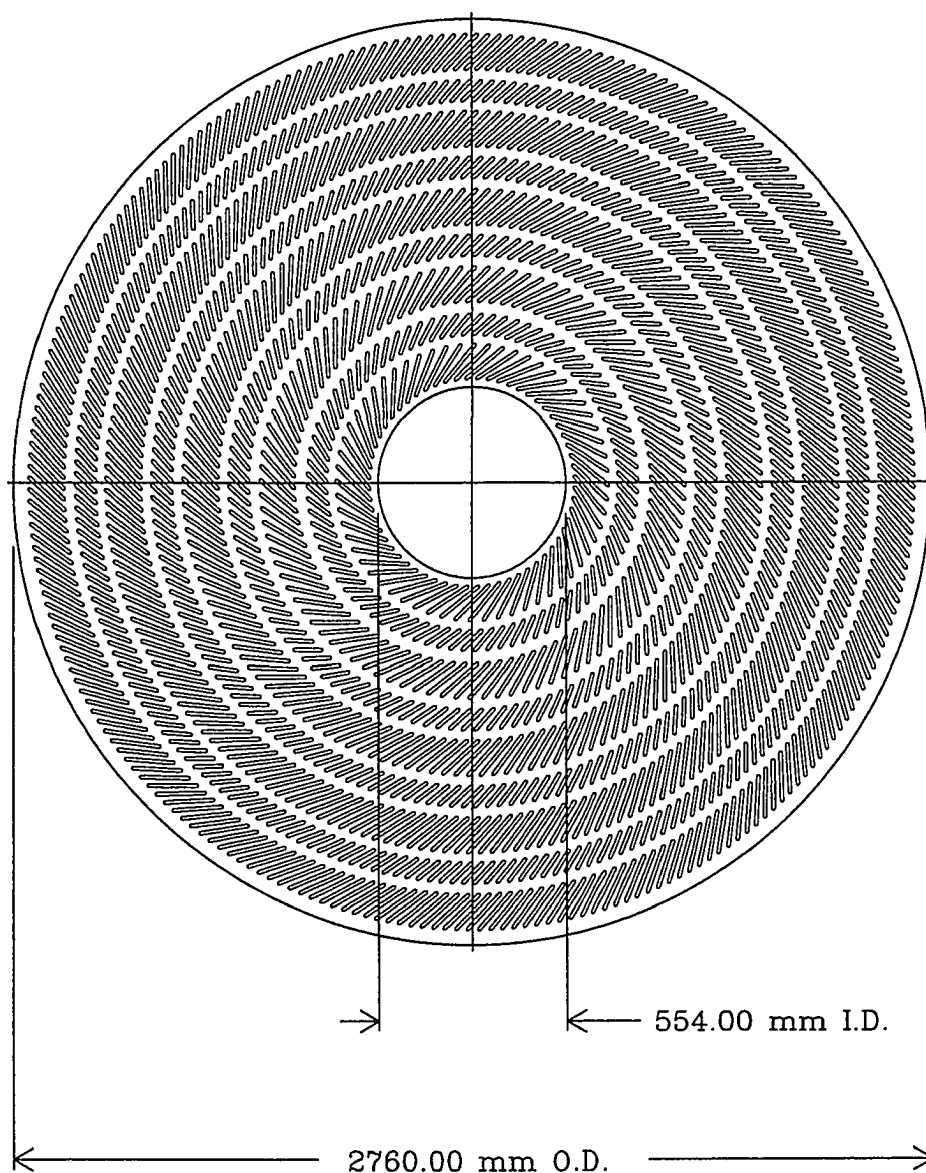


Figure 3.7: End view of the CTC showing the wire slots. The tilt and overlap of the cells is shown by these slots. Every second slot contains sense wires.

year's run. This newer version was radiation hardened and AC coupled with lower noise. In our analysis, SVX' will be referred to as SVX for convenience.

The SVX lies within VTX and the overall mechanical stability of it relies on VTX support. It is also immersed in the VTX gas volume of Argon/Ethane and they share a common cabling flange between two of the VTX modules at $z = 0$. The SVX is made up of two independent identical barrels each of about 25.5 cm in length with a gap of 2.15 cm between them. The length of the SVX is made to cover as much the $p\bar{p}$ collision area (of $\sigma_z = 30$ cm) as practical. Each SVX barrel is covered with an external conductive cylindrical skin that isolates it from electromagnetic noise, external high voltage breakdown and adds rigidity to the system. Each SVX barrel is also made up of 4 concentric cylindrical layers of single sided, AC couple silicon detectors. (Figure 3.8) The layers are numbered 0 to 3 from inside to outside. Layers 0 and 3 have the microstrips facing towards the beam, while layers 1 and 2 are mounted with the microstrips facing outside. The distance between the surface of layer 0 and the exterior of the 3.8 cm-diameter Beryllium beam pipe is less than 1 cm. The radius of the layers are listed in Table 3.1. The ladders are installed between support bulkheads made of Beryllium. The whole SVX is held at a temperature of 20° through the use of a water cooling system and a series of temperature sensors to avoid thermal expansion, relative detector motion, increased leakage current and chip failure due to thermal heating.

Layer	Radius (cm)
0	2.9
1	4.3
2	5.7
3	7.9

Table 3.1: The SVX layers' Radius

Each SVX layer has 12 equal-sized ladders as shown in Figure 3.9. They are all aligned to form 12 wedges. The pitch of the strips is $60\mu\text{m}$ for layers 0-2 and $55\mu\text{m}$ for layer 3. The silicon detectors are 8.5cm long and $300\mu\text{m}$ thick with different

Layer	Number of Chips	Readout Strips	Active Area Width (μm)	Crystal Width (μm)
0	2	256	15360	16040
1	3	384	23040	23720
2	4	512	30720	31400
3	6	768	42240	42930

Table 3.2: Some SVX Parameters

widths for each layer (Table 3.2). On the face of each barrel, each ladder is rotated 3° about its major axis to allow some overlap between neighboring wedges except in layer 0. Since the strips are along the z axis, SVX can only provide $r - \phi$ information of the tracks. The accuracy of SVX measurement is $13\mu\text{m}$ in spatial hit resolution and $\sigma_D(p_T) = 13 + 40/p_T(\mu\text{m})$ in impact parameter resolution. The amount of material of SVX is made to be as small as possible to minimize the radiation lengths and multiple scattering in SVX. Most particle tracks traverse about 0.05 radiation lengths of material when passing through the SVX.

The SVX readout and data acquisition electronics has 46080 channels and data is recorded for those signals passing sparsification thresholds. There are altogether 360 readout chips which are bonded to the silicon strips and each chip has 128 channels. Each chip consists of circuitry for charge integration, voltage amplification, sample and hold, a comparison and latching, and control. The chips read out the analog voltage level and send it together with the channel address to the electronics crates mounted outside the CDF detector where the signals are digitized. The signal to noise in the SVX is about 9 : 1.

SVX needs very precise alignment to achieve optimum performance. The SVX components are very carefully aligned during construction and closely monitored during the run. The strips are aligned to $2.5\mu\text{m}$. The ladder substrates are typically flat to about $75\mu\text{m}$ and the detectors on a ladder are aligned to close to $4.5\mu\text{m}$. The average bow in an SVX ladder is $23\mu\text{m}$. The maximum misalignment of the barrels is less than $10\mu\text{m}$. The wedge to wedge residual misalignment is less than $10\mu\text{m}$.

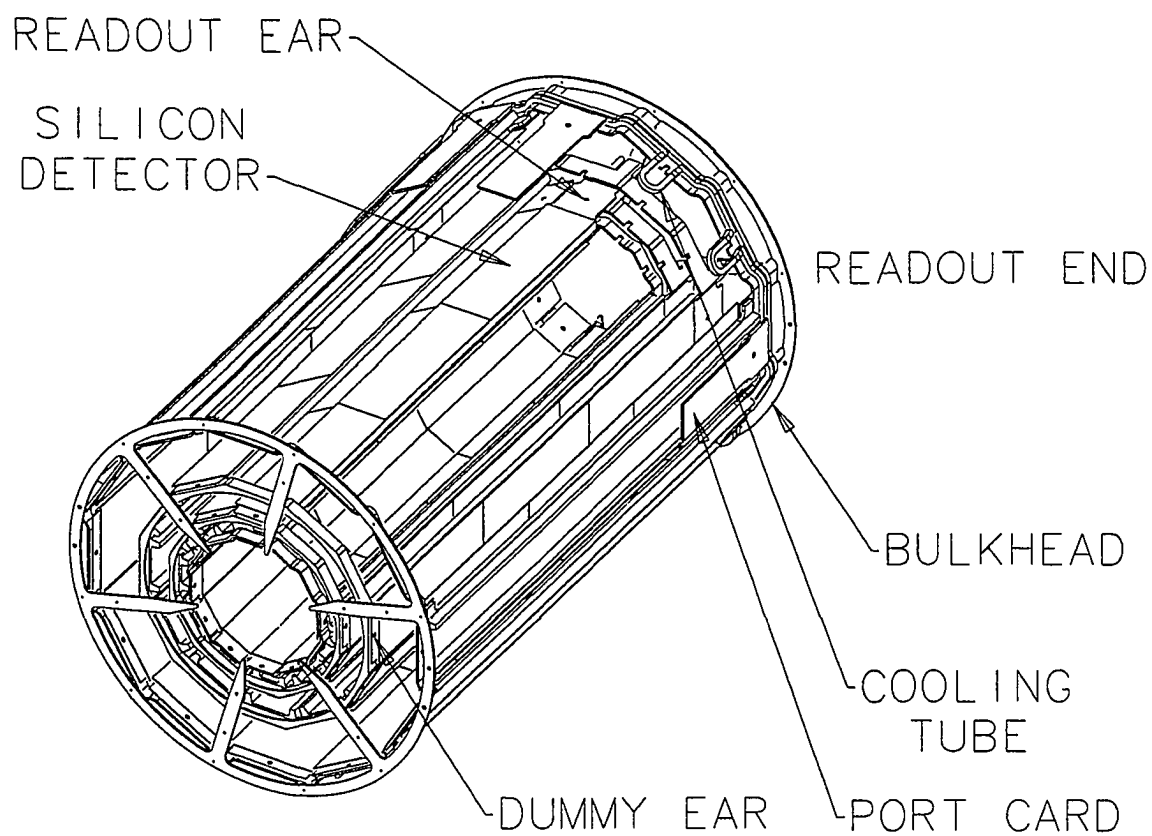


Figure 3.8: One barrel of SVX (isometric view)

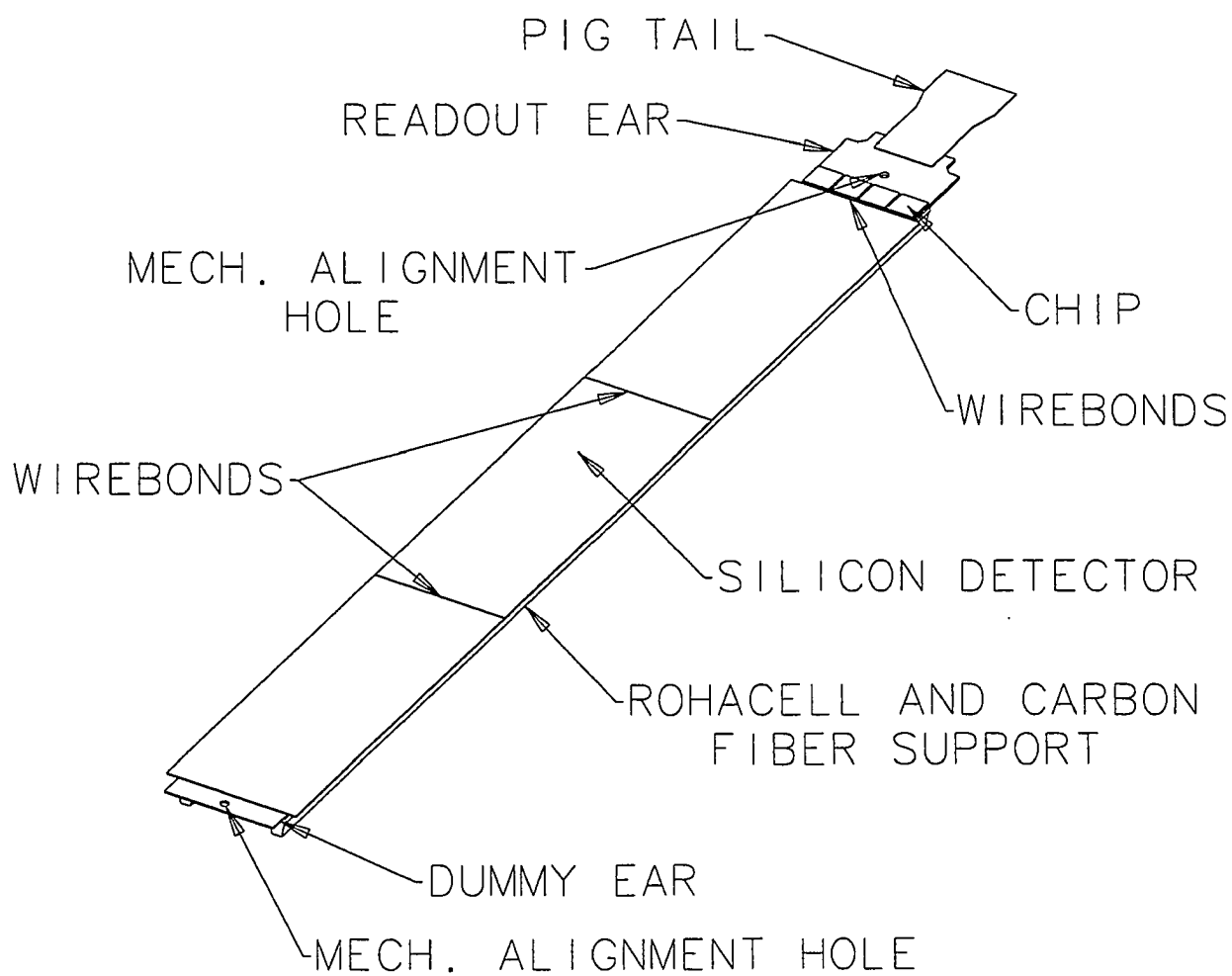


Figure 3.9: SVX ladder 2 layer module

Radiation damage to the SVX CMOS electronics and silicon itself had been a concern since Run IA. Even after radiation hard techniques were used in SVX', radiation monitoring and protection systems to ensure normal functioning of the SVX' were still important components of the experiment.

SVX is crucial to our impact parameter measurements and improved our charged particle momentum determination.

3.6 Beam-Beam Counters

The Beam-Beam Counters (BBC) are mounted on the front of the forward calorimeters. It is also our primary luminosity monitor and provides a minimum bias trigger.

The BBC is composed of a set of scintillator paddles with photomultiplier readout. The paddles cover the angular region 0.32° to 4.47° from the beamline ($3.24 \leq \eta \leq 5.90$) in both forward and backward directions. The timing resolution for the BBC is about 200 ps. When there is at least one hit in each plane of the BBC at opposite ends of the detector within a 15 ns coincidence window around the beam crossing, BBC fires a trigger.

The luminosity of the experiment is obtained by counting the number of interactions with BBC triggers and dividing this number by the known cross section for $p\bar{p}$ collisions to trigger the BBC. The instantaneous luminosity dependence of this cross section and detector deadtime needs to be accounted for during the calculation of the luminosity.

3.7 Central Muon Systems

Our analysis relies on the muon systems to identify our dimuon events. The muon systems include the Central Muon Chambers (CMU), the Central Muon Upgrade (CMP), and the Central Muon Extension (CMX). (Figure 3.5) They are all located outside the calorimeters and identify the muons by looking at their penetration in the muon chambers. These muon tracks are also called stubs and are matched to tracks found in the CTC.

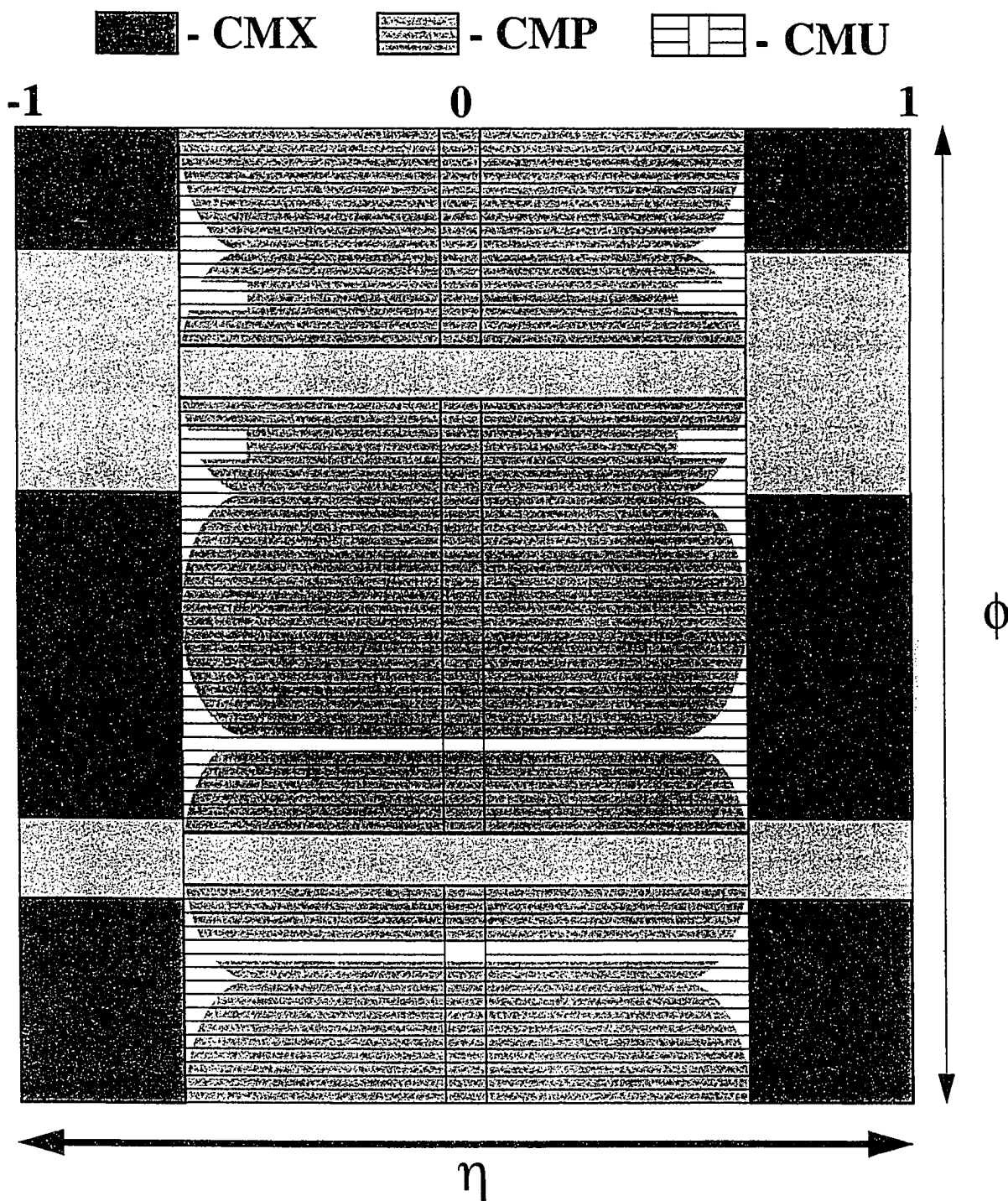


Figure 3.10: Central muon coverage in azimuth(ϕ) and pseudorapidity(η)

The CMU chambers are located at a radius of 3470 mm from the beam line. The chambers consist of 4 layers of drift chambers attached externally to the calorimeter wedges. It is segmented in 15° wedges in ϕ and each wedge is further segmented in ϕ into 3 modules. The detectors in each wedge are 12.6° wide, thus leaving 2.4° gaps between neighbouring wedges. Each layer of drift chambers has 4 drift cells with a steel resistive sense wire of radius of $50\mu\text{m}$ through the middle of each cell. The sense wire is held at 3150 V and the maximum drift time is about $1.2\mu\text{s}$. The chambers use a 50/50 mix of Argon/Ethane bubble through ethanol at -5°C . The chambers are operated in limited steamer mode. The z coordinate is determined from charge division. The position resolution in the ϕ direction is approximately $250\mu\text{m}$ and the z resolution is about 1.2 mm. At the end of the chambers the signals are picked up from the sense wires by preamps and sent to electronics crates outside the detector where they are shaped, amplified and discriminated. Discriminated signals are sent out of the collision hall to the Time to Digital Converters (TDCs).

The CMU chambers use a 2 mm offset of two pairs of sense wires from the center of the detector to resolve the left-right ambiguity (as shown in Figure 3.13). The difference in the drift times between the aligned wires gives a rough estimation of the p_T of the muons. Large p_T tracks have small drift time while small p_T tracks tend to have large drift time. The measured p_T is used in the first level muon trigger.

The Central Muon Upgrade (CMP) consists of rectangular drift chambers of 4 layers. The chambers are about 6.4 m in z direction and form a 4-sided open box around the CMU. A 60 cm thick layer of steel absorber lies between the CMU and CMP to absorb the hadronic punchthroughs. Before arriving at the steel absorber, the hadrons usually traverse 5 absorption lengths of material and about 0.5% of them survive and become fake muons in the CMU. The steel absorber is about 3 absorption lengths and reduces the hadronic punchthroughs by an additional factor of 20, thus achieves a higher purity in the muon reconstruction. On the other hand, the additional multiple scattering and energy losses in the steel absorber raises the observable threshold of the muon p_T to be 2.2 GeV in the CMP detector.

Figure 3.10 shows the $\eta - \phi$ coverage of CMU-CMP-CMX. We will focus on the central rapidity region and make use of the differential purity in CMU and CMP.

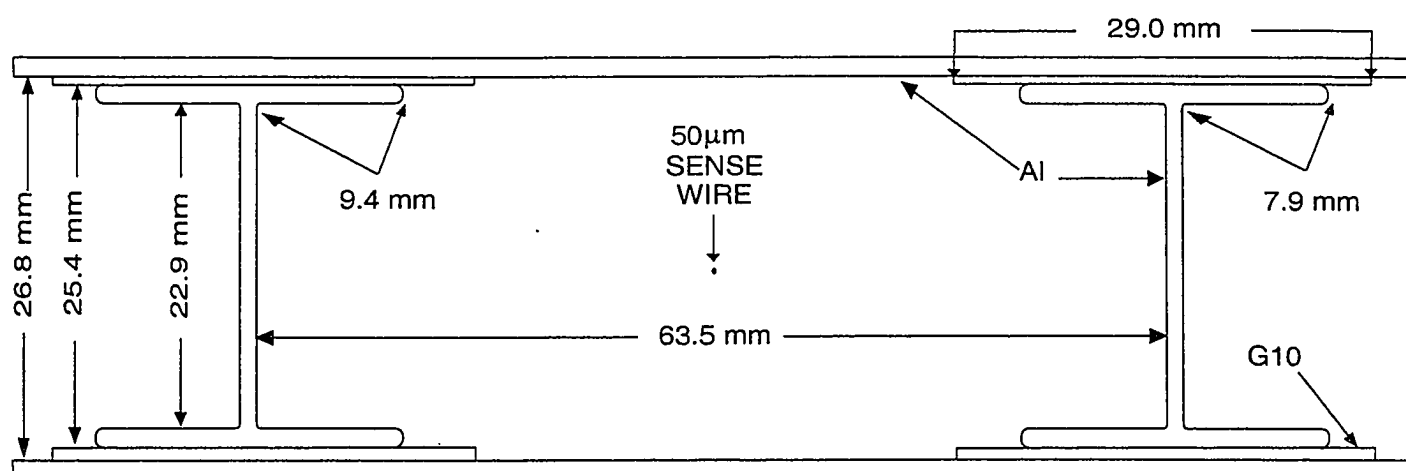


Figure 3.11: Central Muon Drift Cell

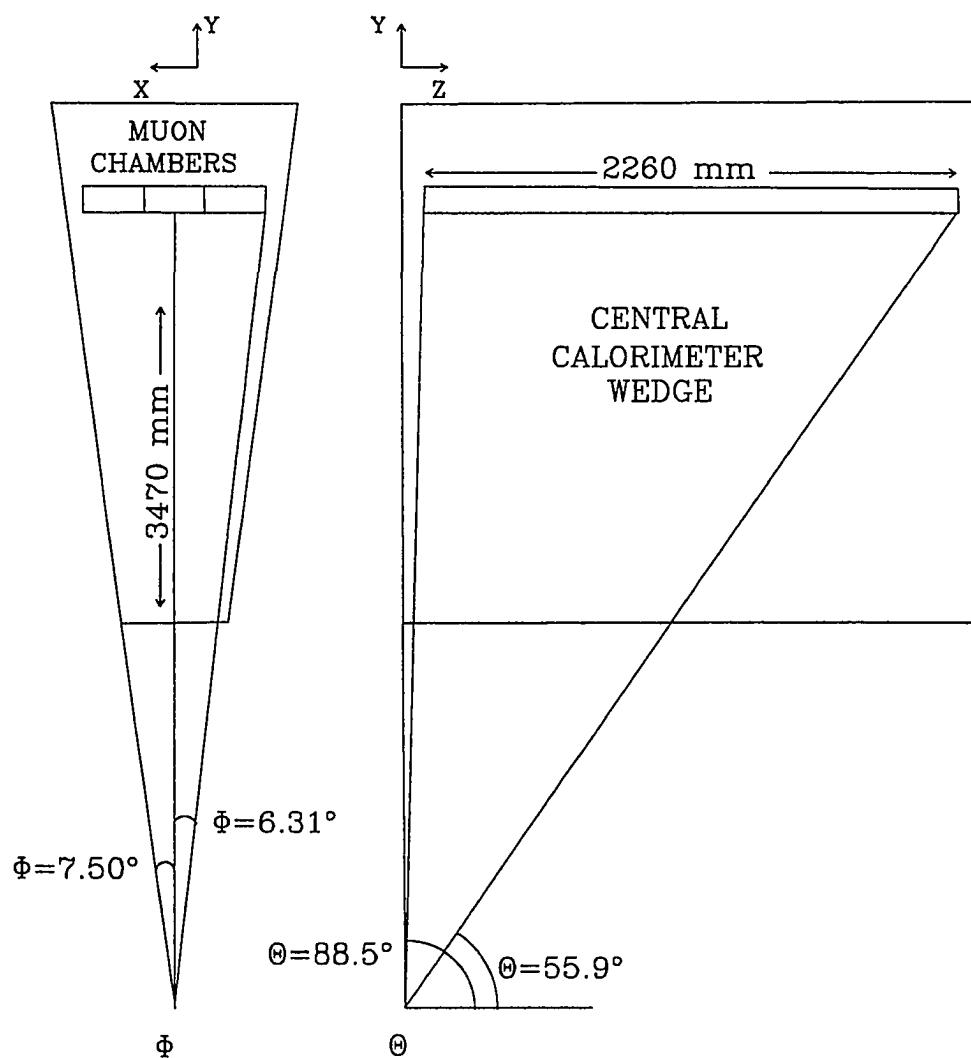


Figure 3.12: Central muon chambers location on the central calorimeter

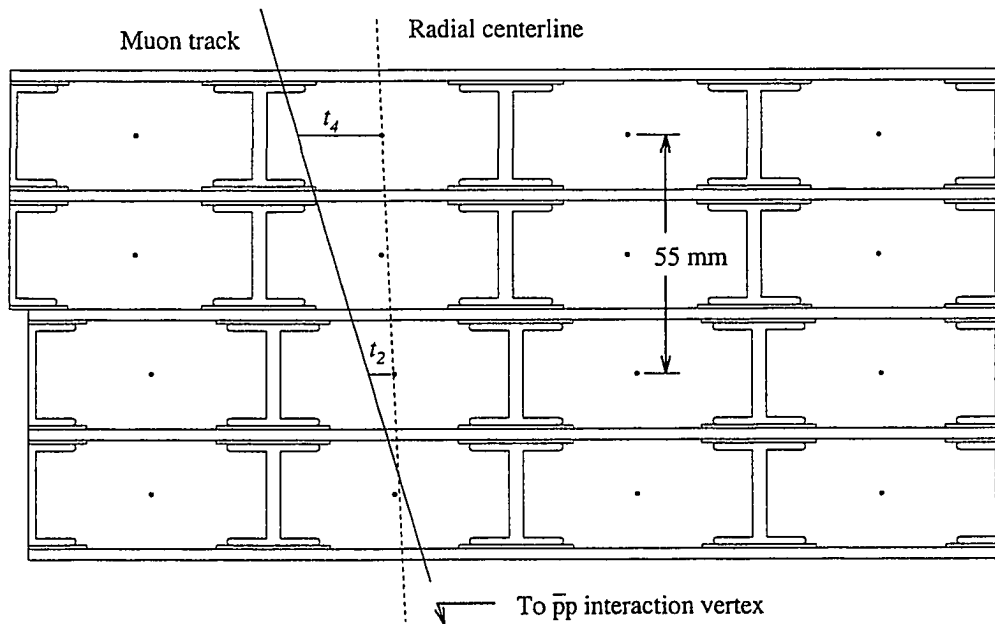


Figure 3.13: This is an example of a track through the CMU wedge. The dashed line shows the offset of the first and third layers. $|t_4 - t_2|$ provides a rough measurement of p_T . Same thing happens for layers 1 and 3.

CMX is not used in our analysis.

In CDF, muon stubs from CMU-CMP is matched to the CTC tracks by extrapolating the CTC track to the muon chambers and associating them using requirements in $r - \phi - z$ space. Thus we are able to identify muons and obtain muon momentum from the CTC for our analysis.

3.8 Trigger System and Data Acquisition System

The Trigger and Data Acquisition system of CDF is the system that selects interesting events, reads them from the detectors, and writes the experiment data to mass storage for our analysis.

During a run at CDF, the $p\bar{p}$ beams cross each other at the rate of 300 KHz. At Run IB's luminosity, such a crossing rate means a $p\bar{p}$ interaction rate of the order of 10^5 Hz. However, most of the interactions produce noise or "junk events" or uninteresting events that are not worth saving for offline processing. The amount of data written to the mass storage is kept at the rate of a few Hz due to the limit on hardware bandwidth. The rejection rate of the online events is 1 out of 5×10^4 .

Three levels of triggering are employed in CDF to realize such rejections. The trigger levels, as well as the data acquisition system, are controlled by the Trigger Supervisor (TS), the Buffer Manager (BM), and Timing Control (TC) (shown in Figure 3.14).

The following subsections describe the 3 trigger levels and the DAQ.

3.8.1 Level 1 Trigger

The Level 1 trigger is implemented entirely in hardware to make quick decisions based on primitive signatures of interesting events. It makes the decisions within $3.5\mu\text{s}$ between beam crossings so that the detector will catch up with the beam crossing frequency without causing a deadtime. The signatures the Level 1 trigger looks for include leptons with transverse energy exceeding a certain threshold, calorimeter energy clusters corresponding to jets above set thresholds, imbalance in the the energy

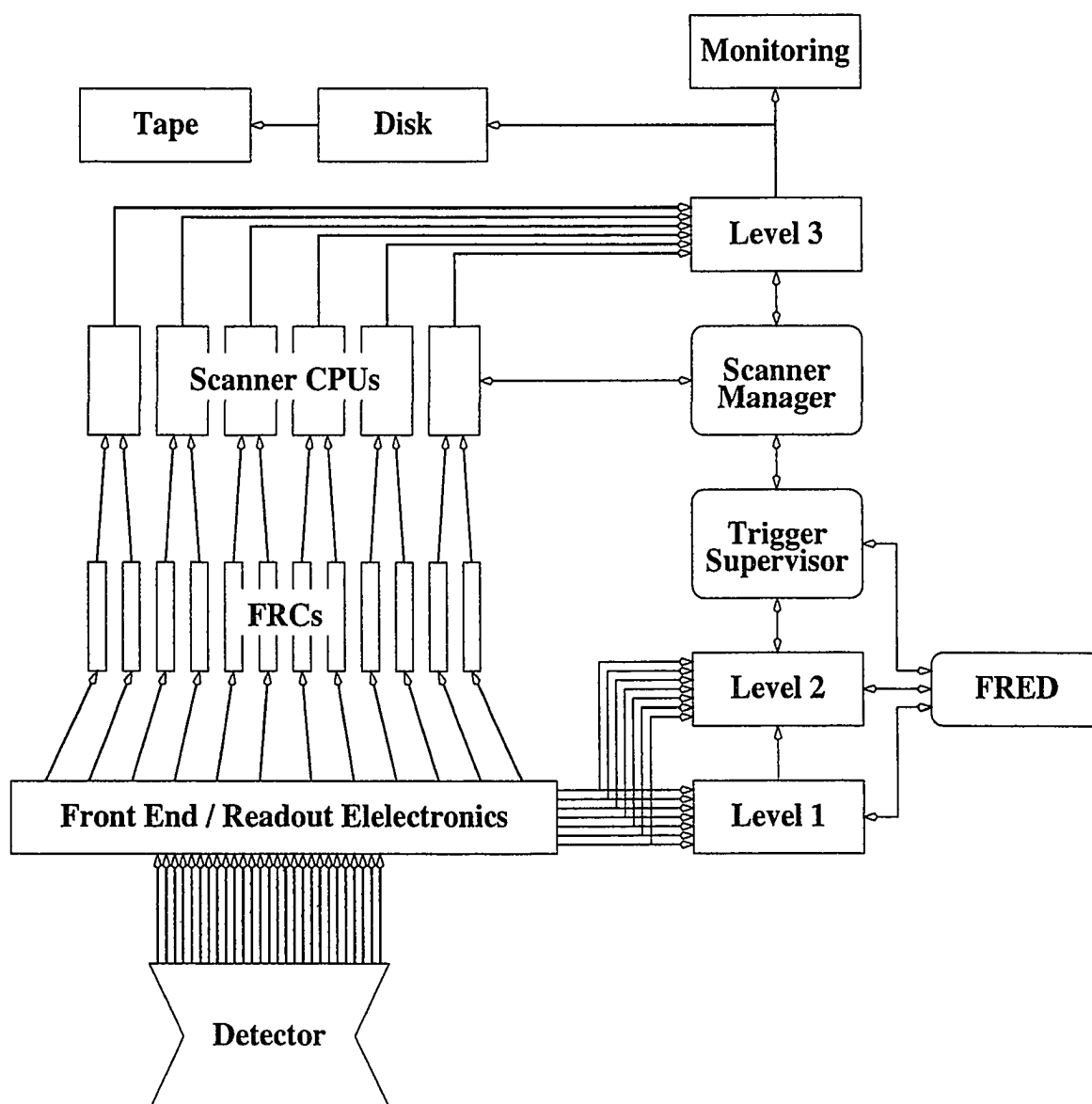


Figure 3.14: The DAQ (left hand side) and Trigger Systems (right hand side). Bold arrows show data flow, thin ones control lines and fast outputs. The Scanner Manager and Scanner CPUs are part of the hub feeding Level 3. “FRED” is logic combining Level 1 and Level 2 decisions. The Trigger Supervisor is the control system for the trigger logic through Level 2.

flow observed in the calorimeter, and beam-beam crossings, etc.

There are two categories of lepton triggers in Level 1: single lepton triggers with higher p_T thresholds and dilepton triggers with lower p_T thresholds. Muons are triggered upon muon system chamber signals with the requirement of the particle track passing close to the beam line. Electrons are triggered upon the observation of energy in the EM calorimeters and not in the hadronic calorimeters.

The calorimeter triggers in Level 1 are determined based on the fast analog outputs from the calorimeter towers. Fast algorithms are implemented in a series of hardware modules to process these signals. The majority of the events are required to exceed a 10 GeV total energy threshold to trigger.

The Level 1 rejection rate is about 1 out of 100, so after Level filtering, the event rate is of the order of 10^3 Hz.

3.8.2 Level 2 Trigger

The Level 2 trigger has two general purpose processors and triggers on the combined information from the fast outputs shared with Level 1, energy clusters in the calorimeters, stiff tracks in the CTC associated with muon stubs, and transverse energy imbalance integrated over the detector, etc.

The CFT [58] is a hardware track processor that uses the hit data in the CTC and performs 2-d track construction in the $r - \phi$ plane. It starts with the outermost CTC layer and searches for hits on layers further-in along helical wedges calculated in advance. More than 95% of all tracks that would coincide with the prompt hit found in the outmost layer are thereby included. These tracks are sorted into 16 bins in transverse momentum and 144 bins in azimuthal angle.

The Level 2 trigger looks at the fast outputs (analog signals split from the front end cards of DAQ) in more detail than the Level 1 and adds the Central Fast Tracker (CFT) track list. It constructs jets, missing transverse energy, photon candidates, and part of electron candidates using calorimeter information. However, due to the limited information available and the CFT's low resolution, the Level 2 trigger does not perform detailed kinematic calculations.

The trigger has a rejection factor of 10:1, reducing the total bandwidth of event rate from 1 kHz to about 100 Hz. Typical trigger rate is usually of the order of tens of Hz.

3.8.3 DAQ

The data acquisition system read out data from the subsystems of the detector and pass it to the Level 3 when L2A (Level 2 Accept) is issued. It consists hierarchy of electronic modules that read, repack the detector data and pass them on to the Level 3 computers. At the very front end of the DAQ, the analog outputs of the subsystems are amplified and digitized. Then custom readout boards read out these signals and send them to the Fastbus based modules to be concentrated. After the concentration, the Fastbus Readout Controllers (FRCs) read out these modules and passes the data on to a distribution hub where data are redistributed to the individual computers in the Level 3 computing farm.

3.8.4 Level 3 Trigger

The Level 3 trigger system uses 64 SGI (Silicon Graphics Challenge) processors to do the event rejection and reconstruction. These computers altogether are called the farm. Events are reconstructed in these processors with fast algorithms and screened with a set of filters before being written to the mass storage (tape drives). The rejection factor at Level 3 is about 3 : 1 and the trigger rate is reduced to 40 Hz at this stage.

The data written to the mass storage is later used for offline processing and detailed analysis for better understanding of the elementary particle physics.

Chapter 4

Method

4.1 Goals and Data Selection

The two purposes of our analysis are to determine the cross section for $b\bar{b}$ productions and to calculate the time integrated mixing parameter $\bar{\chi}$ for neutral B mesons produced at $\sqrt{s} = 1.8$ TeV. In CDF, the most suitable data for our analysis is the high-mass $\mu\mu$ (dimuon) data from $B\bar{B}$ inclusive decays.

We choose to use the data from semi-inclusive decay of $B\bar{B}$ mesons instead of the exclusive $B\bar{B}$ decays because the latter requires events to be fully-reconstructed and therefore reduces the event yield dramatically. A fully-reconstructed event is a event with all its products identified by the detector. Such a requirement makes the measurements clean and accurate because it is much less likely to have fake events when all decay products are identified and kinematic information of the decay products are available. However the strict criteria on triggering events cause heavy penalties on detection efficiencies on the charged tracks. On the other hand, semi-inclusive $B\bar{B}$ decays only require leptons in the decay product to be identified. It has much higher event yield because the branching ratio of semileptonic decays are reasonable large and leptons are easier to identify.

Considering the amount of data and capabilities of the analytical tools available in CDF Run IB, we choose to use semi-inclusive decays of $B\bar{B}$ to take advantage of rich statistics resulting from being able to lower the triggering threshold when two

leptons are required. The disadvantages of having more background in the dimuon data than in the exclusive decays will be made up for by proper offline data selection criteria and our impact parameter fitting method.

4.1.1 $b\bar{b}$ Production Cross Section

The $b\bar{b}$ production cross section in $p\bar{p}$ collisions is determined as follows:

$$\sigma(p\bar{p} \rightarrow b\bar{b}X) = \frac{N_{b\bar{b}}}{Br(b \rightarrow \mu X)^2 \times L \times A \times \epsilon_{CDF}} \quad (4.1)$$

Here

- $N_{b\bar{b}}$ is the total number of $b\bar{b}$ dimuon events obtained in the experiment after applying all selection criteria.
- $Br(b \rightarrow \mu)$ is the branching ratio for the semileptonic decay of B hadron.
- L is the integrated luminosity.
- A is the dimuon acceptance. It is the ratio of the dimuon events that can be observed within the geometrical and kinematic regions covered by the detector to the overall number of dimuon events that was produced with the luminosity L . Equation 6.1 shows the definition of A .
- ϵ_{CDF} is the combined detector and data selection efficiency. It is the fraction of the final number of dimuon events, i.e. those actually observed in the detector and passing all the selection criteria, to the dimuon events observed within the geometrical and kinematic regions covered by the detector.

We can obtain these numbers as follows:

- The number of dimuon pairs $N_{b\bar{b}}$ surviving all criteria are obtained with Impact Parameter Fitting method described in the next section. The main idea is to distinguish muons from b quark from the other muons and background by taking advantage of the long lifetime property of B mesons.
- The branching ratio $Br(b \rightarrow \mu = 0.1058 \pm 0.0018)$ is available in Reference [2].

- The quantity of luminosity L can be obtained by running a standard procedure through the dimuon data set to sum up the individual luminosities of each file. Only the runs considered “Good” enter the calculations. (A “good” run is determined at the end of each run of Run IB. It requires a series of checks for each subsystem, such as whether actual $p\bar{p}$ collisions occurred, whether the trigger system was working, etc., to make that determination.) Our calculation shows $L = 88.0 \pm 3.5 pb^{-1}$ during the CDF Run IB period (8/93 - 8/95)
- The acceptance A is obtained by running Monte Carlo Simulations of $p\bar{p}$ collisions. By letting the generated muons fly through a simulated CDF detector and counting the fraction of muons falling into the acceptance region, we are able to calculate the value of A .
- The efficiency ϵ_{CDF} is a product of a series of efficiencies due to the loss of events in different parts of the detector, such as the SVX, CTC, CMU, etc. The calculations of these factors will be carried out in the following chapters.

Once we are able to obtain these numbers, we will be able to calculate $\sigma(p\bar{p} \rightarrow b\bar{b}X)$. Furthermore, in fact, in our analysis, we also calculated the cross sections in different b quark transverse momentum bins.

4.1.2 The Time Integrated Mixing Parameter $\bar{\chi}$

In principle if a dimuon pair can only be generated by a $b\bar{b}$ pair through the process $b \rightarrow \bar{B}^0 \rightarrow \mu^-$ and $\bar{b} \rightarrow B^0 \rightarrow \mu^+$, i.e. both quarks go through direct semileptonic decay, then the two muons should be of opposite charge 100% of the time. However, experimentally this is not the case. We see about one third of our dimuon events are with the muons of the same charge. Such events with same-charge muons are called Like-Sign events (LS). (We call the dimuon events with muons of opposite charges Opposite-Sign events (OS).) There are several sources of LS $b\bar{b}$ events. Here are some examples:

- The mixing of B^0 with \bar{B}^0 . When a mixing happens in one leg of the dimuon event, for example, $b \rightarrow \bar{B}^0 \rightarrow B^0 \rightarrow \mu^+$ in one leg and $\bar{b} \rightarrow B^0 \rightarrow \mu^+$ in the

other leg, we have a muon pair of the same positive charge (LS). If the mixing happens to both legs, then we have a OS which is indistinguishable from a OS event from two direct decays.

- Sequential semileptonic decays of the b quark. For example, $b \rightarrow \bar{B}^0 \rightarrow D^+ \rightarrow \mu^+$ in one leg and direct decay in the other leg create a LS muon pair. If the other leg is not undergoing direct decay, (for instance when mixing or sequential decay happens), then we have an OS event again.
- The decay depicted in Figure 4.1 happening in one leg and a mixing or sequential decay happening in the other leg creates a LS event.

In fact, since each leg of the $b\bar{b}$ event decays independently in one of the 4 modes:

- Direct Decay
- Mixing
- Sequential Decay
- Special Case of Figure 4.1

we have a combination of 4×4 modes for a $b\bar{b}$ dimuon pair. To simplify the problem, we define the ratio r_{ws} , called the Wrong-Sign cascade ratio, as $r_{ws} = N_{ws}/N_{rs}$, where N_{ws} is the number of muons that carry an opposite electric charge from its ancestor b quark and N_{rs} is the number of the muons that carry the same sign of electric charge as its ancestor b quark. The source of N_{ws} is normal sequential decays: $b \rightarrow c \rightarrow \mu$ (including $b \rightarrow c \rightarrow \tau \rightarrow \mu$). The source of N_{rs} includes:

- Direct decay $b \rightarrow \mu$
- The case of $b \rightarrow \tau \rightarrow \mu$ where muon comes from a τ from direct B decay.
- The case of $b \rightarrow c, \bar{c}$ and $\bar{c} \rightarrow \mu^-$ as depicted in Figure 4.1.

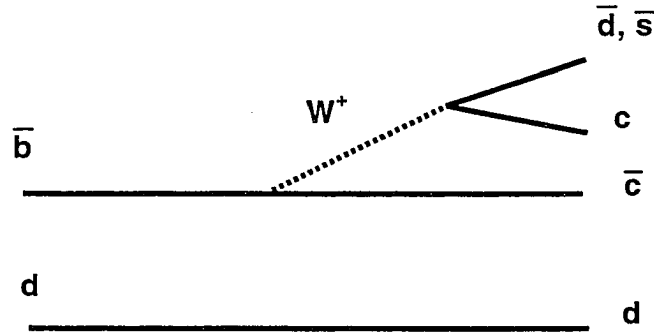


Figure 4.1: Feynman Diagram showing $b \rightarrow c, \bar{c}$. This process produces a muon carrying the same sign of charge as its ancestor b quark without going through a direct decay.

We do not include the mixing effects in r_{ws} because it is what we are going to measure.

We define the ratio of LS $b\bar{b}$ event to OS $b\bar{b}$ events as $R = \frac{N_{LS}}{N_{OS}}$. R is experimentally measurable with our Impact Parameter Fitting Method described in the next section. We could calculate R if we knew the time integrated mixing parameter $\bar{\chi}$ and the Wrong-Sign cascade muons ratio r_{ws} . Since r_{ws} includes all the other effects except mixing, the probabilities of get a wrong-sign or right-sign $b \rightarrow \mu$ are described in Table 4.1.

	Right Sign	Wrong Sign
Probability	$1/(1 + r_{ws})$	$r_{ws}/(1 + r_{ws})$

Table 4.1: Right Sign, Wrong Sign Probabilities

The probabilities of mixing and non-mixing are listed in Table 4.2. Since mixing happens independently of the decays, the combined probabilities are listed in Table 4.3. With two muons decaying and mixing independently, in Table 4.4, we can cal-

	Mix	No Mix
Probability	$\bar{\chi}$	$1 - \bar{\chi}$

Table 4.2: Mixing, No Mixing Probabilities

	Probability
Mixing + Wrong Sign	$P_{mw} = r_{ws}/(1 + r_{ws}) \times \bar{\chi}$
No Mixing + Wrong Sign	$P_{nw} = r_{ws}/(1 + r_{ws}) \times (1 - \bar{\chi})$
Mixing + Right Sign	$P_{mr} = 1/(1 + r_{ws}) \times \bar{\chi}$
No Mixing + Right Sign	$P_{nr} = 1/(1 + r_{ws}) \times (1 - \bar{\chi})$

Table 4.3: Dimuon Charge Combination

culate the probabilities of each cell by multiplying the corresponding probabilities in Table 4.3. In Table 4.4, we add up the probabilities in all the LS cells and divide the sum by the sum of the OS cells to get the result in Equation 4.2).

$$R = \frac{N_{ls}}{N_{os}} = \frac{2r_{ws}(\bar{\chi}^2 + (1 - \bar{\chi})^2) + 2\bar{\chi}(1 - \bar{\chi})(1 + r_{ws}^2)}{(\bar{\chi}^2 + (1 - \bar{\chi})^2)(1 + r_{ws}^2) + 4r_{ws}\bar{\chi}(1 - \bar{\chi})} \quad (4.2)$$

Since r_{ws} can be obtained in Monte Carlo simulations, by putting R and r_{ws} into equation 4.2, we can then determine $\bar{\chi}$.

4.2 Impact Parameter Fitting Method

In the last section, we described the approaches to calculate our $b\bar{b}$ production cross section and $\bar{\chi}$. Both calculations need a very important input: the number of $b\bar{b}$ dimuon events in our data. However, despite the fact that our dimuon data set has an abundance of $b\bar{b}$ events, there are many other sources of “dimuon” events co-existing with these $b\bar{b}$ events. The many sources of “dimuon” events are described in Chapter 5 of this thesis. This hotchpotch of “dimuon” components should be studied carefully and the dimuons from $b\bar{b}$ ’s should be separated from the other signals and counted.

		μ_1			
		Mixing+ Wrong Sign	No Mixing+ Wrong Sign	Mixing+ Right Sign	No Mixing+ Right Sign
μ_2	Mixing+ Wrong Sign	$P_{mw} \times P_{mw}$ OS	$P_{mw} \times P_{nw}$ LS	$P_{mw} \times P_{mr}$ OS	$P_{mw} \times P_{nr}$ LS
	No Mixing+ Wrong Sign	$P_{nw} \times P_{mw}$ LS	$P_{nw} \times P_{nw}$ OS	$P_{nw} \times P_{mr}$ LS	$P_{nw} \times P_{nr}$ OS
	Mixing+ Right Sign	$P_{mr} \times P_{mw}$ OS	$P_{mr} \times P_{nw}$ LS	$P_{mr} \times P_{mr}$ OS	$P_{mr} \times P_{nr}$ LS
	No Mixing+ Right Sign	$P_{nr} \times P_{mw}$ LS	$P_{nr} \times P_{nw}$ OS	$P_{nr} \times P_{mr}$ LS	$P_{nr} \times P_{nr}$ OS

Table 4.4: The independent decay and mixing in both of the dimuon legs result in LS and OS dimuon events. Summing up the LS cells and dividing it by the sum of the OS cells gives Equation 4.2.

The biggest difference between the $b\bar{b}$ dimuons and the other components is in their impact parameters. The impact parameter, IP, of the track of a decay product is defined as the distance of the closest approach from the track to the primary vertex (where the $p\bar{p}$ interactions happen) of the collision in the transverse plane. As indicated in Figure 4.2, the impact parameter depends on the decay length, i.e., the distance from the primary vertex to the secondary vertex, of the parent particle. The decay length is equal to $\beta\gamma c\tau$ where $\beta\gamma$ is the Lorentz boost of the parent particle and τ is its lifetime at $\beta = 0$. Therefore:

$$IP = \beta\gamma c\tau \sin \delta \quad (4.3)$$

The longer the parent particle lifetime is, the larger impact parameters the tracks of its decay products tend to have.

Theoretically, the IP distribution can be calculated as:

$$\frac{dN}{dIP} = \frac{1}{2} \int \sin(2 \tan^{-1} \frac{y}{z}) \frac{2}{1 + (\frac{y}{z})^2} \frac{1}{cz\tau} e^{-z} dz \quad (4.4)$$

Here $\frac{dN}{dIP}$ is the differential distribution of IP, t is the proper decay time, τ is the lifetime of the parent particle, $z = t/\tau$ and $y = IP/c\tau$. However, experimentally,

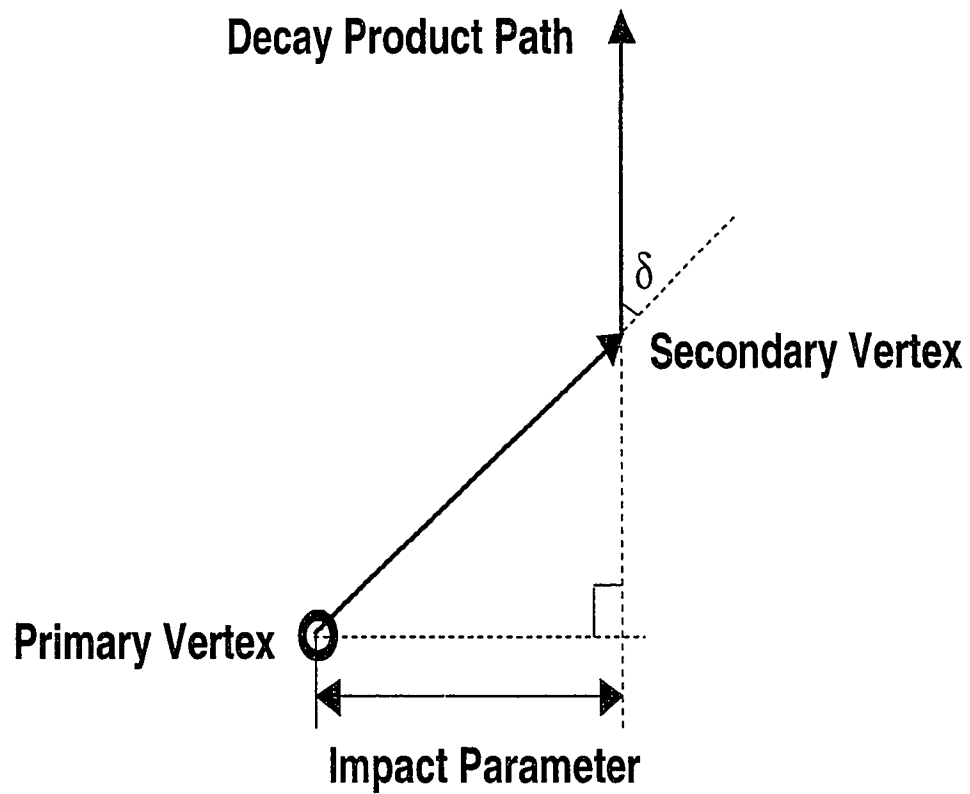


Figure 4.2: The Impact Parameter is defined as the shortest distance of the primary vertex to the decay product track. The distance from the primary vertex to the secondary vertex is called the decay length and is proportional to the lifetime of the particle.

the observed distribution is different because the geometric coverage of the detector is only for low rapidity and the tracking errors, the beam spot spread, etc. cause deviation of the IP distribution from the theoretical case. Therefore we will need to use Monte Carlo simulations to estimate the IP distribution relevant to our analysis.

Classified by Impact Parameter, the components in the dimuon data fall into three categories: bottom muons (b), charm muons (c) and prompt source tracks (j). Bottom muons are muons from B hadron decay products. Charm muons are muons from D hadron decays. The prompt source tracks are usually background signals from different origins such as hadronic punchthroughs or decay-in-flight muons, etc. A large portion of the prompt tracks are fake muons, i.e., particles passing all the muon criteria but are not muons.

Due to the long lifetime of bottom hadrons, the Impact Parameter of tracks from B 's are much larger than tracks from D and the tracks from prompt source. Therefore, it is natural to use statistical fitting to extract the fraction of $b\bar{b}$ dimuons from the rest of the components. Figures 4.3 4.4 and 4.5 show the impact parameter distributions of these components. We produced the b and c components via Monte Carlo simulations and the j component using data from the experiment.

The first step of the Impact Parameter Fitting Method is to prepare the templates for the fitting. We will describe the details of how to prepare the impact parameter distributions in Figures 4.3, 4.4 and 4.5 in the next Chapter. The Monte Carlo method we use to get the b muon IP distribution template have default values for the B hadron species fractions and b decay branching ratios that are different from the world average numbers. We therefore need to reweight their fractions properly according to the correct B fractions in the B mixture. The weighting factors are obtained by running side-check Monte Carlo simulations which will be discussed in the following chapters. With these IP distribution templates ready, we need to smooth them into curves because the template histograms are based on limited number of observations. By smoothing the distributions we can eliminate the statistical fluctuations in the histograms and carry out more accurate fittings. The method we use is an extension of Nadaraya-Watson kernel smoothing which is described in detail in Appendix A. The results of the smoothing are shown in Figure 4.6.

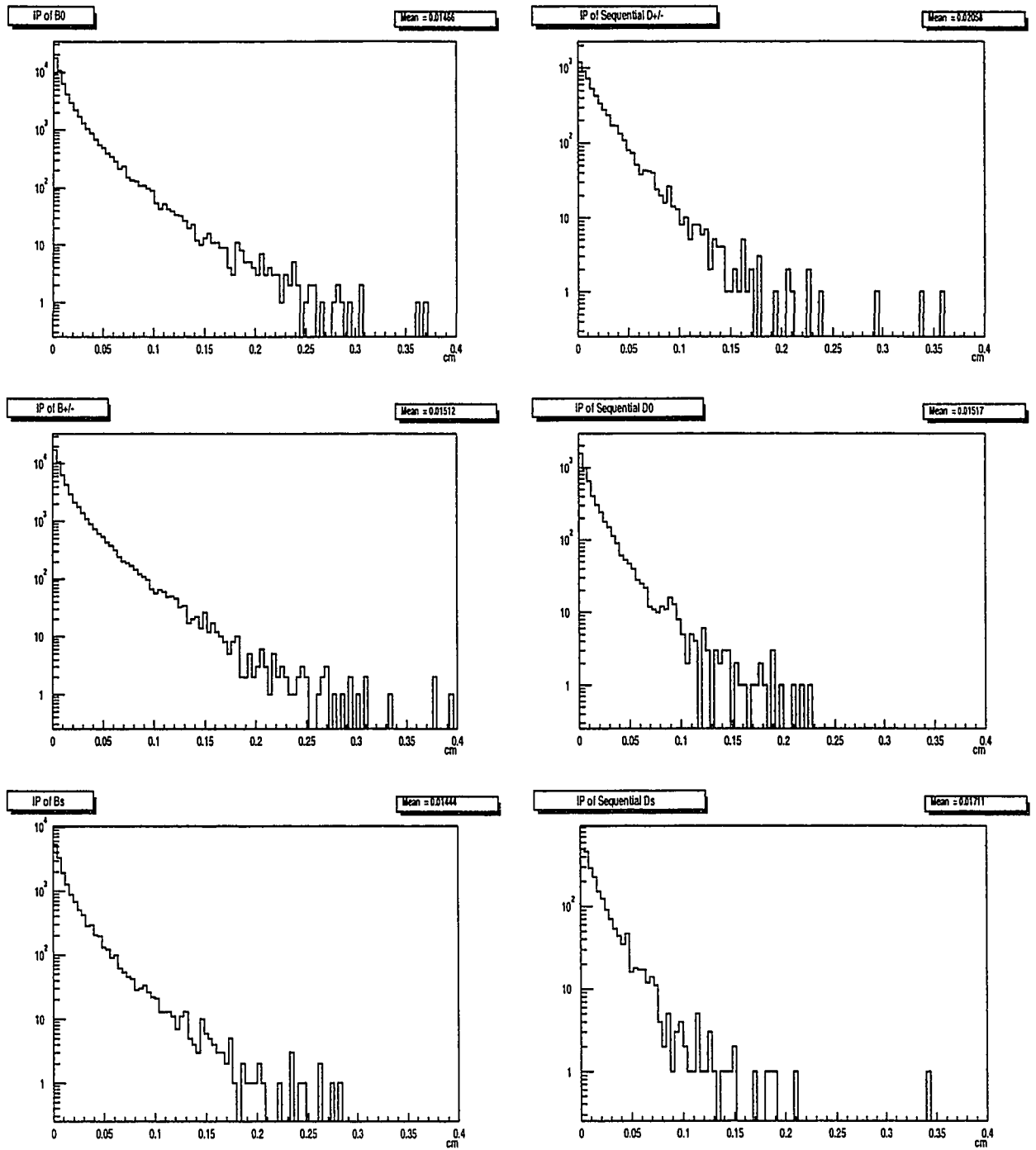


Figure 4.3: The IP distribution of muons of direct and sequential b decays (cm)

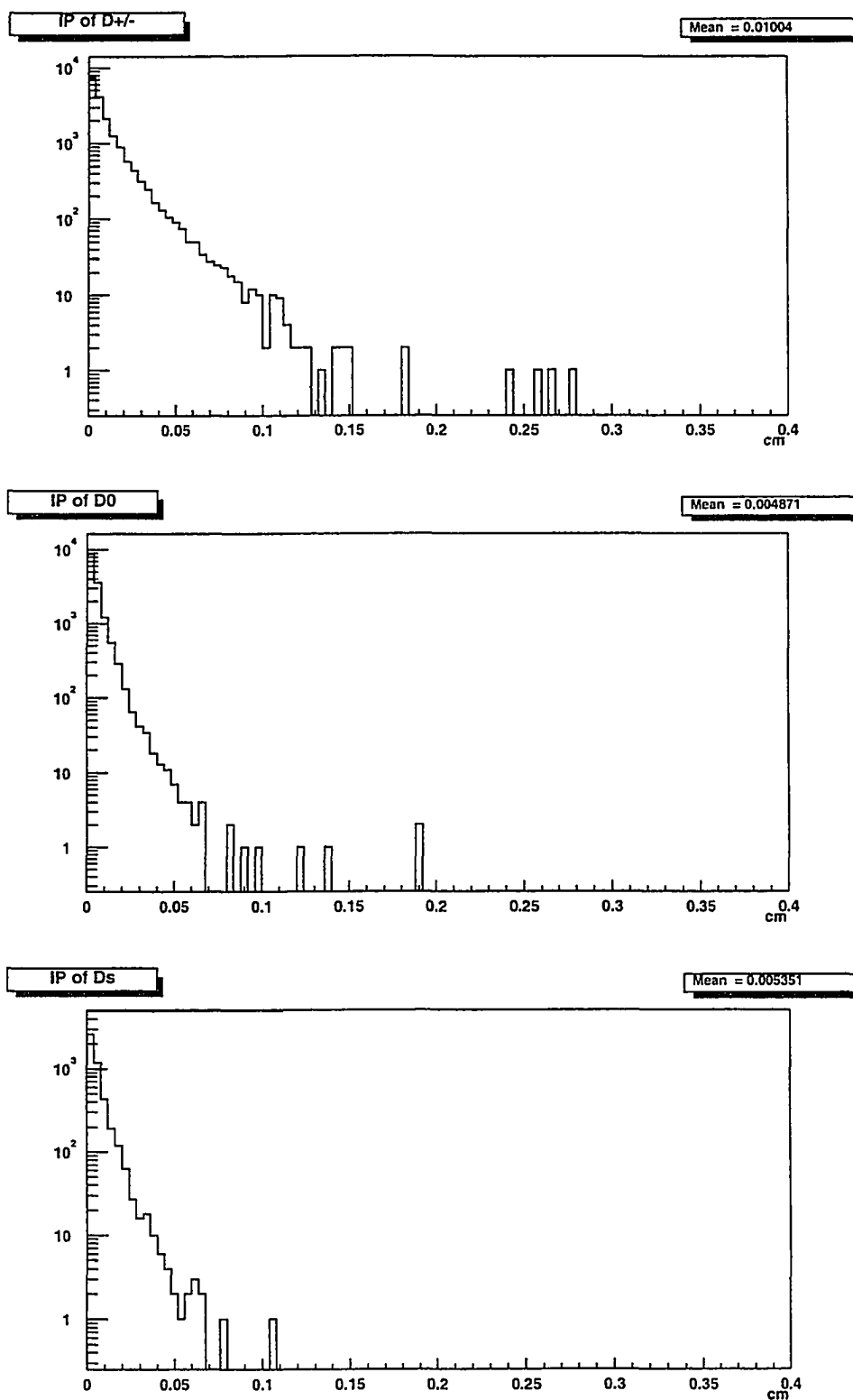


Figure 4.4: The IP distribution of muons of direct c decays (cm)

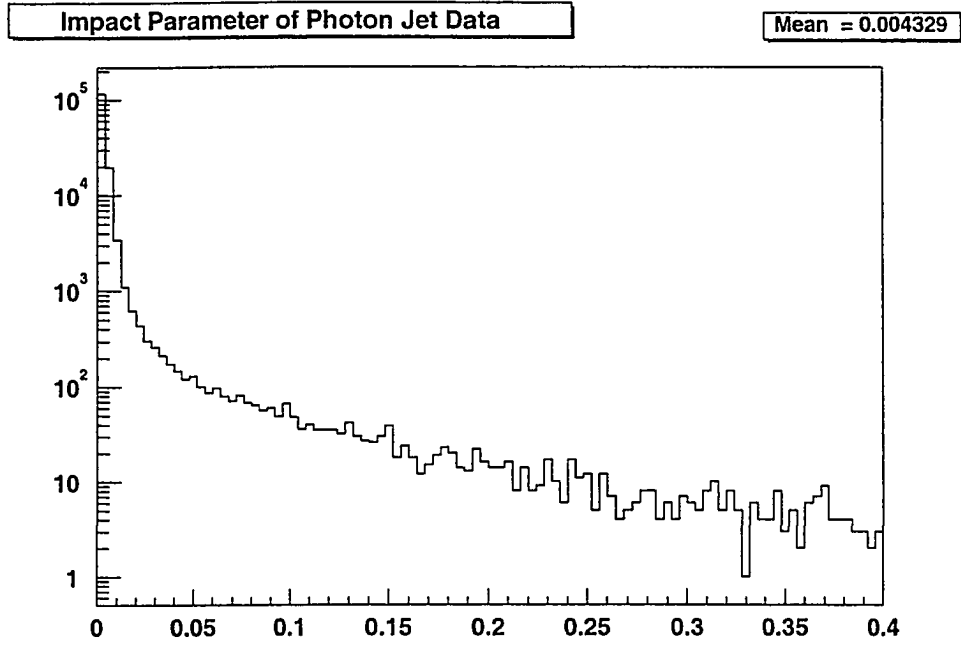


Figure 4.5: The IP distribution of tracks in Photon Jet Data

The smoothed curves have incorporated knowledge of the IP distribution that are not available in the Monte Carlo simulations. For example, IP distribution should have good monotonicity in the measured region and should not have large fluctuations. Therefore the smoothed curves are better approximation of the real IP distribution and will be used for the fittings in our analysis.

The next step is to create the 2-dimensional impact parameter distribution templates. That is because we have 2 muon candidates for each event and either candidate can be from one of the 3 possible sources: b , c and j . Since each muon comes from an independent chain of decays, we assume there are no correlations in the IP distribution between the two muons, i.e., the impact parameter of one muon does not depend on the impact parameter of the other muon. Therefore we can calculate the 2-dimensional distribution by convoluting the 1-dimensional distributions. The smoothed and normalized one-dimensional impact parameter distributions of b muons, c muons and tracks from prompt sources are defined as $f_b(x)$, $f_c(x)$, and $f_j(x)$.

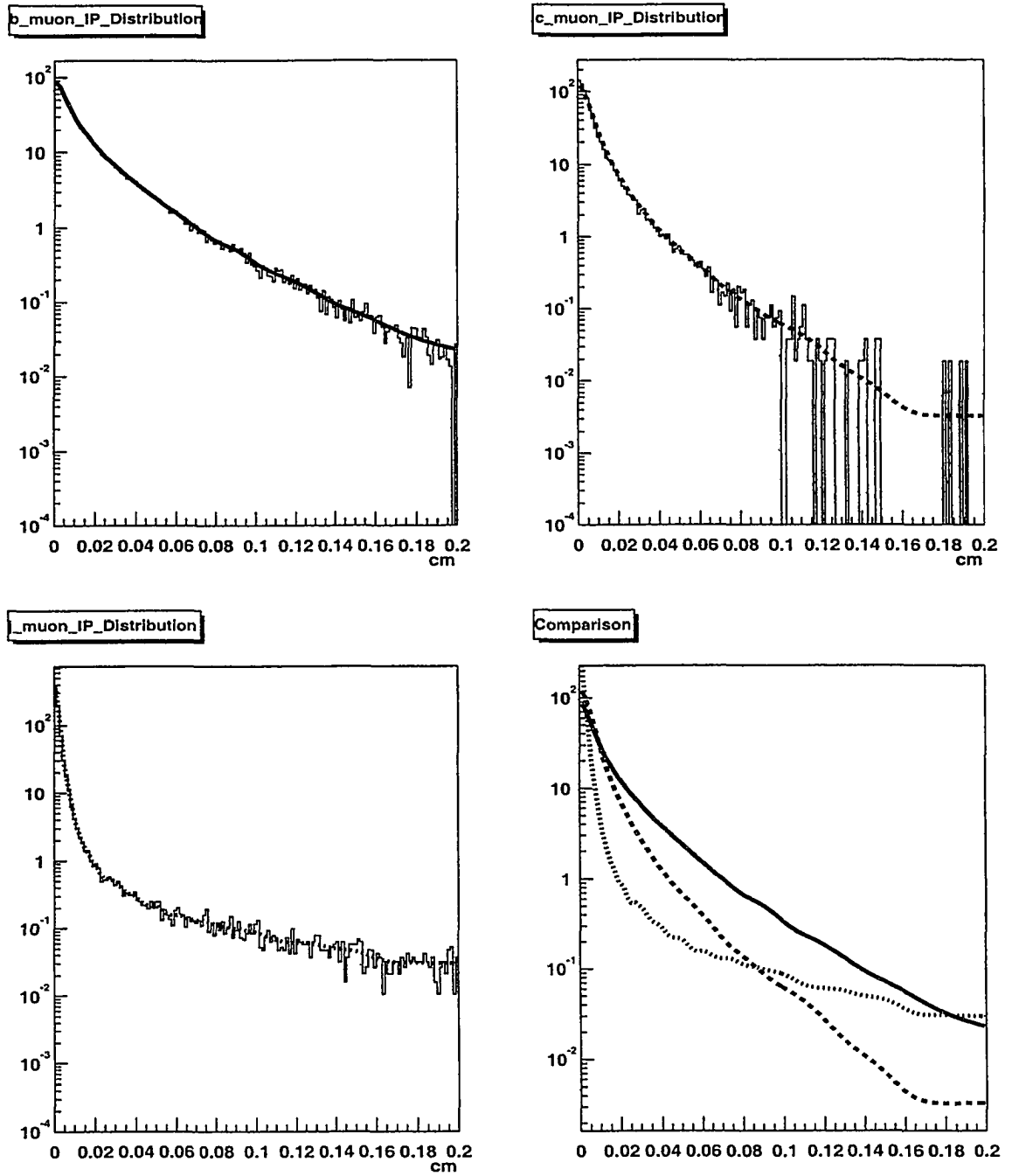


Figure 4.6: Normalized and smoothed Impact Parameter Frequency Distributions for the three types of components and their comparison. As we can see, *b* muons have the longest impact parameters.(X axis are in cm)

They are convoluted in the following way:

$$\begin{aligned}
f_{bb} &= f_b(x) \times f_b(y) \\
f_{cc} &= f_c(x) \times f_c(y) \\
f_{jj} &= f_j(x) \times f_j(y) \\
f_{bj} &= (f_b(x) \times f_j(y) + f_b(y) \times f_j(x))/2 \\
f_{cj} &= (f_c(x) \times f_j(y) + f_c(y) \times f_j(x))/2
\end{aligned} \tag{4.5}$$

Here x and y are the impact parameters of each of the muons. There are actually 6 possible combinations but f_{bc} is not used because it is not likely that an event can have direct b muons and c muons at the same time. The f_{bj} and f_{cj} are formulated in such a way as to obtain symmetry between x and y because there is no preference in choosing the order of the two muons in our data. The factor of $1/2$ in their formulas are used to keep $\int f dx dy = 1$.

Figure 4.7 shows the 5 convoluted templates: bb , cc , jj , bj and cj . They are the templates used in fitting the dimuon data.

Since the 5 templates (bb , cc , jj , bj , cj) have different impact parameter (IP) distribution, we use a linear combination of these 5 templates to fit the dimuon data's impact parameter frequency distribution as indicated in Equation 4.6.

$$f_{\mu\mu} = c_0 \times f_{bb} + c_1 \times f_{cc} + c_2 \times f_{jj} + c_3 \times f_{bj} + c_4 \times f_{cj} \tag{4.6}$$

Here $f_{\mu\mu}$ is the dimuon data IP distribution. The c_i 's are the fractions of each component.

The method that we use for the fitting is Unbinned Maximum Log-Likelihood fitting. The log likelihood function we use is:

$$L = -2 \times \sum \ln(c_0 \times f_{bb} + c_1 \times f_{cc} + c_2 \times f_{jj} + c_3 \times f_{bj} + c_4 \times f_{cj}) \tag{4.7}$$

with the constraint $c_0 + c_1 + c_2 + c_3 + c_4 = 1$. Here, the sum is taken over all the dimuon events. We minimize the likelihood function by changing the c_i 's while keeping the sum of them to be 1. The c_i 's giving the minimum L will be our best estimation of the fractions of the 5 components in our dimuon data sample. We use the software package MINUIT [59] from the CERN library to calculate the optimum fractions

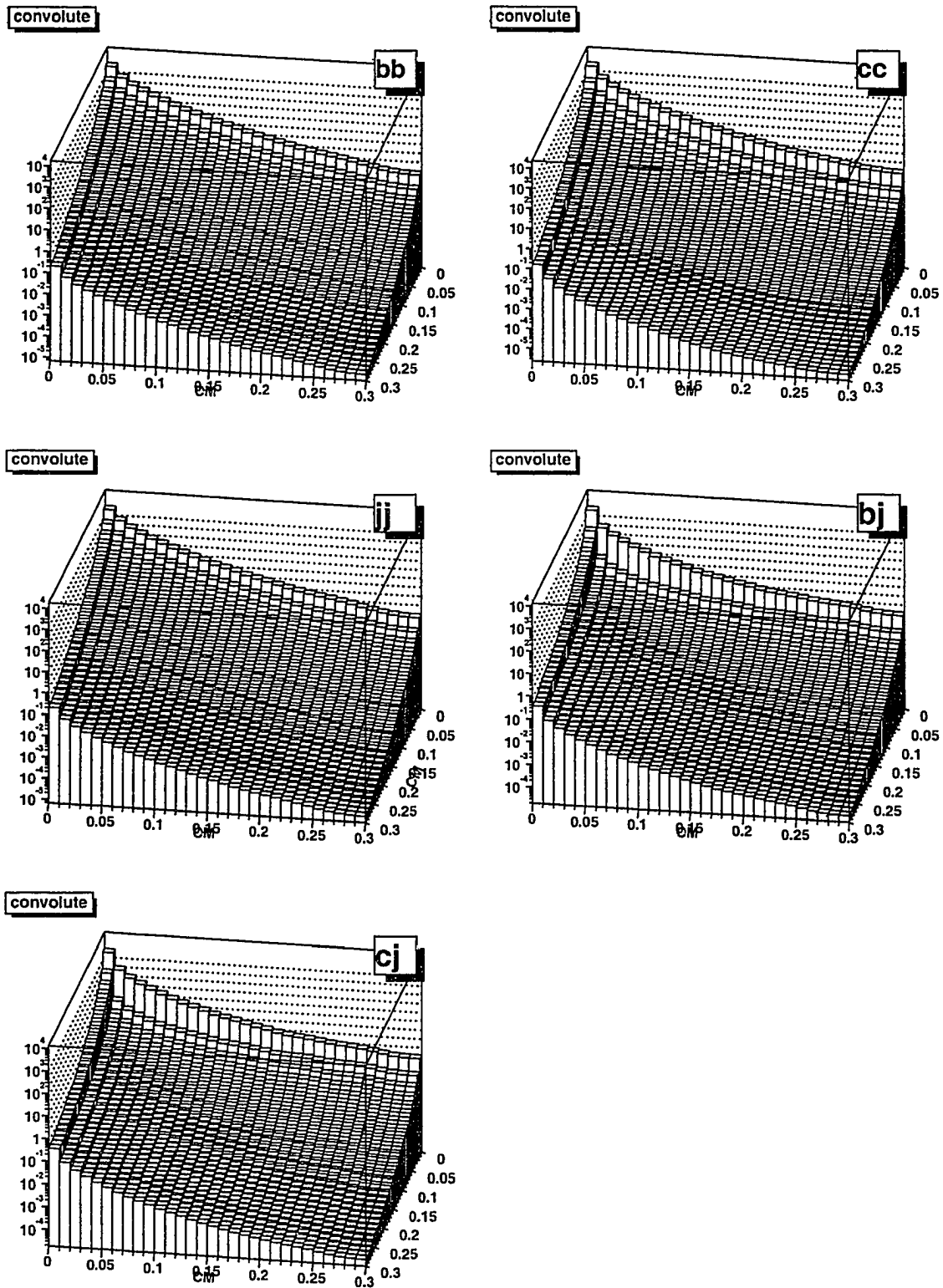


Figure 4.7: 2-d Impact Parameter Frequency Distributions of the 5 templates. (x, y are in cm)

and use the uncertainties returned by MINUIT as our statistical uncertainties for the fractions. Since we choose L to be the Log sum times 2, the uncertainties returned from the MINUIT corresponds to one sigma deviation.

To validate our method, we try to fit a mock data sample which is composed of 5000 bb events, 5000 cc events, and 5000 jj events. The fitter gives the result in Figure 4.8. The result shows that the percentage of the bb and cc and jj are close to 1/3 within errors. There are clearly nontrivial correlations in the low impact parameter components: cc, jj, bj and cj. This results in inaccuracies in the fractions of those components. But for high impact parameter components, especially $b\bar{b}$ muons, the fraction is quite accurate.

With the Impact Parameter Fitting method, we are able to obtain the $b\bar{b}$ dimuons fraction in the Dimuon data and carry out the calculations of $b\bar{b}$ generation cross section and the time integrated mixing parameter $\bar{\chi}$.

The TEST fitting results(5par): (Projected to one dim)

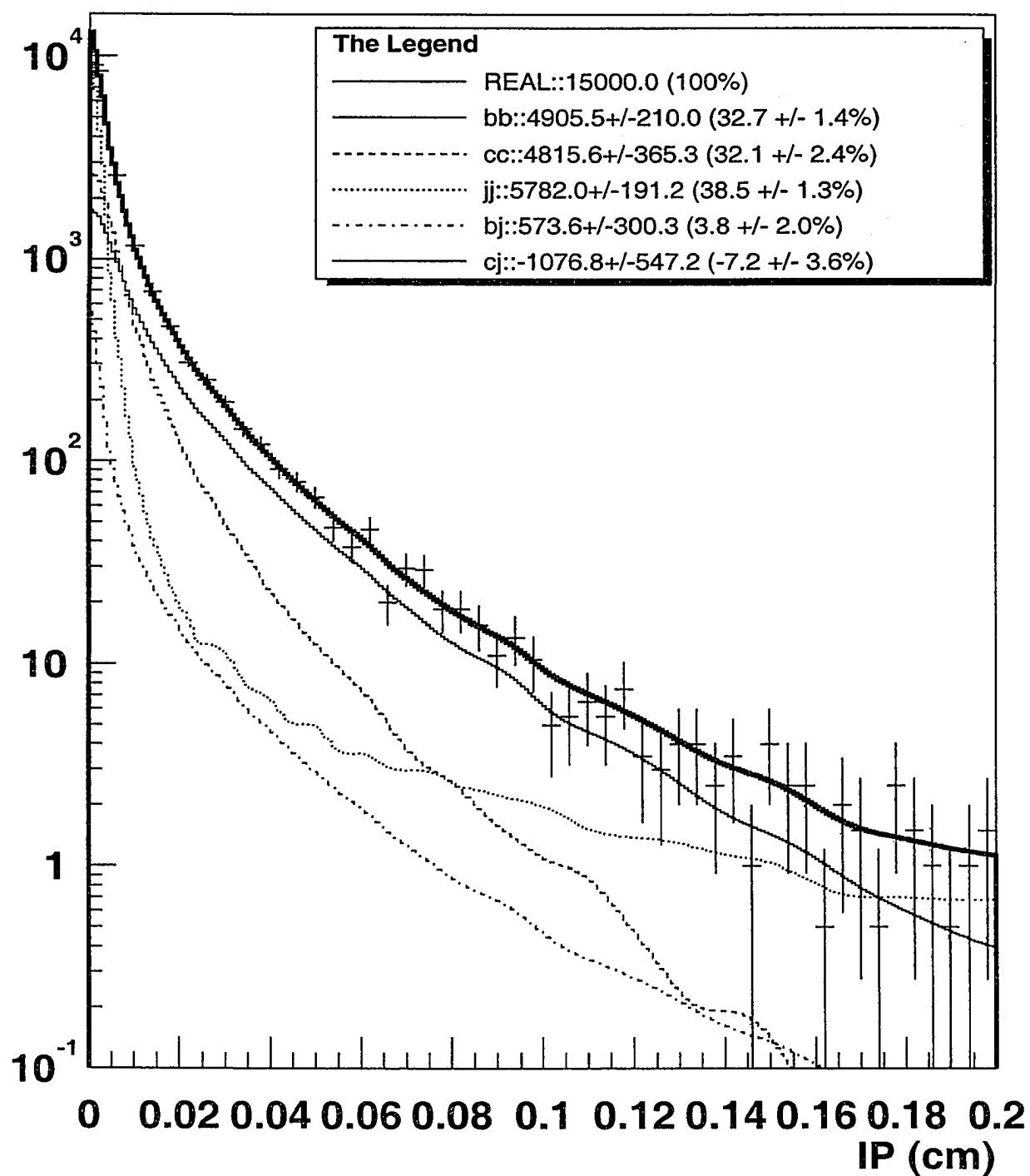


Figure 4.8: Fit of data sample of mixture of 5000 bb, 5000 cc and 5000 jj events

Chapter 5

Data

This chapter describes the data set we use in our analysis. The first section describes the dimuon data set measured in CDF Run IB. The second section describes the way in which we generate our Monte Carlo data sets. The third section describes a data set obtained from CDF Run IB and used for generating our prompt source IP templates.

5.1 Dimuon Data

5.1.1 The Sources of Dimuon Data.

The dimuon data we use for this analysis is the data collected during CDF Run IB which lasted from 1993 to 1995 and had a total luminosity of $88.0 \pm 3.5 \text{ pb}^{-1}$. We stripped our dimuon data from the RUN-IB data set *BHMB_5B* (high-mass $\mu - \mu$ data) of stream B. The Level 2 trigger for this part of data is called TWO_CMU_TWO_CFT_2_2 and the Level-3 trigger for this data is called PSIB_DIMUON_HIGHMASS_V1. Altogether 15549 files are listed in the *BHMB_5B* directory and the integrated luminosity is $88.0 \pm 3.5 \text{ pb}^{-1}$.

The instantaneous luminosity is measured using the Beam-Beam Counters described in Chapter 3. It is defined as:

$$L = \frac{BN_p N_{\bar{p}}}{4\pi\sigma^2} \quad (5.1)$$

Here B is the bunch crossing rate which is about one crossing per $3.5\mu\text{s}$. The two N 's are the number of protons and antiprotons per bunch. Both N 's are about the order of 10^{10} . The parameter $\sigma \sim 35\mu\text{m}$ is the standard deviation of the Gaussian distribution of the beam spot in the transverse plane.

The dimuon data generated in $p\bar{p}$ collisions at $\sqrt{s} = 1.8 \text{ GeV}$ has the following origins:

- Bottom decays:

A large portion of the muon pairs in the dimuon events come from the $b\bar{b}$ pairs produced in the $p\bar{p}$ collisions. These include both direct and sequential b decays. In most cases each b quark in the $b\bar{b}$ pair produces one muon of the muon pair. However, there are decays in which $b \rightarrow \mu_1 c X$ and then $c \rightarrow \mu_2$. This type of decay of a single quark produces two muons simultaneously. When the other quark did not produce a muon, we could have a “dimuon” event. We need to remove such events from our data set. To remove them we need simply to apply a mass cut, i.e., to remove all the dimuon events with invariant mass less than that of a B meson ($\sim 5 \text{ GeV}/c^2$).

- Fake muons from Bottom Decays:

When $b \rightarrow \mu X$, the by products in X have a probability of being mistaken as muons by the detectors. These fake muons have similar geometric and kinematic properties as real muons and are therefore difficult to remove completely. In Section 6.3.6 we discuss in detail the method of estimating these fake muons.

- Charm decays:

Dimuons can be produced by the semileptonic decays of $c\bar{c}$ pairs in the following way:

$$c \rightarrow \mu^+, \bar{c} \rightarrow \mu^- \quad (5.2)$$

In $p\bar{p}$ collisions, large numbers of $c\bar{c}$ pairs are produced as well as $b\bar{b}$ pairs. The semileptonic decay $c \rightarrow \mu\nu X$ branching ratio is about 9% [32] and is close to that of semileptonic decay of b 's. Even though the p_T spectrum of produced c quarks is much softer than that of b 's, we could still have a considerable contribution of $c\bar{c}$ dimuons.

- Decay in Flight(DIF) of π and K :

The $p\bar{p}$ collisions produce a significant number of pions and kaons. The pions and kaons decay into muons with very high branching ratios ($\sim 99.99\%$ and $\sim 68\%$ respectively). These are called Decay-in-Flight muons. These muons should have very large impact parameters due to the very long life time of the π 's and K 's ($\tau_\pi = 2.6 \times 10^{-8}s$, $\tau_K = 1.24 \times 10^{-8}$). However, in our detector, if a hadron decays in CTC, some of the trajectories will have large kinks and therefore be rejected by the CDF offline tracking selections that accepts only smooth helical trajectories. Therefore most of the DIF muons are removed and the remaining muons show an impact parameter distribution similar to that of prompt tracks.

- Hadronic Punchthroughs:

The pions and kaons produced in the collisions can also be identified as muons themselves. They can punch through the calorimeters and reach the muons chambers. The secondary hadrons produced by particles interacting with the media could also be identified as muons. These are all called hadronic punchthroughs. There are 5 interaction lengths in calorimeter between the collision point and CMU and another 3 interaction lengths are added by the steel shield between CMU and CMP. Even with such shielding, we still expect a portion of our "dimuon" data to be such punchthroughs. These punchthroughs have small impact parameters because they are generated from the $p\bar{p}$ collision spot.

- Electroweak Processes:

In $p\bar{p}$ collisions, $q\bar{q}$ can annihilate to produce a virtual photon or a Z^0 , and then a muon pair are generated as a result of this annihilation.

- Υ Decay

A certain amount of bottomonia (Υ 's) are created in the collisions. The bottomonium states Υ ($1S$), ($2S$) and ($3S$) can decay into muons by way of $\Upsilon \rightarrow \mu^+\mu^-$, thus being eligible for entering our dimuon data set. These muons are close to prompt because the Υ states decay almost instantly after they are created in the collisions.

- Cosmic Rays

Cosmic rays pass uniformly in the detector. The track of a cosmic ray particle entering and then leaving the detector can be mistaken to be two tracks of opposite charge, both leaving the detector. They can enter our dimuon data set as well. However the number of the cosmic ray particles is small and the kinematic features of cosmic particles make them easy to identify. For example, the two tracks share the same impact parameter (distance from the collision spot to the track) because they are in fact different sections of the same track. Also, unlike the tracks generated in the collisions which concentrate around the beam spot, the cosmic tracks uniformly exist in the detector and are easy to be separated from the rest part of the dimuon data.

- Combinations of the Above

A dimuon event has two legs. Each leg could be from any one of the sources listed above. For example, one leg is from B direct decay and the other leg is from π punchthrough, etc. These events should also be accounted for in our dimuon data set.

In order to purify our dimuon data set, we need to apply both online and offline data selection criteria.

5.1.2 Online Data Selection Criteria

As we have described in the Apparatus Chapter, the CDF trigger system has 3 levels. They each filter the dimuon data with certain criteria. Higher levels of the trigger system require more constraints or more refined criteria and are allotted more time to do so. At each trigger level, there are different types of triggers designed to fit different research interests. The triggers that we need are called dimuon triggers.

- The Level 1 dimuon trigger requires 2 muon segments to be found in CMU and each muon segment has $p_T > 3 \text{ GeV}/c$. Here p_T is measured via the drift time difference between CMU detector layers and is not the most accurate p_T we can achieve in our experiment. This type of p_T measurement is chosen for

the Level 1 trigger system because it is relatively more convenient and fast to calculate the drift time difference in CMU and thus avoids deadtime. Due to the crudeness in the p_T measurement, there are inaccuracies in the Level 1 data selections. The higher level triggers will make up for these inaccuracies.

- The Level 2 dimuon trigger we use is called *TWO_CMU_TWO_CFT_2.2*. It requires both of the muon segments in CMU to match a track in CTC and p_T of the muon segments to be greater than 2 GeV/c. The CTC tracks are matched to the muon segments by the Central Fast Tracker (CFT)[60]. The CFT is a hardware track processor using fast hit information from the CTC to calculate the particle p_T with a resolution of $\delta p_T/p_T = 0.035p_T$. CFT matches a CTC track and a muon segment in CMU when the ϕ is within 15° . This match has an efficiency of close to 1, therefore the Level 2 trigger efficiency is solely dependent on CFT, which is about 92.5% for $p_T \geq 3$ GeV/c.
- The Level 3 trigger system is a more elaborate system for event filtering. The Data Acquisition System reads out the detector information for events passing the Level 1 and Level 2 trigger and passes it to Level 3 trigger where a full 3-dimensional reconstruction of the CTC tracks is made. At Level 3, the p_T resolution is refined to $\delta p_T/p_T = 0.02p_T$. On the other hand, the CTC tracks are matched to the muon segments in the muon system using χ^2 . χ^2 is defined as:

$$\chi^2 = (\Delta I \ \Delta S) \begin{pmatrix} \sigma_I^2 & \delta \\ \delta & \sigma_S^2 \end{pmatrix}^{-1} \begin{pmatrix} \Delta I \\ \Delta S \end{pmatrix} \quad (5.3)$$

where ΔS is the difference between the slopes of the muon segment and the CTC track. ΔI is the difference of the intercepts of them. The parameter σ is the p_T -dependent resolution which includes energy loss and multiple scattering. The parameter δ is the correlation between ΔS and ΔI . The value of $\sqrt{\chi^2}$ follows a Gaussian distribution with $\sigma = 1$ and is independent of p_T . Using χ^2 matching is a more sophisticated method of matching muon segments with the CTC tracks.

Upon passing all three trigger levels, the data are written to mass storage (still magnetic tapes in Run IB) for offline reconstruction. Offline reconstruction uses a similar method as Level 3 but does a even more accurate calculation of all the information available. For example, in the offline reconstructions, raw information from the detector is converted into physical quantities, SVX tracking reconstruction is performed, and detector calibration and performance are taken into consideration. Many sets of offline reconstructions are performed for different physics interests. *BHMB.5B* (high-mass $\mu - \mu$ data) of stream B, which we use for our analysis, is one of them.

5.1.3 Offline Data Selection Criteria

The data sets produced in the offline reconstruction are kept in CDF data silos. We need to apply finer criteria on relevant data sets to obtain purer data for our analysis.

- “Good” runs only. A “good” run is a run in which all the subsystems work normally and there are $p\bar{p}$ collisions happening during the run. The goodness of a run is determined at the end of each run.
- Two muons, both with CMU-CMP muon segments, are required. If more than two muons exist, we choose the two muons with the highest p_T , because bottom muon candidates are expected to come from a relatively “harder” p_T spectrum.
- Both muons should have transverse momentum $p_T \geq 3.0$ GeV/c.
- In order to avoid picking up muons from the same B, we require the dimuon invariant mass to be $M \geq 5.0$ GeV.
- Quality cuts for SVX tracking:
 - Each muon is required to have at least 3 hits on SVX layers. Among them at least 2 good hits, i.e., hits not shared with another track and charge shared over 4 or less channels, are required.
 - χ^2 of the SVX tracking ≤ 6 .

- Matching χ^2 of muons in the CMU detector in the $r - \phi$ plane $\chi^2_{r-\phi}$ should be less than 9.0.
- Matching χ^2 of muons in the CMU detector χ^2_z should be less than 12.0.
- Matching χ^2 of muons of the CMP detector in the $r - \phi$ plane should be less than 9.0.

After all these criteria, we obtain 28323 events, among which 8697 events are LS (Like Sign) events and 19626 events are OS (Opposite Sign) events. Figure 5.1 shows the invariant mass spectrum of the LS and OS events.

5.1.4 Studies on Dimuon Data Offline Selection

Υ 's in the Dimuon Data

We can easily see the three Υ states in our LS dimuon mass spectrum. By fitting the dimuon mass spectrum with three Gaussians and one Exponential functions, we obtain the total number of Υ 's which is 2455 ± 49 . As a comparison to using 2-SVX-hit criteria, we performed the same fit to count the number of Υ 's in the dimuon data which are identical to the one in Figure 5.1 except that it has a 2-SVX-hit criteria. In Figure 5.2, we show the Υ fittings. The first figure shows the fitting for number of upsilons in the dimuon data with 2 SVX hits requirements. The second figure shows the ratio between the number of dimuon data with at least 2 SVX hits and the number of dimuon data with at least 3 SVX hits. We can see that we gain slightly in the upilon mass regions. Table 5.1 shows the comparison of number of Υ 's and background.

We have chosen at least 3 SVX hits criteria for our analysis.

Cosmic Rays in Dimuon Data

Figure 5.3 is the 2-dimensional Impact Parameter Distributions for dimuon. It shows that there exists a small cosmic ray component in the dimuon data. Cosmic rays appear only in the opposite sign data because the track of a cosmic particle entering

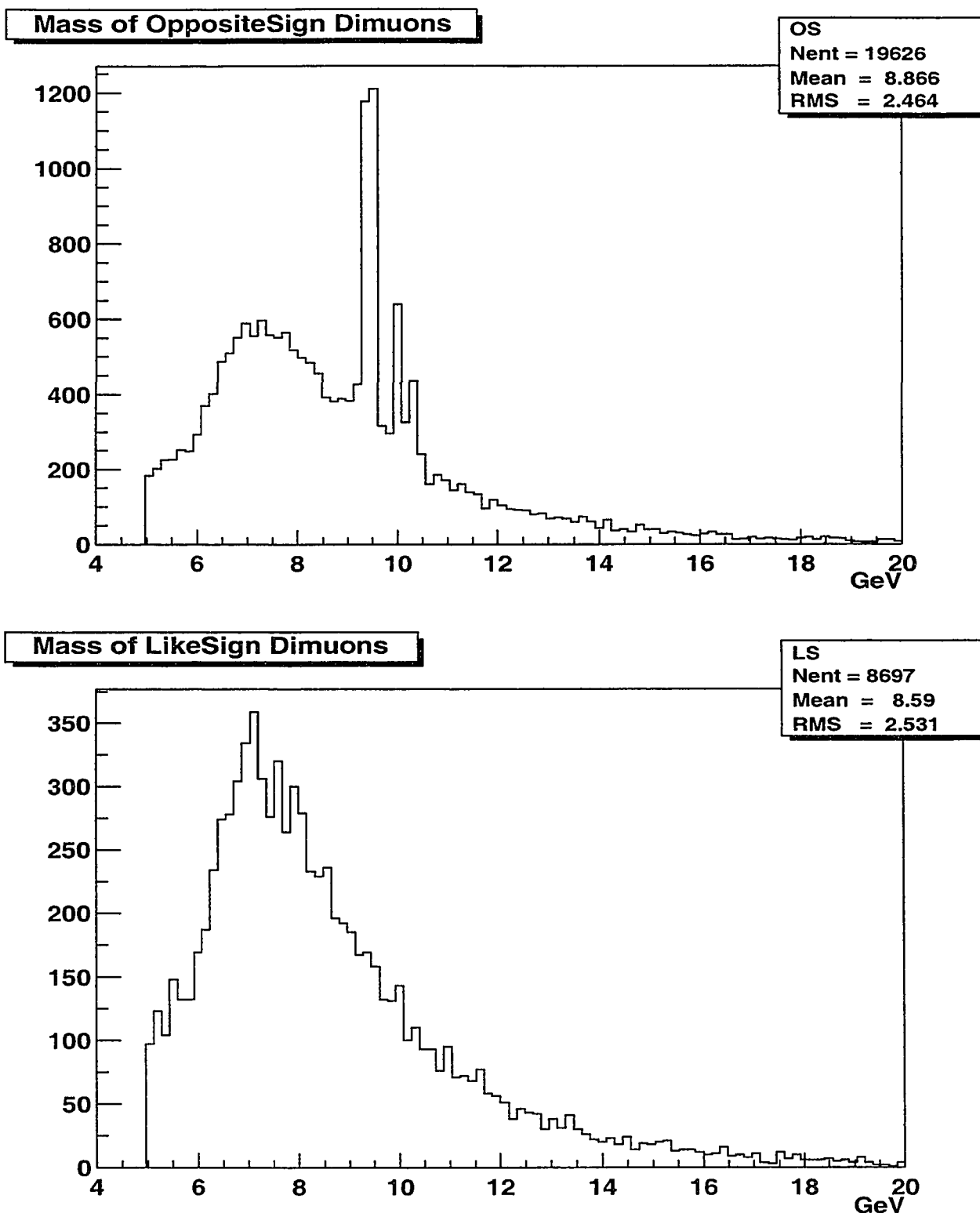
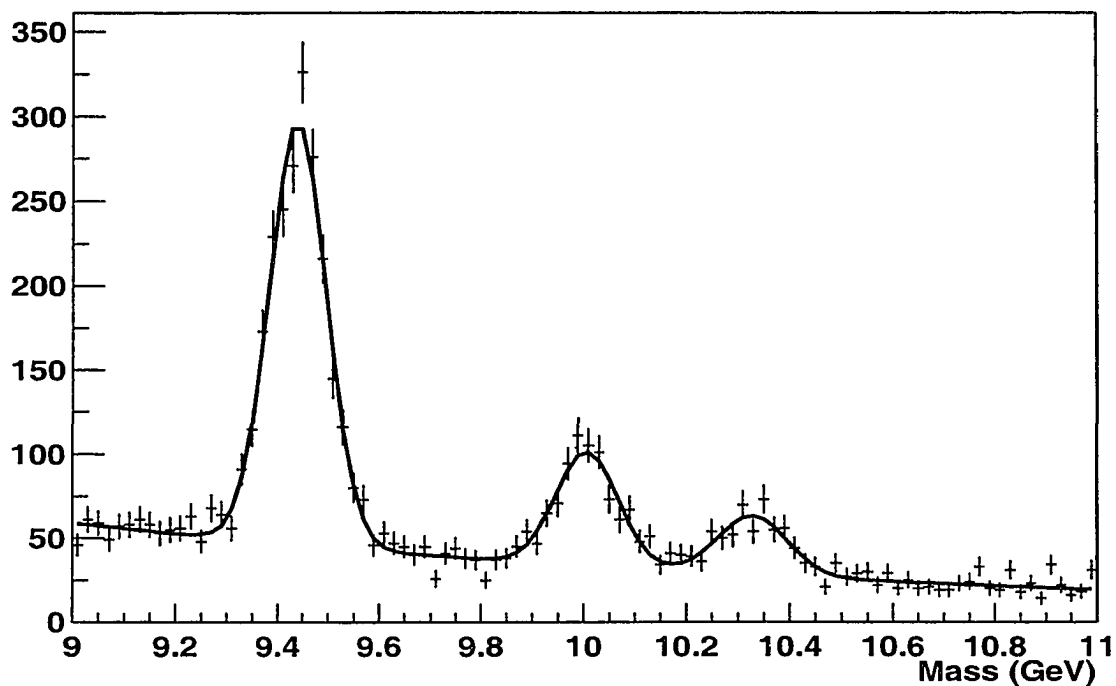


Figure 5.1: Mass Spectrum of OS and LS dimuons from CDF Run IB dimuon Data Set (after all selection criteria). We can see the existence of Υ 's in the OS dimuon signals.

Fit for Number of Upsilon's (2 SVX Hits)



(Events of 3 SVX hits)/(Events of 2 SVX hits)

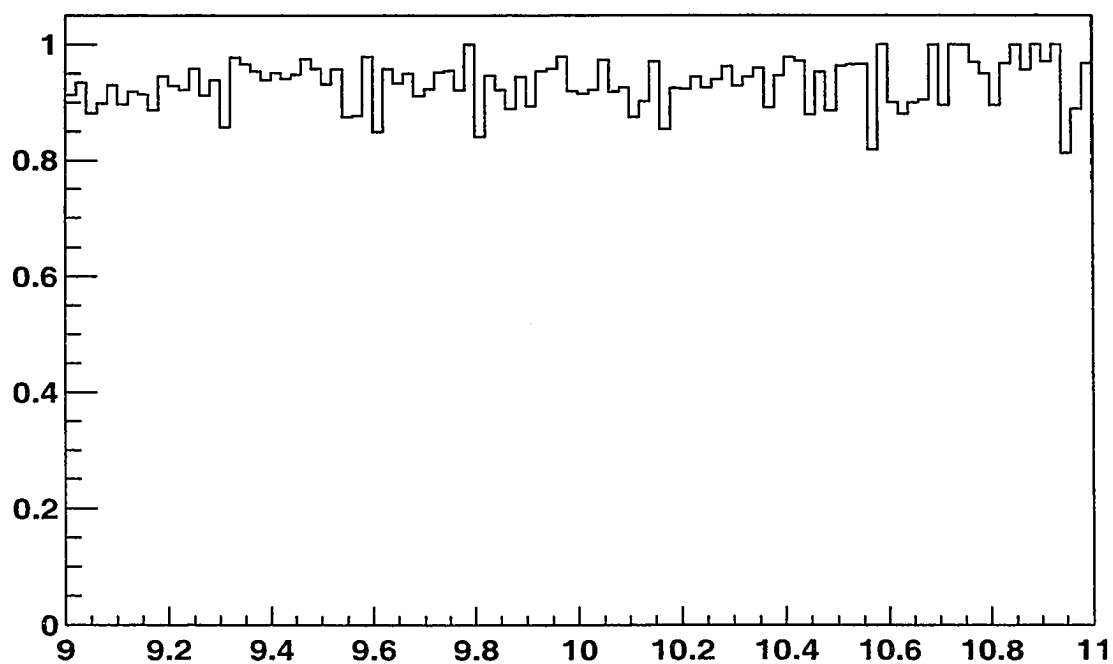


Figure 5.2: We compare the number of Υ 's under 2 or 3 SVX hits requirements. This figure shows that background signal reduces somewhat more than the muon signals after applying 3 SVX hits criteria.

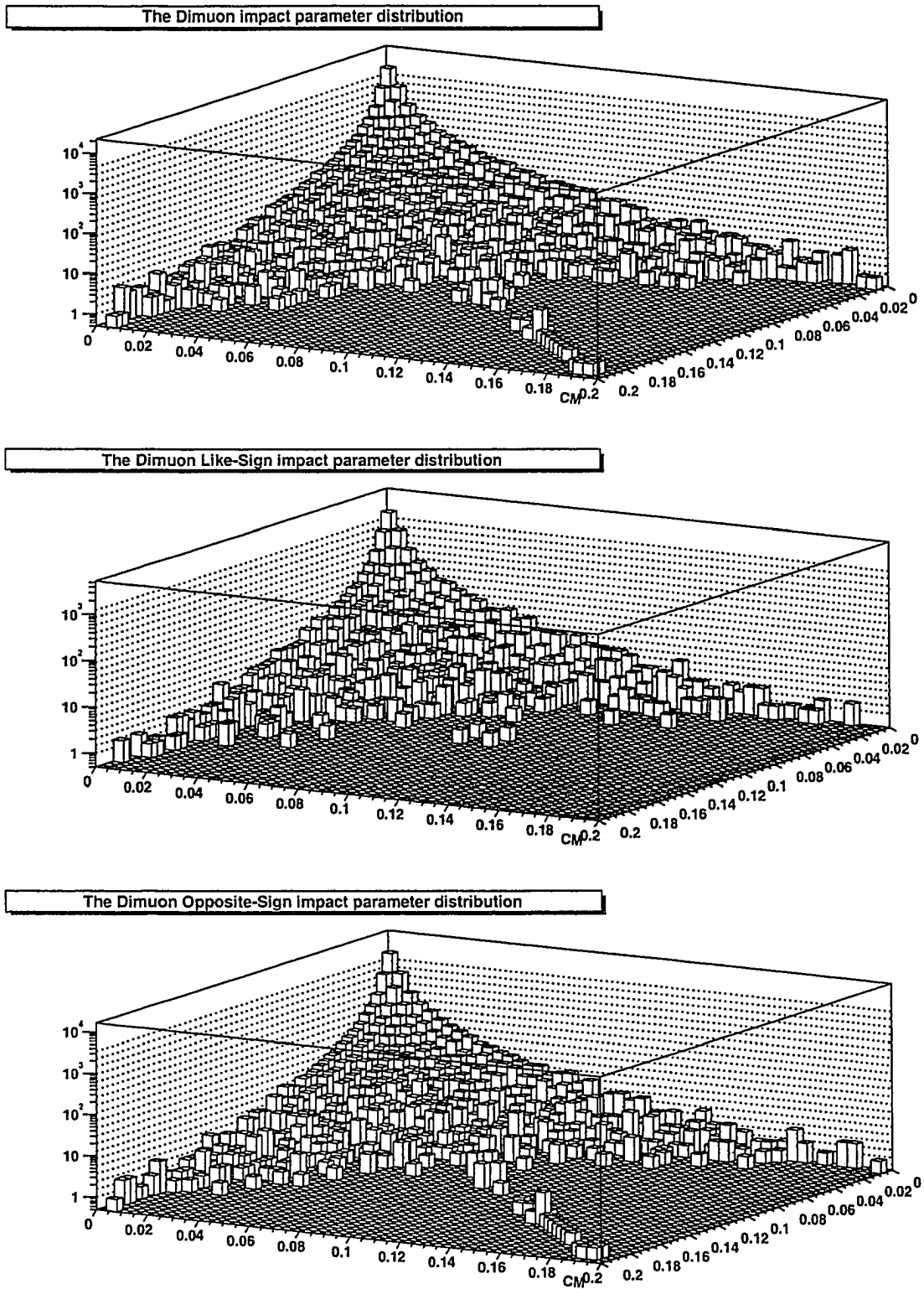


Figure 5.3: 2-dimensional Impact Parameter Distributions for dimuon data. Shown here are the distributions for Over All, Like-Sign (LS) and Opposite-Sign (OS) Dimuon Impact Parameter Distributions

	Υ 's	BACKGROUND
2 SVX hits	2582 ± 51	3549 ± 60
3 SVX hits	2456 ± 49	3276 ± 57
Reduced By	$(4.8 \pm .2)\%$	$(8.7 \pm .3)\%$

Table 5.1: By requiring 3 SVX hits, the background reduces more than the Υ signals do.

and then leaving the detector can be mistaken to be two tracks of opposite charge, both leaving the detector. Simple counting shows that the cosmic ray component takes up less than 0.5% of the total number of events and we choose to ignore them in later calculations.

Refinement of Impact Parameter

We use DO_SVX_PAD and VXPRIM in our software code. DO_SVX_PAD is a module that does SVX tracking reconstruction. VXPRIM is a vertex finder module. In order to avoid bias, during the reconstruction, we refine the coordinates of the primary vertex by removing all muon tracks and then recalculating the impact parameters with respect to the newly found vertex. Comparison of the second column and third column in Figure 5.4 shows that refining of the impact parameters removes the spike at the low values of impact-parameter.

By default, VXPRIM uses only tracks that have impact parameter significance less than 3.5σ from the current primary vertex. Some b-hadron decay tracks may be used in the primary vertex finding when the track multiplicity is low (not unexpected in $b\bar{b}$ events). This can cause a bias, pulling the calculated primary vertex closer to the b-hadron vertex than it actually is. Figure 5.4 shows that after explicitly requiring the “max_residual” to be 2.0 in VXPRIM, this bias is reduced. When we exclude muons, the bias disappears. [61]

We will do the same refinement for Impact Parameter templates from the Monte Carlo data and data from the prompt source as well.

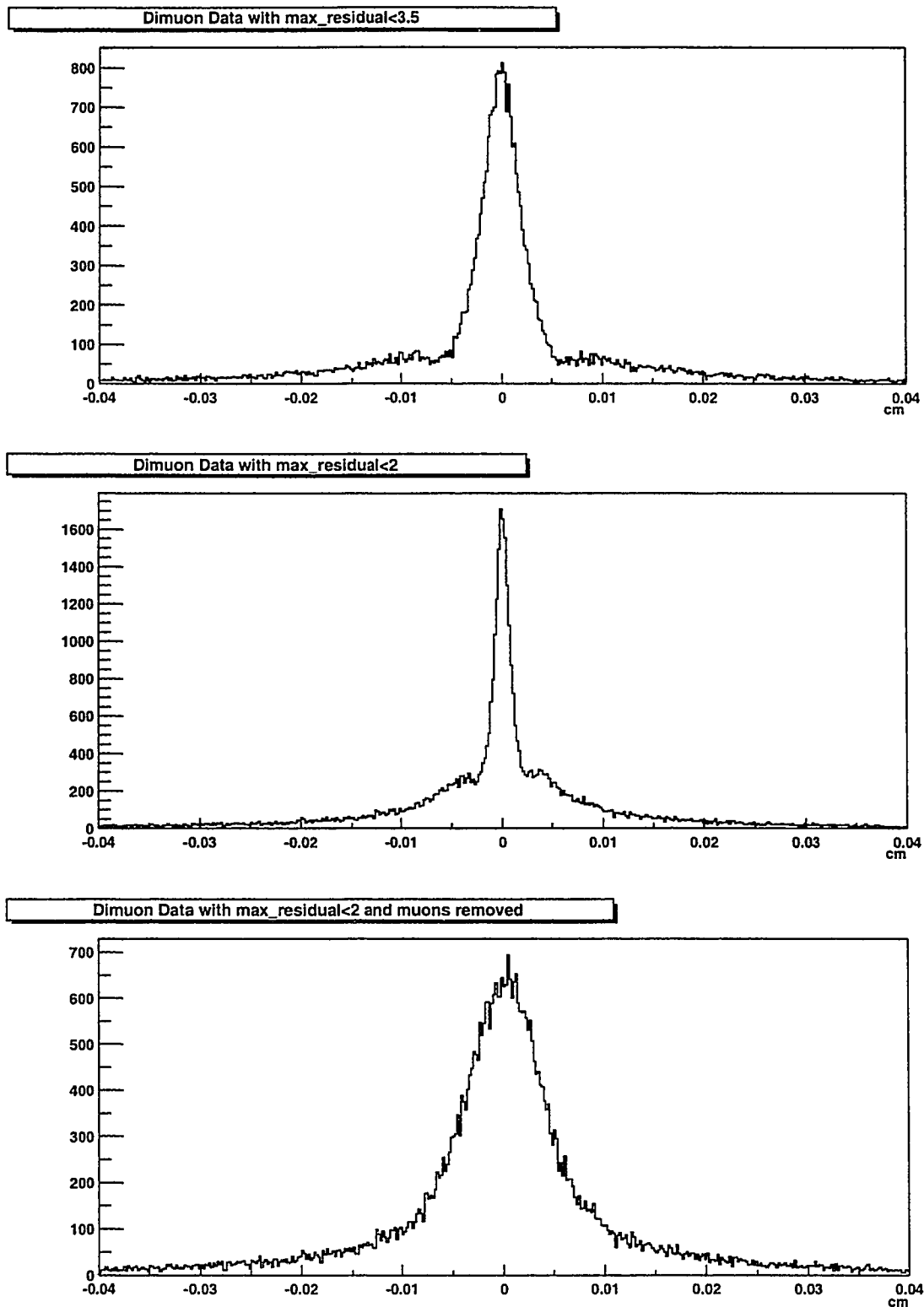


Figure 5.4: Dimuon Data Impact Parameter Distribution changes with reducing the max_residual and removing muons. We use the last one for the Impact Parameter Distribution in our analysis.

5.2 Monte Carlo Data

We need to do a few kinds of Monte Carlo simulations for different purposes in this analysis. First, to calculate the acceptance A in equation 4.1, we need to run a generator level Monte Carlo simulation of $p\bar{p}$ collisions and calculate the geometric and kinematic acceptance of the detector for dimuons. Since we only need the detector coverage and do not study the detector efficiency at this step, we do not need an explicit detector simulation. By leaving out the detector simulation, we can run the programs faster and have much more statistics for our calculation. Second, we need to run Monte Carlo simulations of $p\bar{p}$ collision that generates $b\bar{b}$ muons, $c\bar{c}$ muons and prompt tracks respectively and measure the impact parameters with a simulated detector. These impact parameters are used for generating IP templates to be used in the Impact Parameter Fitting method or as a comparison to IP templates obtained in other ways. Here we need to run the complete simulation of both the generator level and the detector level because the detector efficiency accounts for much of the shape of the IP distribution. Third, some small generator level Monte Carlo simulations are run to calculate the reweighting factors that recalibrates the main Monte Carlo's results. These are very simple Monte Carlo simulations with many restraints removed. They therefore can finish in a short time with high statistics for the sole purpose of recalibration. In this section we describe how these Monte Carlos are run and how we extract the results.

5.2.1 Software Packages and Parameters Selection

The software we use for the Monte Carlo Generation has three components which simulates different stages of the experiment. The program Pythia simulates the $p\bar{p}$ collisions at $\sqrt{S} = 1.8$ TeV and generates all the products of the collisions. The software QQ (also called CLEO_MC or CLEO) is a software that redecays some important particles such as B mesons and D mesons, etc. The reason we use QQ is that Pythia is not a specialized decay software and many important and detailed decays are not treated with sufficient sophistication and have to be redone by QQ. The QFL' program takes all the products from Pythia and QQ, simulates the CDF

detector and writes down the detected data in the same format as used for the real CDF data. Our reconstruction code can read the resultant data in the same way as reading the real dimuon data and extract necessary information. Not all of the Monte Carlo programs are necessarily used in each simulation. For instance, a generator level Monte Carlo simulation uses only Pythia and QQ.

Pythia

Pythia is a full-fledged Monte Carlo program intended for the study of hadronic processes emphasized in high- p_T physics in high-energy particle collisions. It includes hard scattering matrix elements, structure functions and initial and final state parton showers. It uses the ordinary Lund fragmentation model for fragmentation and does a detailed job in setting up the string configuration, especially for the low- p_T target remnants.

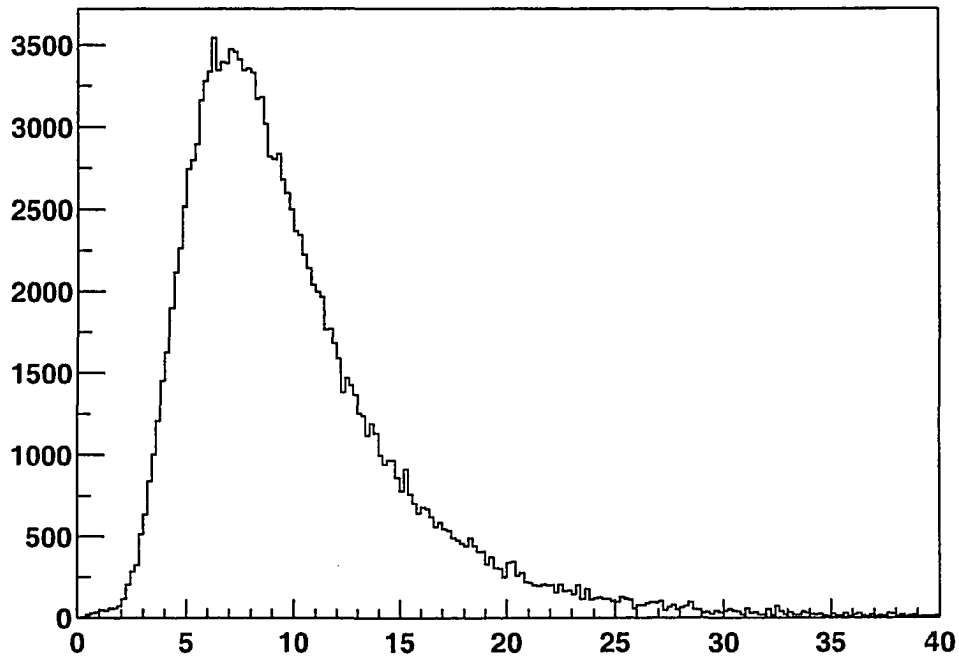
- Pythia for Acceptance Calculation

Pythia v5_7 is used to calculate the acceptances of dimuons in the CDF detector. The minimum quark p_T is chosen to be 4 GeV/c to accelerate computing while causing little bias (Figure 5.5). The pseudorapidity η of the b quark is limited between $(-1, 1)$ to include all the possible particles that could fall into the detector coverage while keeping the computation efficient.

- Pythia for IP Templates

We use Pythia v5_6 to generate muons from b quark pairs and c quark pairs separately. Minimum p_T for b quark is 0 GeV and minimum p_T for c quark is 4.0 GeV. The choice of quark p_T lower bound is set for technical reasons. The second plot in Figure 5.5 shows the p_T distribution of the c quarks that produces muons surviving all cuts when no explicit cuts on c quark p_T are put in the Monte Carlo. We find out that cutting away low p_T quarks ($p_T \leq 4$ GeV) will not affect our result significantly because this only cuts away less than 0.5% of the events. However this does accelerate our Monte-Carlo simulation to a large extent.

P_T Spectrum of b Quarks Producing Muons in IP Templates



P_T Spectrum of c Quarks Producing Muons in IP Templates

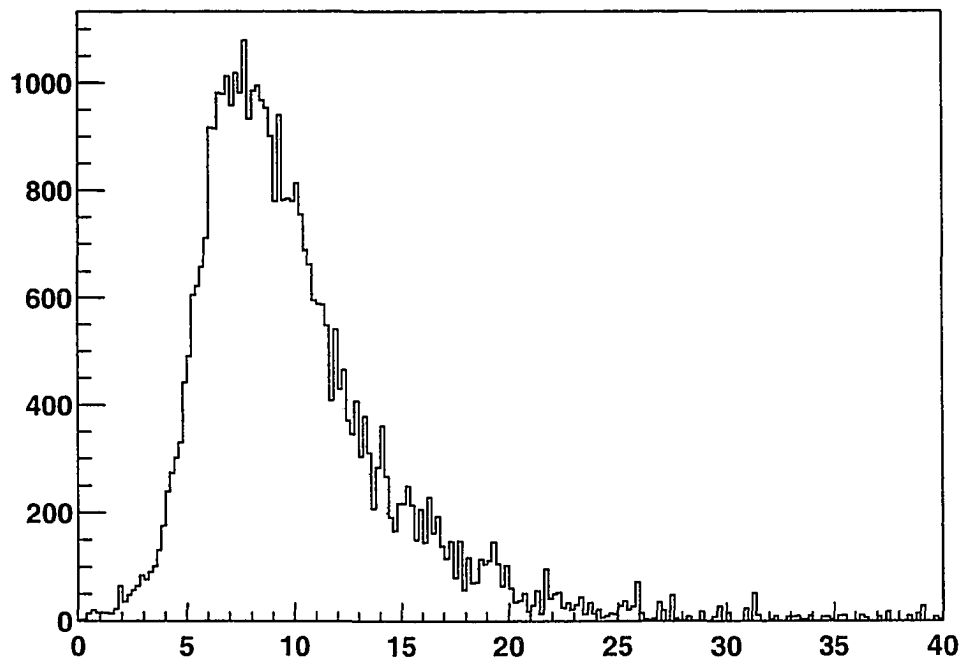


Figure 5.5: p_T spectrum of b , c quarks that produce muons in our IP templates. Since our templates requires $p_T(\mu) > 3$ GeV, most of the quarks have a relative high p_T .

At the Pythia level, we could apply no explicit rapidity criteria on quarks so that it can simulate the reality as close as possible. The pseudorapidity of quarks at this level can go as far as ± 10 . However, since almost 100% of the events that we are interested in are from quarks of rapidity $|y| < 1$, most of the time we use $|y| < 1$ constraints in the Monte Carlo simulations to accelerate the calculations.

Like what we have done with our dimuon data, we choose “max_residual” to be 2.0 in VXPRIM to reduce the bias. Figure 5.6 shows the difference of IP distribution shapes under different requirements.

- **Reweighting Particle Species Generated by Pythia** The world average values for B_u , B_d , B_s , and b – *baryon* production fractions are given in Reference [2]. The

f_{B_s}	$(9.4 \pm 2.2)\%$
$f_{b\text{-baryon}}$	$(10.1 \pm 1.8)\%$
f_{B_d}, f_{B^+}	$(40.3 \pm 1.2)\%$

Table 5.2: The world average fractions of b-hadrons determined from Reference [2] as direct measurements.

relative production rates coming from Pythia do not completely match those values. We need to reweight the b-hadron species produced by Pythia in order to agree with Reference [2]. Also, we need to reweight the c-hadrons accordingly. By running a generator level Pythia and QQ Monte Carlo job, we are able to determine those reweighting factors. We can use these reweighting factors to recalculate the central values of all results based on Pythia. [2] also gave the uncertainties of these fractions. These uncertainties can propagate to all the calculations based on Pythia. We retoss the species ratios away from their central value with Gaussian distributions multiple times and use the standard deviation of the outcomes as the systematic uncertainties.

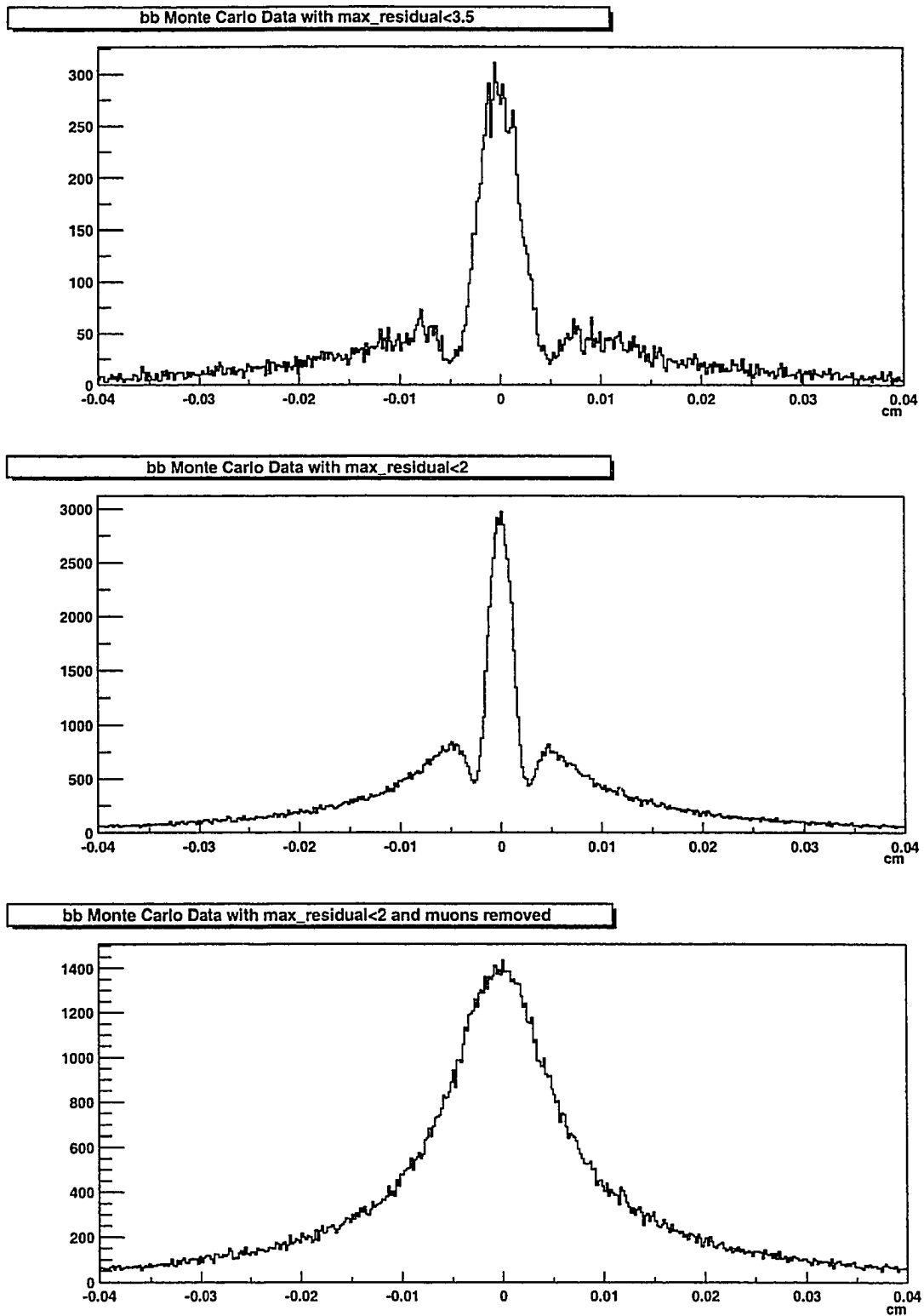


Figure 5.6: Monte Carlo $b\bar{b}$ Data Impact Parameter Distribution changes with reducing the max_residual and removing muons. We use the last one for the impact parameter distribution in our analysis.

QQ Monte Carlo Package (CLEO)

We use QQ version 9.1 in our analysis. To generate muons from b-hadron decays, we turn on all the b decays. To generate muons from c-hadron decays, we turned on the `prompt_charm_decay`. In both cases we turn on “lowest_only”. We do not allow $B\bar{B}$ mixing in QQ.

In order to gain more statistics, we let QQ do a fixed number of retossing of the Pythia events (100 times). Every Pythia event is treated equally and therefore no bias is introduced by this retossing.

Right-Sign and Wrong-Sign Cascade b Semileptonic Decay Rate

Reference [2] gives the world average information for semileptonic Branching Ratio for b-hadrons.

Direct b-hadron sl. BR	$BR(b \rightarrow l^- \bar{\nu}_l X)$	0.1058 ± 0.0018
Cascade b sl. decay (r.s.)	$BR(b \rightarrow \bar{c} \rightarrow l^- \bar{\nu}_l X)$	0.0162 ± 0.0044
Cascade b sl. decay (w.s.)	$BR(b \rightarrow c \rightarrow l^+ \nu_l X)$	0.0807 ± 0.0025

Table 5.3: World average cascade b semileptonic decay rates from Reference [2]

The relative B.R. obtained with Pythia and QQ do not completely match Table 5.3. Therefore we need to reweight the products of the cascade decays (compared to the direct decays). The reweighting factors are again found by running a Pythia and QQ job requiring at least one muon to be produced. Any subsequent result depending on Pythia and QQ are recalculated using the reweighting factors. The systematic uncertainty caused by the uncertainties in the r.s. and w.s. are calculated by retossing r.s. and w.s. away from the central value in a Gaussian distribution and calculating the standard deviation of the outcomes from such retossing.

QFL'

We use QFL' to perform detector simulation. In QFL', beam spot is set at $(X, Y) = (0, 0)$ and beam slope is set $(0, 0)$ and beam sigmas are set to $\sigma_X = \sigma_Y = .0025cm$.

	B^0, B^0	B^\pm	B_s	Λ_b
Factors	1	0.995	1.161	1.293
	D^\pm	D^0, D^0	D_s	Λ_c
r.s. Factors	0.929	0.931	0.944	1.023
w.s. Factors	0.929	0.930	1.066	1.069

Table 5.4: The central values of combined reweighting factors for Pythia and QQ outputs.

Data banks written to the harddrives are in the same format as those in the Run IB silo and therefore can be retrieved with the same reconstruction code.

5.2.2 The Selection Criteria for the Monte-Carlo Data

Since we save the Monte-Carlo data in the same format, we can use similar reconstruction code to strip our data. Similar selection criteria are applied in the reconstruction.

- At least one muon with CMU-CMP muon segment is required. If more than one muon is found, the two muons with highest p_T are put into the template as if they were generated separately. Events with more than one muon count for less than 0.1% of the total number of Monte-Carlo events.
- Muon transverse momentum $p_T \geq 3.0$ GeV.
- Quality criteria for SVX tracking:
 - Each muon is required to have at least 3 hits on SVX layers. Among them at least 2 Good hits, i.e., hits not shared with another track and charge shared over 4 or less channels, are required.
 - χ^2 of the SVX tracking/degree of freedom ≤ 6 .
- Event vertices have $|z| \leq 30.0$ cm.
- Matching χ^2 of muons in the CMU detector in the $r - \phi$ plane $\chi^2_{r-\phi}$ should be less than 9.0.

- Matching χ^2 of muons in the CMU detector χ_z^2 should be less than 12.0.
- Matching χ^2 of muons of the CMP detector in the $r - \phi$ plane should be less than 9.0.

5.2.3 Dimuon Trigger (DIMUTG)

DIMUTG is a routine written by Steve Pappas [62] which is used to correct the data for the dimuon trigger efficiency. It checks geometric and kinematic properties of individual muon pairs for passing the trigger requirements. Muons falling into regions of phase space for which the trigger is not designed to be efficient are removed to avoid strong dependencies on luminosity and event structure. Events in these regions could pass the physical trigger due to background effects such as matching incorrect CFT tracks to a hit muon chamber. Muons that pass the physical trigger may be removed by the DIMUTG code to avoid these effects in the efficiencies. Losses above the trigger thresholds are low.

DIMUTG is used in our cross section measurements because trigger efficiencies are an important factor in the calculations. We do not use DIMUTG in our $\bar{\chi}$ measurement to gain more statistics. (We have checked $\bar{\chi}$ is not sensitive to DIMUTG.)

5.3 Track Data from Prompt Source

As discussed in the Method Chapter, we need an impact parameter template that has the shape of prompt source tracks in our fitting. We use tracks from photon jet events of Run IB data with $E_t \geq 23$ GeV (isolated) for this purpose. The data is extracted from data set GHIB-5P. The selection criteria for prompt tracks are:

- A vertex with class > 10 is required. The highest class vertex is used. The class of the a vertex reflexes the quality of the vertex reconstruction. The higher quality a vertex reconstruction is, the higher class it has.
- “Good” runs only.
- All candidate tracks of the events are used.

- Candidate tracks are required to have $p_T \geq 3.0$ GeV.
- Candidate tracks are required to be CMP fiducial. (We use CMUSWM to determine the fiduciality.)
- Z component of the candidate tracks are required to be within 5 cm of the vertex from which the impact parameter is measured. This is because if a track has a z component that is far away from a vertex, it is not likely the track is an offspring of that vertex.
- Quality cuts on SVX tracking:
 - Each track should have at least 3 hits on SVX layers. Among them at least 2 good hits, i.e., hits not shared with another track and charge shared over 4 or less channels, are required.
 - χ^2 of the SVX tracking/degree of freedom ≤ 6 .
- Event vertices have $|z| \leq 30.0$ cm.

Figure 5.7 validates the 5 cm Z cut and CMP fiducial cut. Z_0 in the Figure is defined as the z component of the track. The first figure is the distribution of the z component of the primary vertex. The second figure is the distribution of the z component of the tracks. The third one shows after the 5 cm requirement, the z component of the tracks shrink to similar regions as the primary vertex. The last figure shows the difference between the IP distributions before and after the $Z_0 < 5$ cm and CMP fiducial requirements. We can see that these two requirements are helpful for removing some badly measured tracks.

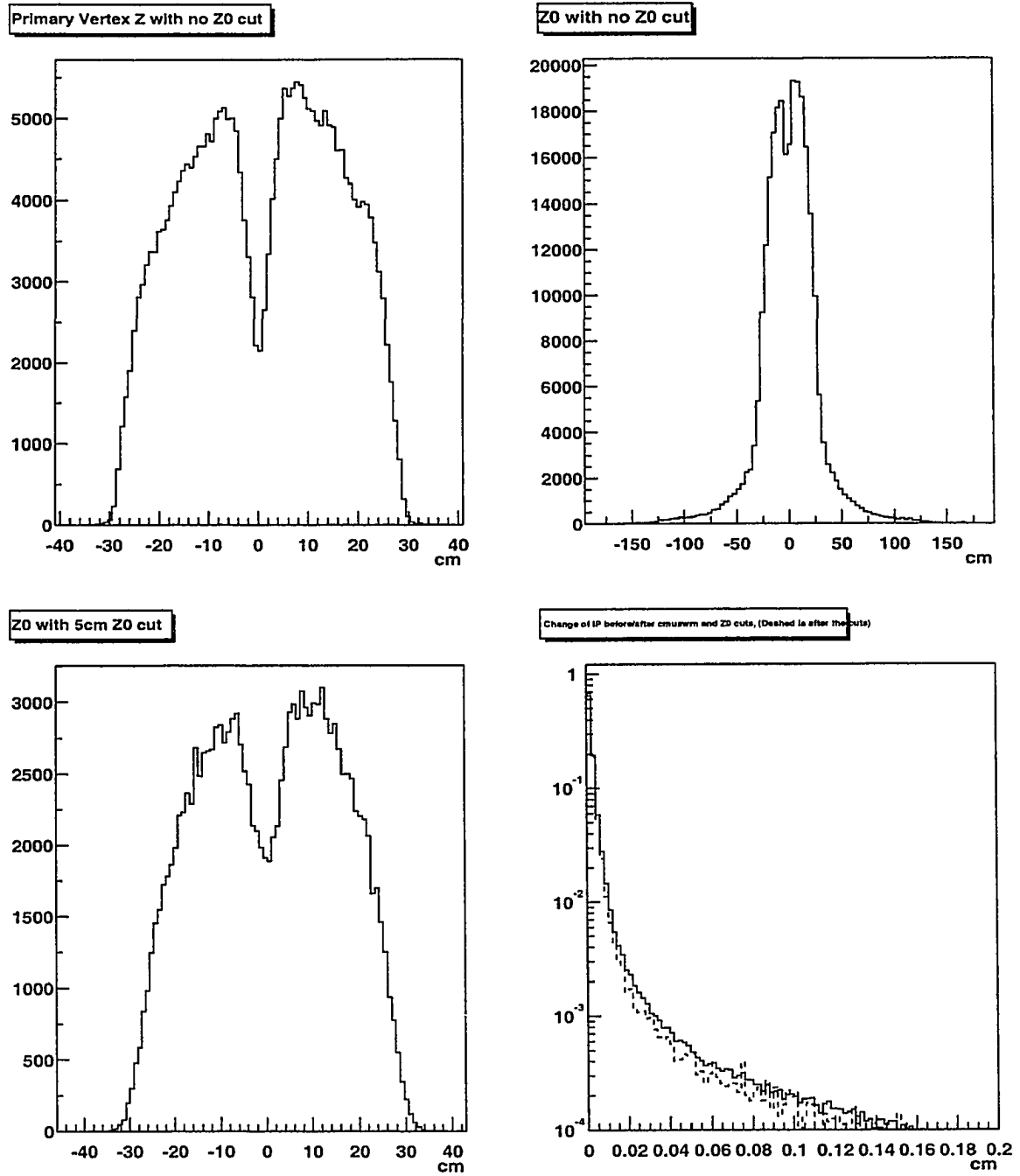


Figure 5.7: Validation of some cuts on prompt data (cm)

Chapter 6

The Measurement of $b\bar{b}$ Production Cross Section in $p\bar{p}$ Collision at $\sqrt{S} = 1.8$ TeV

6.1 Introduction

In Chapter 4, we discussed briefly the method for measuring the $b\bar{b}$ cross section. Equation 4.1 gives the formula determining the total $b\bar{b}$ cross section. Given the amount of statistics we have, we are able to divide the dimuon events into 3 distinct kinematic data subsets and calculate the cross sections in those kinematic bins. The three data sets we have chosen are defined by the transverse momenta, p_T , of the muons as given in Table 6.1:

Bins	1	2	3
$p_T(\mu_1)$	> 3 GeV/c	> 3 GeV/c	> 3 GeV/c
$p_T(\mu_2)$	$\in (3, 5)$ GeV/c	$\in (5, 7)$ GeV/c	$\in (7, \infty)$ GeV/c

Table 6.1: Three bins chosen for $b\bar{b}$ cross section measurements. The order of the muons are determined randomly without preference.

The order for choosing μ_1 and μ_2 in each dimuon pair is randomly chosen so that

there will be no systematic uncertainties caused by ordering the muons according to their p_T 's or other characteristics. Besides the criteria for the dimuon data mentioned in Section 5.1.3, we also apply DIMUTG to the data set because triggering efficiency is accounted for in our CDF efficiency measurement (Section 6.3).

Figure 6.1 shows the ancestor quark $p_T(b)$ spectra of the second muon in these three data subsets. The data used in the figures are obtained by running a generator level Monte Carlo simulation of Pythia and QQ with no quark p_T criteria applied. A generator level Monte Carlo simulation is a process that simulates $p\bar{p}$ collisions and decays of the particles produced in the collisions, but it does not simulate a particle detector in the process. Since we produce Figure 6.1 only to show the relationship between the muon p_T and quark p_T , we do not need a full simulation. Also by using a simple generator level simulation, we can accelerate our computation to a large extent and obtain richer statistical data.

We can see in Figure 6.1 that the muons in different p_T bins have different quark p_T spectra. Muons with higher p_T tend to originate from ancestor quarks with higher p_T because in the process of $b \rightarrow B \rightarrow \mu$, the daughter particles are boosted in the same direction as the parent particles. We define $p_T(b)_{min}$ to be the quark momentum such that 90% of the muons in that specific $p_T(\mu)$ bin originate from a b quark with a $p_T(b)$ greater than $p_T(b)_{min}$. Table 6.2 shows the $p_T(b)_{min}$ calculated from the Monte Carlo results. As we can see $p_T(b)_{min}$ increases as $p_T(\mu)$ increases.

Bins	1	2	3
$p_T(\mu_2)$	$\in (3, 5)$ GeV/c	$\in (5, 7)$ GeV/c	$\in (7, \infty)$ GeV/c
$p_T(b_2)_{min}$	6.5 GeV/c	8.75 GeV/c	12.25 GeV/c

Table 6.2: $p_T(b)_{min}$ for the three $p_T(\mu)$ bins.

Since $p_T(\mu_1) > 3$ GeV/c is the same criteria for all three bins, we always have $p_T(b_1)_{min} = 6.5$ GeV/c.

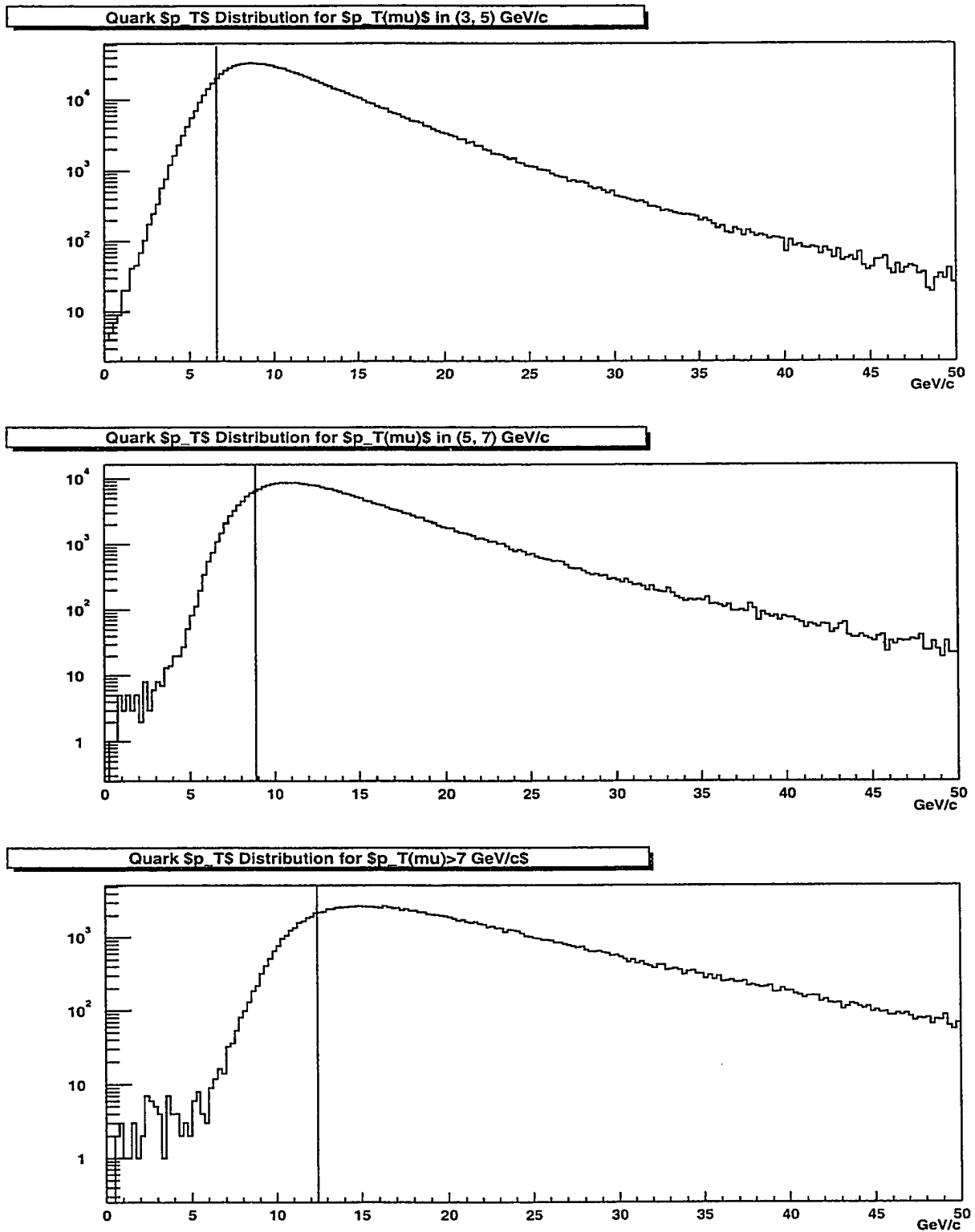


Figure 6.1: Quark p_T distribution given different muon p_T . The dashed line in the figure indicates the minimum quark momentum $p_{T(b)_{min}}$. 90% of the muons in that specific $p_{T(\mu)}$ bin originate from a b quark with a $p_T(b)$ greater than $p_{T(b)_{min}}$.

6.2 The Acceptance

In our analysis, the dimuon acceptance of the CDF detector is defined as:

$$A = \frac{N_1}{N_2} \quad (6.1)$$

Here N_1 is the number of events that pass the following requirements:

- At least 2 muons are produced in each event; muons from both direct and cascade decays are counted.
- The muons' p_T are in the muon p_T bins specified above.
- The dimuon invariant mass is required to be $\geq 5 \text{ GeV}/c^2$.
- Both muons are required to be CMU and CMP fiducial. We use a module called CMUSWM in the CDF library to determine the fiduciality of the muons. The CMUSWM takes the momenta of the tracks as inputs and determines whether the tracks fall into the geometric coverage of the CMU and CMP. The CMUSWM is employed with energy loss and multiple scattering turned off.

Here N_2 requires:

- A $b\bar{b}$ pair is produced and each of them decays into a muon.
- $p_T(b_1) \geq p_{T(b_1)_{min}}$ and $p_T(b_2) \geq p_{T(b_2)_{min}}$
- $|y(b_1)| \leq 1$ and $|y(b_2)| \leq 1$ where y is the rapidity of the particle.
- Both muons are products of direct semileptonic decay of b-hadrons. This is required because according to Equation 4.1, $Br(b \rightarrow \mu)^2$ used in the cross section calculation is taken to be that for direct semileptonic decays of b-hadrons.

The acceptance for each p_T bin is obtained through a generator level Monte Carlo simulation (Pythia and QQ). Since the geometric and kinematic acceptance of the tracks does not rely on the detector efficiency or its material components, we do not need to simulate a detector in the process. We calculate the acceptance by counting the N_1 and N_2 in the simulation.

6.2.1 Monte Carlo Weights for the Acceptance

Pythia, as a package that simulates the $p\bar{p}$ collisions, uses default relative B species fractions that are different from the world average numbers shown in Table 5.2. QQ, as a decay simulation package, uses a set of B semileptonic branching ratios different from the world average values shown in Table 5.3. In order for the Monte Carlo simulation results to correctly reflect our best knowledge of the B species fractions and B semileptonic branching ratios, we need to reweight the hadrons generated in most of the simulations in our analysis.

The reweighting factors are again found by running a few generator level Pythia and QQ simulations. The factors for the B hadron species reweighting are obtained by running a simple Pythia Monte Carlo simulation with no constraints and count the number of B 's generated in the simulation. By comparing these number to the world averages in Table 5.2, we can calculate the numbers in Table 6.3.

The D hadrons' reweighting are due to both the B species reweighting and the semileptonic branching ratio reweighting. By counting the numbers of D hadrons with different B ancestries in the products of the Pythia simulation with no constraints, we can change the D 's fractions according to the B species reweighting. Also using the same Monte Carlo simulation, we can adjust the D 's fractions according to the branching ratios in Table 5.3.

D hadron reweightings are carried out for two different cases: Right-Sign (RS) and Wrong-Sign (WS). RS D hadrons are D hadrons that decay into leptons carrying the same electric charge as the ancestor b quarks. WS D hadrons are D hadrons that decay into leptons carrying opposite electric charge to the ancestor b quarks. We need to treat these two cases separately because the reweightings are different for RS D hadrons' ratio and WS D hadrons' ratio and thereby can affect our subsequent calculations such as wrong-sign sequential (r_{ws}) estimations mentioned in Chapter 4.

All our subsequent analysis depending on Pythia and QQ simulations are recalculated using these reweighting factors. The central values for the combined reweighting factors accounting for the effects due to the both the species fractions and branching ratios are listed in Tables 6.3 and 6.4. The systematic uncertainties caused by the uncertainties in the reweighting factors are calculated by retossing the reweighting

factors away from their central value in a Gaussian distribution and measuring the standard deviation of the outcomes from such retossing.

	B^0	B^+	B_s	Λ_b
Factors	1	1.001	1.120	1.273

Table 6.3: The central values of the combined reweighting factors for B hadrons from Pythia and QQ outputs.

	D^+	D^0	D_s	Λ_c
RS Factors	0.970	0.971	0.985	1.099
WS Factors	0.975	0.976	1.082	1.111

Table 6.4: The central values of the combined reweighting factors for D hadrons from Pythia and QQ outputs.

6.2.2 Rapidity Constraints in Our Monte Carlo Simulations

In our Monte Carlo simulations, the rapidities for the generated quarks are restricted such that $|y| < 1$. This restriction is valid as demonstrated in Figure 6.2. The first figure shows the rapidity distribution of the b quarks in a generator level Monte Carlo simulation with Pythia and QQ where rapidities are constrained in $|y| < 2$. Each b quark here generates at least one muon. After applying $p_T(\mu) > 3$ and CMU-CMP fiduciality criteria on the same data set, almost all the b quarks are with rapidity $|y| < 1$. Since in our analysis $p_T(\mu) > 3$ and CMU-CMP fiduciality are a basic requirement on the dimuon data and Monte Carlo templates, the restriction of $|y| < 1$ is applied on most of the Monte Carlo simulations except when explicitly mentioned. This restriction accelerates the computing and therefore provides richer statistics for our analysis.

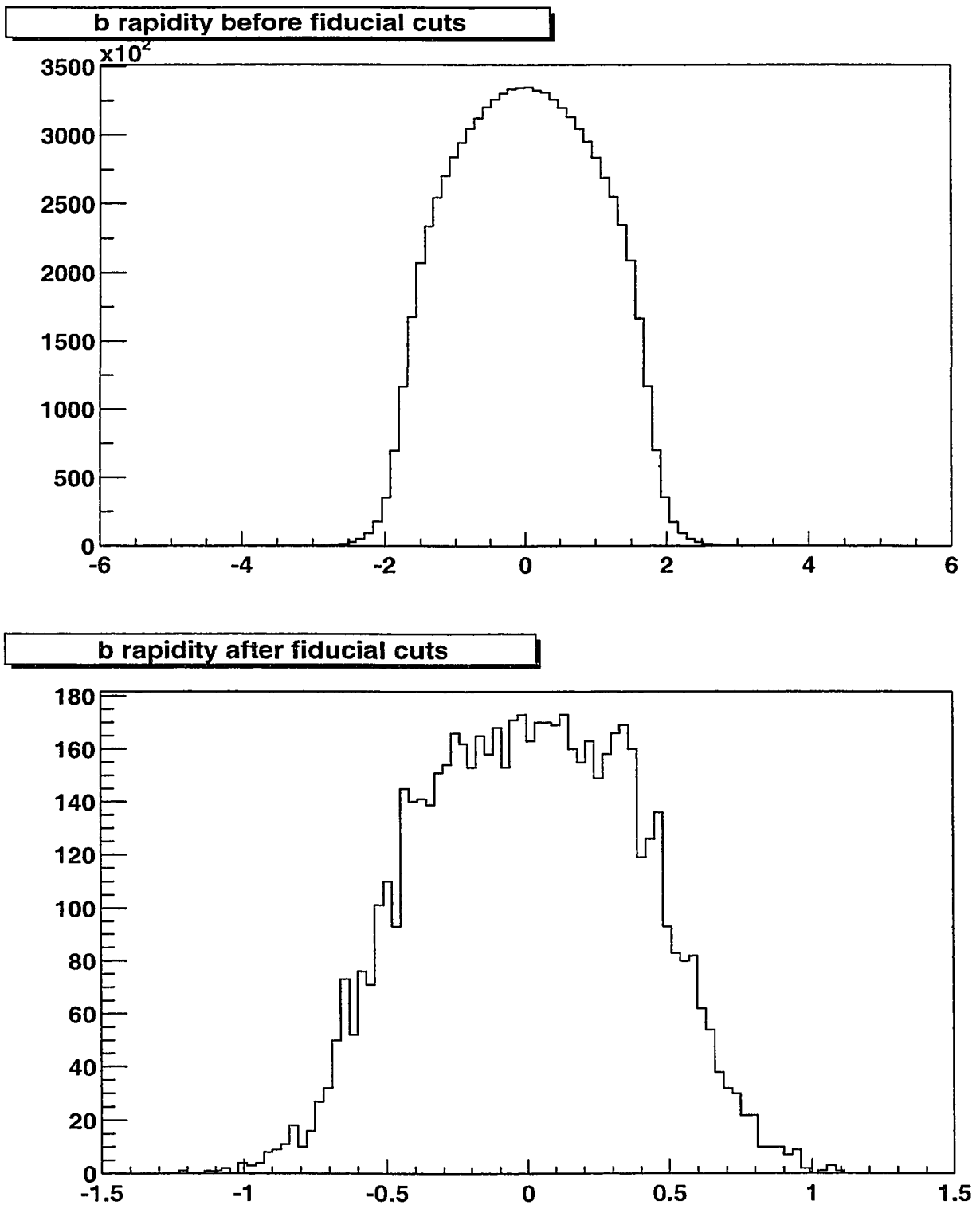


Figure 6.2: Quark rapidity distributions before (above) after (below) the CMU-P Fiducial requirements and $3 \text{ GeV}/c \text{ } p_T$ requirement. The rapidity distribution shrinks to $(-1, 1)$ after the requirements.

6.2.3 The Results for the Detector Acceptances

With the reweighting tool available, we are able to calculate the acceptances by dividing the reweighted N_1 by the reweighted N_2 . We can estimate the acceptance uncertainties based on the following factors:

- The Monte Carlo statistics: We can only simulate limited number of collisions.
- The uncertainties of the world-average B species fractions in Table 5.2.
- The uncertainties of the world-average B branching ratios shown in Table 5.3.

The results and uncertainties for the acceptances in the three $p_T(\mu)$ bins are given in Table 6.5.

$p_T(\mu_1)$	$\geq 3 \text{ GeV/c}$	$\geq 3 \text{ GeV/c}$	$\geq 3 \text{ GeV/c}$
$p_T(\mu_2)$	$3 - 5 \text{ GeV/c}$	$5 - 7 \text{ GeV/c}$	$\geq 7 \text{ GeV/c}$
Acceptance	0.0155	0.0078	0.0113
Uncertainty	0.0008	0.0005	0.0008
Monte Carlo Statistical Uncertainty	0.0007	0.0003	0.0005
Uncertainty from b-hadron Species Fraction	0.0003	0.0003	0.0006
Uncertainty from B branching ratios	0.0002	0.0001	0.0001

Table 6.5: Acceptances and uncertainties in different muon p_T bins determined from Pythia + QQ generator level dimuon Monte Carlo

6.2.4 A Comparison to BGenerator

As a cross check we also used BGenerator and obtained the results given in Table 6.6. BGenerator [63] is another Monte Carlo simulation software program used widely in the CDF Run I experiment. Compared to the general purpose simulation package Pythia, BGenerator is a special purpose simulation package that only generates b quarks according to the inclusive transverse momentum spectrum from the NDE [17] or MNR [8] calculations.

$p_T(\mu_1)$	$\geq 3 \text{ GeV/c}$	$\geq 3 \text{ GeV/c}$	$\geq 3 \text{ GeV/c}$
$p_T(\mu_2)$	$3 - 5 \text{ GeV/c}$	$5 - 7 \text{ GeV/c}$	$\geq 7 \text{ GeV/c}$
Acceptance	0.0150	0.0075	0.0128
Uncertainty	0.0008	0.0006	0.0005
Monte Carlo Statistical Uncertainty	0.0005	0.0003	0.0005
Uncertainty from b-hadron Species Fraction	0.0006	0.0005	0.0001
Uncertainty from Cascades	0.0002	0.0001	0.0002

Table 6.6: Acceptances and assigned uncertainties in different p_T bins as determined from BGenerator + QQ generator level dimuon Monte Carlo.

The BGenerator products undergo the same QQ processes as Pythia's. We also count the N_1 and N_2 in the same way as in our calculations using Pythia. The acceptances and their uncertainties are calculated in identical ways as well.

Table 6.5 and 6.6 show that Pythia and BGenerator give similar results for the CDF detector acceptances for all three kinematic bins of muons.

Since BGenerator generates b quarks only, and does not take into account other interactions in $p\bar{p}$ collisions like Pythia does, BGenerator is a much faster algorithm than Pythia. On the other hand, Pythia treats the $p\bar{p}$ collisions more sophisticatedly and generates events closer to the reality. Therefore, we prefer to use the Pythia results for our final results.

6.3 Detector Efficiency ϵ_{CDF}

The CDF detector efficiency is defined as the efficiency of observing the muons that are accepted into the geometric and kinematic criteria of the detector. Different subsystems of the detector have different efficiencies for muons. We write the total detector efficiency for dimuons ϵ_{CDF} as a product of a series of subsystem efficiencies as shown in Equation 6.2:

$$\epsilon_{CDF} = \epsilon_{svx} * \epsilon_{trig} * \epsilon_{norm} * \epsilon_{ctc}^2 * \epsilon_{cmu}^2 * \epsilon_{link}^2 * \epsilon_{match}^2 * \epsilon_{cmp}^2 * \epsilon_{L3} \quad (6.2)$$

Here, ϵ_{svx} is the SVX efficiency, ϵ_{trig} is the trigger efficiency, ϵ_{norm} is the normalization correction efficiency, ϵ_{ctc} is the CTC efficiency, ϵ_{cmu} is the CMU efficiency, ϵ_{link} and ϵ_{match} are the muon linking and matching efficiencies, ϵ_{cmp} is the CMP efficiency and ϵ_{L3} is the Level 3 trigger efficiency.

We will need to calculate each one of these subsystem efficiencies to get the total detector efficiency. According to References [1] and [64], as long as $p_T(\mu)$ is greater than 3 GeV/c, the subsystem efficiencies have little dependency on $p_T(\mu)$. Therefore we use the same efficiencies for all three muon transverse momentum bins. Most of the efficiencies in Equation 6.2 are independent from each other and their orders can be permuted. However, some of them cannot be permuted. For example, the order of the SVX efficiency, ϵ_{svx} , and the Level 3 efficiency, ϵ_{L3} should not be exchanged because Level 3 trigger effectively requires a primary vertex criteria $|z| < 35cm$ while the SVX efficiency relies on the z coverage of the SVX. Applying Level 3 trigger before or after the SVX requirements will mean different conditional probability for a muon to pass the SVX requirements, i.e., the SVX efficiency will be different in the two situations. We therefore should be very careful and emulate similar geometric and kinematic situations when calculating these efficiencies individually.

6.3.1 Using Upsilons in the Efficiency Calculations

Some of the subsystem efficiencies are calculated using the upsilons signals in our dimuon data. The reason for choosing upsilons is that dimuons from upsilons decays have a unique mass spectrum (three peaks in the $(1S)$ $(2S)$ and $(3S)$ states of upsilons) and are easily identified and separated from the background.

The other reason for using upsilons is that these dimuons share similar kinematic properties with dimuons from $B\bar{B}$ hadrons. Figure 6.3 shows the distributions of the opening angle between the two tracks in the transverse plane in different data sets. The opening angle between the two muons is concentrated in the back-to-back region. For the upsilons data, We simply take the mass region between 9.3 GeV/c² and 10.5 GeV/c² in the dimuon data for the upsilons without background subtraction because this region is dominated by the upsilons. The similarity of kinematics between the

upsilons in the dimuon data and the rest of the dimuon data shows that we can use the upsilons as the sample for determining many subsystem efficiencies for the dimuon data with little bias.

6.3.2 ϵ_{SVX}

We study the upsilons in the dimuon data before and after these SVX requirements:

- Each muon should have at least 3 hits on the SVX layers. Among them at least 2 good hits, i.e., hits not shared with another track and charge shared over 4 or less channels, are required.
- χ^2 of the SVX tracking/degree of freedom are ≤ 6 .

We define ϵ_{SVX} as a efficiency with the Level 3 trigger implicitly required.

In Figure 6.4, the first figure shows the dimuon mass distribution in the upsilons region with all other requirements except the SVX requirement. The second figure is the dimuon mass spectrum with all requirements. We fit the mass spectrum with three Gaussians (upsilons) and one exponential (background) and count the number of upsilons in the dimuon data. By counting the number of the upsilons before and after the SVX requirements, we are able to obtain the SVX efficiency for the dimuon data.

There are 3632 ± 60 upsilons before the SVX and 2457 ± 50 after the SVX requirement. So, $\epsilon_{SVX} = 0.68 \pm 0.02$. (Figure 6.4)

According the Figure 6.3, the kinematics of the upsilons are similar to those of the rest of the data, so we can use ϵ_{SVX} for the whole data set.

6.3.3 ϵ_{CMP}

We can determine ϵ_{CMP} by counting the number of upsilons before and after the CMP requirement as indicated in Figure 6.5. In our dimuon data, at least one muon has been required to have CMP confirmation in the Level 3 trigger selection. We define N_{1CMP} to be the number of events that has at least one muon passing CMP

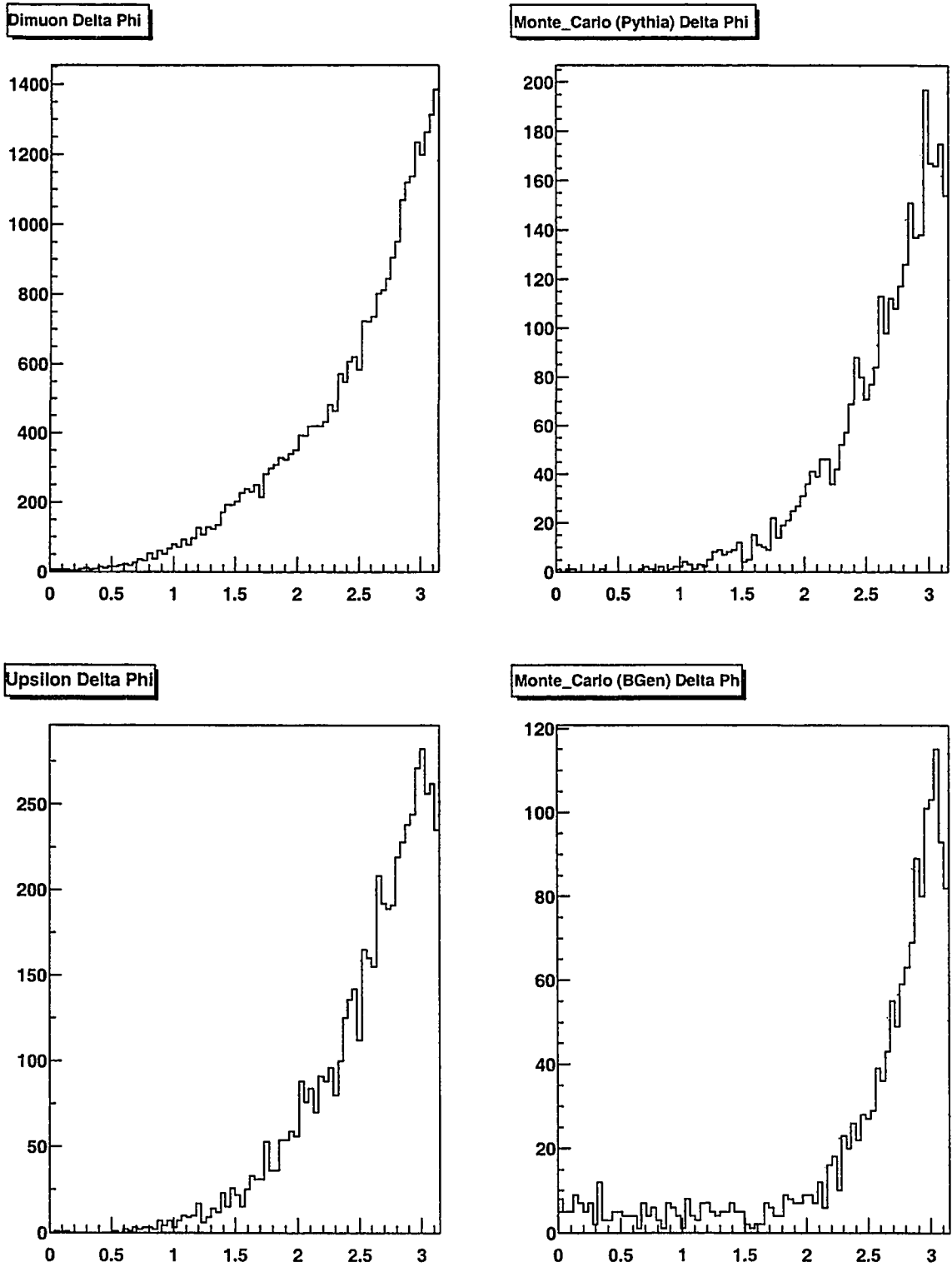
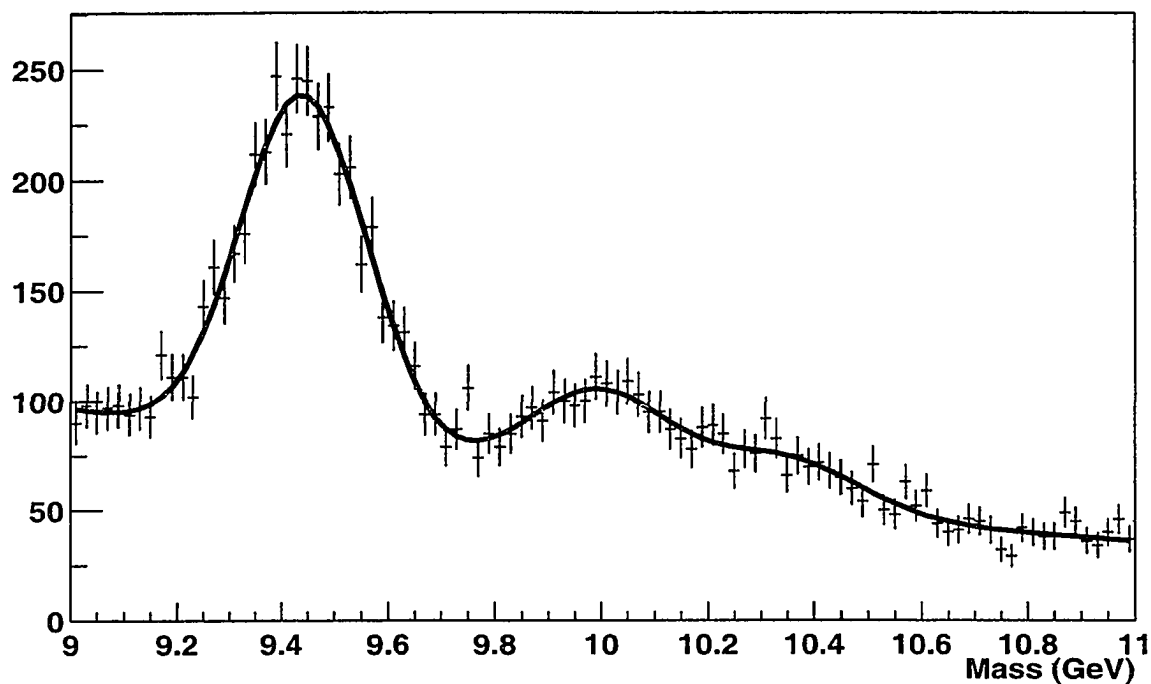


Figure 6.3: Transverse opening angle $\Delta\Phi$ of dimuon events from different sources. We can see they have very similar kinematics.

The Opposite-Sign Upsilons Before SVX



The Opposite-Sign Upsilons After SVX

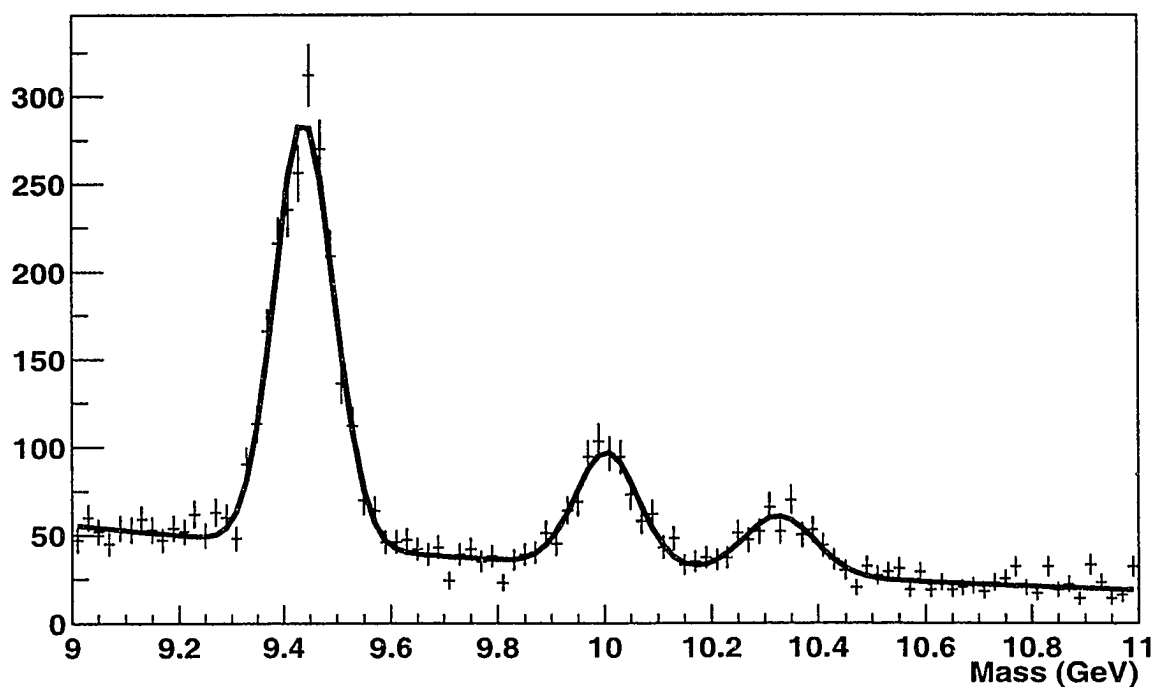


Figure 6.4: The figures for calculating the SVX efficiencies. We obtain the efficiencies by counting the number of upsilons in the mass spectrum before and after the criteria.

and N_{2CMP} to be the number of events having two muon passing CMP. A simple calculation shows that:

$$\frac{N_{2CMP}}{N_{1CMP}} = \frac{\epsilon_{CMP}}{2 - \epsilon_{CMP}} \quad (6.3)$$

The number of upsilons decreased from 2088 ± 45 to 1836 ± 42 before and after the CMP requirements according to the fit in Figure 6.5. Solving the equation 6.3, we obtain $\epsilon_{CMP} = 0.936 \pm 0.016$. This result is consistent with the result obtained by Intae Yu, $\epsilon_{CMP} = 0.94 \pm 0.01$ ([1]), for Run Ia.

6.3.4 The Level 3 Efficiency ϵ_{L3}

The Level 3 trigger we use, PSIB_DIMUON_HIGHMASS_V1, requires:

- Each event has at least 1 muon that is CMP confirmed.
- The dimuon invariant mass is between $2.7 \text{ GeV}/c^2$ and $150 \text{ GeV}/c^2$.
- Both muons are from $|z| < 35.0 \text{ cm}$ region.
- Both muons have $p_T > 1.4 \text{ GeV}/c$

During the Level 3 reconstruction of the dimuon data, besides removing low p_T events and matching the CTC tracks with the muon segments, the trigger system also apply an explicit criteria on z component of the muon tracks before writing the data into the mass storage. The requirement for both muons to be from $|z| < 35.0 \text{ cm}$ is effectively equivalent to requiring the primary vertex to have $|z| < 35.0 \text{ cm}$. In Run IB, the z of the primary vertex of a $p\bar{p}$ has a Gaussian distribution with $\sigma \approx 29 \text{ cm}$. However, the length of the SVX detector active region is 51.1 cm around the interaction spot. Therefore the SVX only covers about 60% of the decays. Decays with primary vertices of large z component have relatively small probabilities of having SVX tracks. Events without SVX information are usually of little interest for detailed studies, but they take up a considerable amount of processing time and storage space. Therefore, in Level 3, only events with both muons from $|z| < 35 \text{ cm}$ region are saved for offline processing.

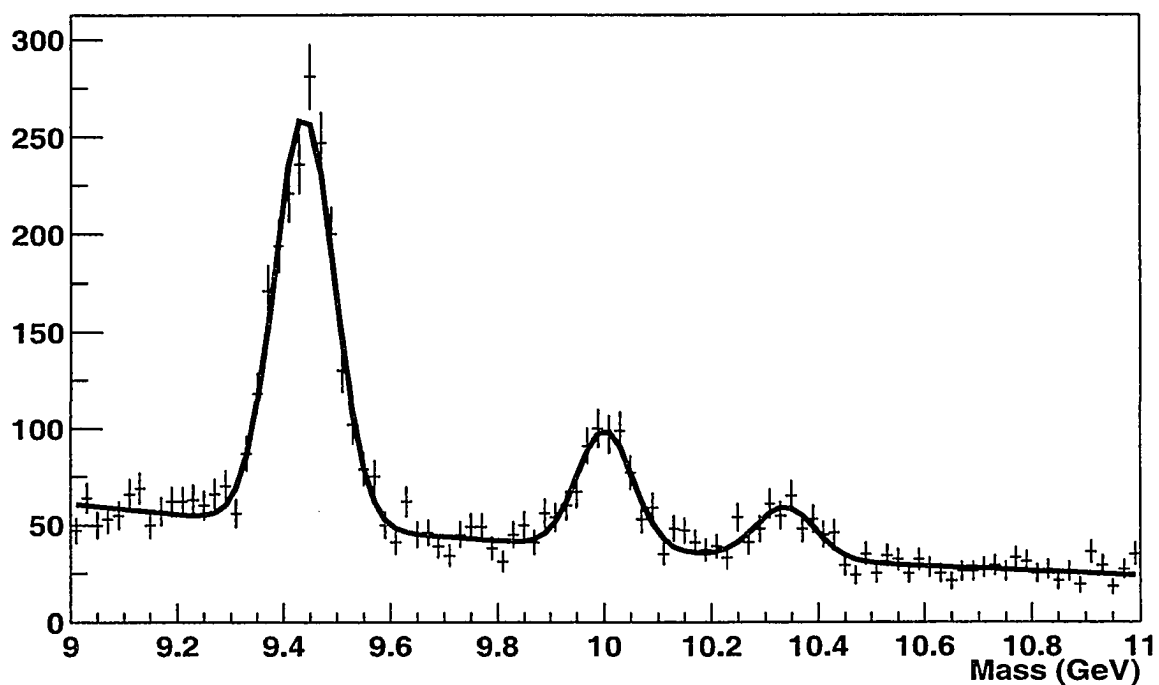
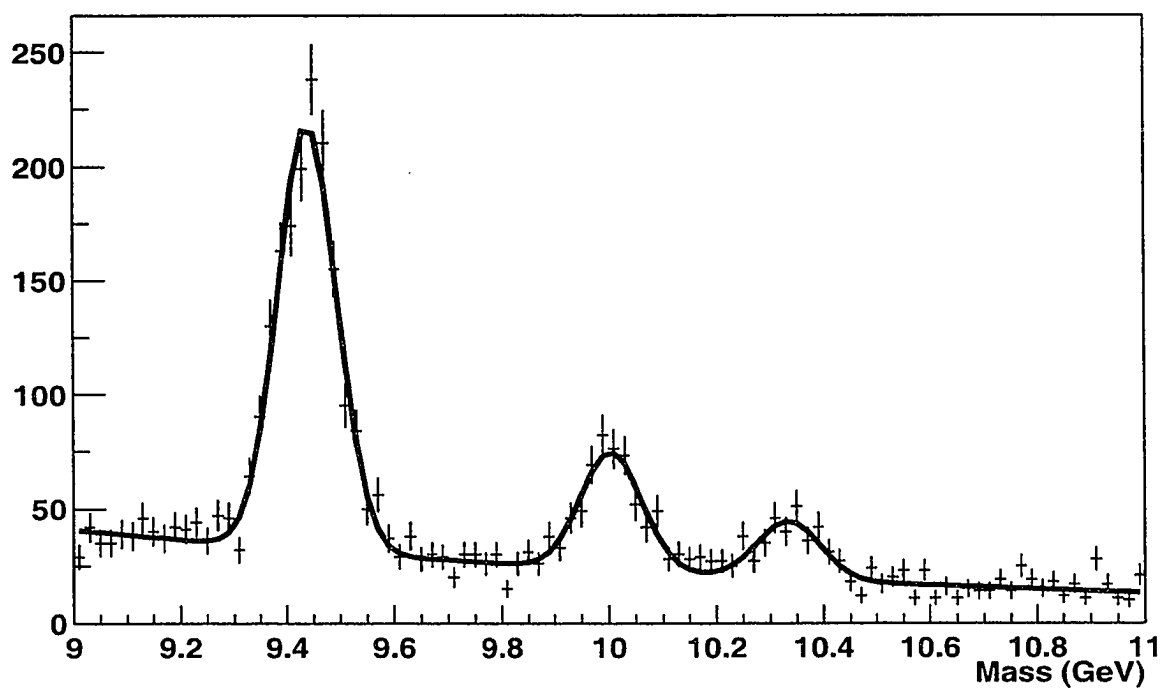
Upsilon's Before CMP**UPSILONS After CMP**

Figure 6.5: Upsilon's before and after requiring the second CMP

The efficiency for passing our Level 3 trigger are measured using the upsilon dimuon data set from PSIB_DIMUON_UPSILON_V1 trigger. This Level 3 trigger is similar to our dimuon L3 trigger but it does not need CMP confirmation and uses opposite-sign dimuons in the upsilon mass region $(8.5, 11, 4)$ GeV/c² only. Also, this trigger does not require $|z| < 35$ cm and thus provides a basis for measuring z efficiency for our dimuon trigger.

The tracking efficiency of Level 3 ($\epsilon_{L3-tracking}$) was measured in previous CDF analysis [65] [64] to be 0.97 ± 0.02 . As for the efficiency for $|z| < 35$ cm requirement in Level 3, ϵ_{L3-z} , we apply the z requirement to the upsilon dimuon set and count the number of upsilons before and after the requirement. The data set before the $|z| < 35$ cm requirement has the following criteria in addition to the upsilon Level 3 trigger:

- Both muons have $p_T > 3$ GeV/c
- Both muons have CMP confirmation
- Trigger bits are set
- Passing the track quality requirements

Since we have defined ϵ_{SVX} to be after ϵ_{L3} , no SVX requirement is applied here and we use the beam constraint instead of the SVX information in this calculation.

We count 3900 ± 62 upsilons before the z requirement and 2907 ± 54 after it. Therefore the efficiency $\epsilon_{L3-z} = 0.745 \pm 0.018$.

The combined Level 3 efficiency $\epsilon_{L3} = \epsilon_{L3-tracking} \times \epsilon_{L3-z}$ is therefore 0.722 ± 0.031 .

6.3.5 Other Efficiencies

The other efficiencies can be obtained from the upsilon cross section analysis [64]. We list all the CDF detector efficiencies in Table 6.7.

Source	Name	Efficiency
SVX Efficiency	ϵ_{svx}	0.68 ± 0.02
Trigger Efficiency	ϵ_{trig}	0.75 ± 0.04 [64]
Normalization Correction	ϵ_{norm}	0.88 ± 0.04 [66][64]
CTC Tracking Efficiency	ϵ_{ctc}^2	0.98 ± 0.02 [67][64]
Muon Stub Efficiency	ϵ_{cmu}^2	0.966 ± 0.006 [68][64]
CTC Muon Linking Efficiency	ϵ_{link}^2	0.996 ± 0.004 [69][64]
Muon Matching Efficiency	ϵ_{match}^2	0.974 ± 0.004 [70][64]
CMP Efficiency	ϵ_{CMP}^2	0.876 ± 0.030
L3 Tracking and $ z < 35cm$ Efficiency	ϵ_{L3}	0.722 ± 0.031
The Combined Efficiency	ϵ_{CDF}	0.261 ± 0.025

Table 6.7: The list of (di-)muon event efficiencies and their sources.

6.3.6 Accounting for Fake Tracks

Despite the selection criteria, some of the selected muons may be fakes. The so-called fakes are tracks that pass all the muon criteria but are not muons. We need to have an estimation of the fake muon content of the $b\bar{b}$ events because we are interested in only the real b-muon fraction in the dimuon data.

According to Chapter 5, most of the fake muons come from prompt sources and can be easily separated from the b-muons with our impact parameter fitting method. However, in addition to prompt fake muons the data may contain b-like fake muons, that is fake muons with tracks that have large impact parameters. Such tracks naturally arise as byproducts of b-hadron decay. We defined $P(\mu)$ as the probability of a b-like track with $p_T \geq 3$ GeV/c, satisfying CMU, CMP fiduciality criteria and having CMU, CMP hits, to be a muon. Assuming the probability of finding fakes in either leg of a dimuon event are independent, we can use the events with 1 or 2 CMP confirmed muons to determine $P(\mu)$ as indicated in Table 6.8.

Here, $N_{b\bar{b}-1CMP}$ is the number of $b\bar{b}$ dimuon events with both legs CMP fiducial and both have CMU hits but only one has a CMP hit. $N_{b\bar{b}-2CMP}$ is the number of $b\bar{b}$ dimuon events with both legs CMP fiducial and both have CMU and CMP hits. The efficiency of a fake muon (with $p_T > 3$ GeV/c and being CMP fiducial) to be found

	2 Fakes	1 Fake and 1 Muon	2 Muons
$\frac{N_{b\bar{b}-1CMP}}{N_{b\bar{b}-2CMP}}$	$\frac{2\epsilon_f(1-\epsilon_f)}{\epsilon_f^2}$	$\frac{\epsilon_f(1-\epsilon_\mu)+(1-\epsilon_f)\epsilon_\mu}{\epsilon_f\epsilon_\mu}$	$\frac{2\epsilon_\mu(1-\epsilon_\mu)}{\epsilon_\mu^2}$
Weight for $\frac{N_{b\bar{b}-1CMP}}{N_{b\bar{b}-2CMP}}$	$(1 - P(\mu))^2$	$2(1 - P(\mu))P(\mu)$	$P^2(\mu)$

Table 6.8: $N_{b\bar{b}-1CMP}/N_{b\bar{b}-2CMP}$ under different circumstances.

with a matched CMP stub is $\epsilon_f = 0.42 \pm .02$ according to Colin Gay et al. [71] The efficiency of a muon (with $p_T > 3$ GeV/c and being CMP fiducial) to be found with a matched CMP stub is $\epsilon_\mu = 0.936 \pm 0.016$ (Section 6.3.3).

The weighted mean of $\frac{N_{b\bar{b}-1CMP}}{N_{b\bar{b}-2CMP}}$ is what we can measure. Equation 6.4 shows how we are able to calculate $P(\mu)$ with the weights in Table 6.8.

$$\begin{aligned} \frac{N_{b\bar{b}-1CMP}}{N_{b\bar{b}-2CMP}} = & \frac{2\epsilon_f(1-\epsilon_f)}{\epsilon_f^2} * (1 - P(\mu))^2 \\ & + \frac{\epsilon_f(1-\epsilon_\mu)+(1-\epsilon_f)\epsilon_\mu}{\epsilon_f\epsilon_\mu} * 2(1 - P(\mu))P(\mu) \\ & + \frac{2\epsilon_\mu(1-\epsilon_\mu)}{\epsilon_\mu^2} * P^2(\mu) \end{aligned} \quad (6.4)$$

Simplifying it, we obtain:

$$\frac{N_{b\bar{b}-1CMP}}{N_{b\bar{b}-2CMP}} = 2\left(\frac{1 - P(\mu)}{\epsilon_f} + \frac{P(\mu)}{\epsilon_\mu} - 1\right) \quad (6.5)$$

We obtain $N_{b\bar{b}-1CMP}$ and $N_{b\bar{b}-2CMP}$ by fitting the impact parameter distribution of two sets of data:

- The dimuon data set with both legs being within the CMP fiducial region and having matched CMU stubs, but only one has a CMP hit.
- The dimuon data set with both legs being within the CMP fiducial region and both having CMU and CMP hits.

Here we explicitly require both tracks of the dimuon events to be CMU-CMP fiducial in all the fits. Putting the results into equation 6.5, we are able to calculate the P_μ . In fact, we divide the dimuon data into two parts: LS (Figures 6.6 and 6.7) and OS (Figures 6.8 and 6.9) case and calculate $P(\mu)$ separately. This is because

The Like_Sign fitting results(5par): (Projected to one dim)

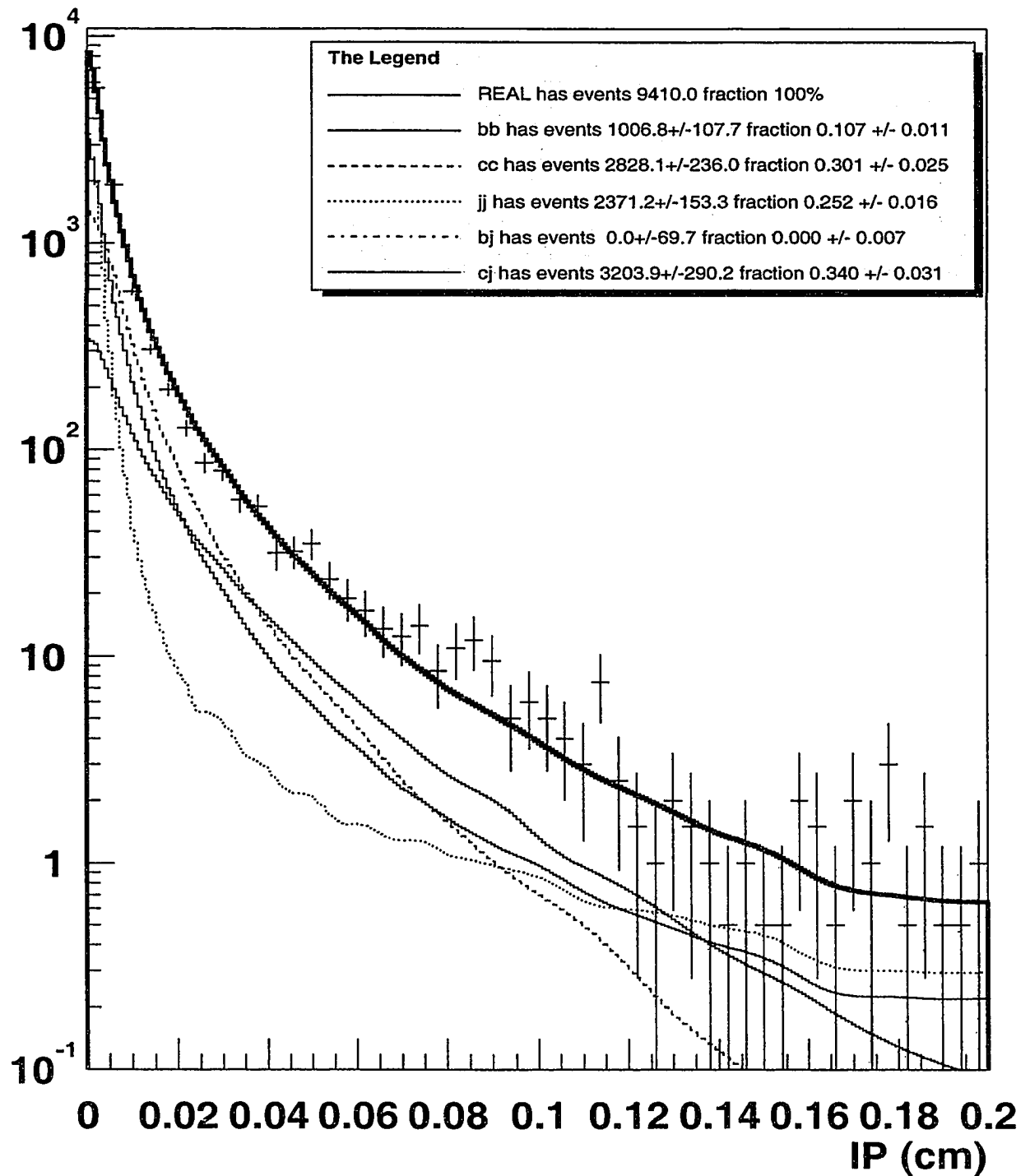


Figure 6.6: Impact parameter fit for the like-sign dimuon data with both legs CMP fiducial and having CMU hits, we fit the subset of only 1 CMP hit (this plot) and the subset of 2 CMP hits (next plot) to obtain the b-muon fractions and calculate $P(\mu)$.

The Like_Sign fitting results(5par): (Projected to one dim)

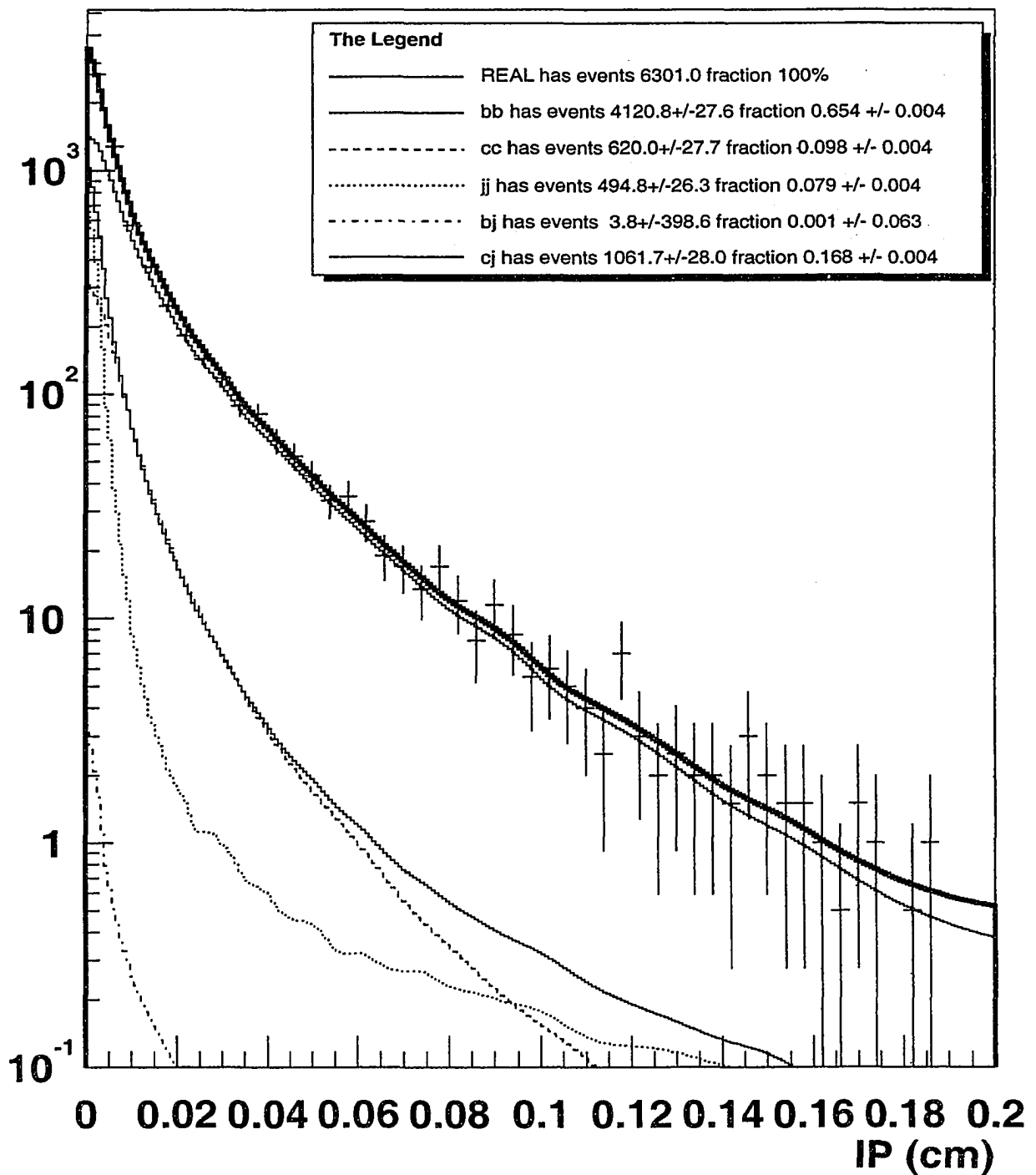


Figure 6.7: Impact parameter fit for the like-sign dimuon data with both legs CMP fiducial and having CMU hits, we fit the subset of only 1 CMP hit (last plot) and the subset of 2 CMP hits (this plot) to obtain the b-muon fractions and calculate $P(\mu)$.

The Opposite-Sign fitting results(5par): (Projected to one dim)

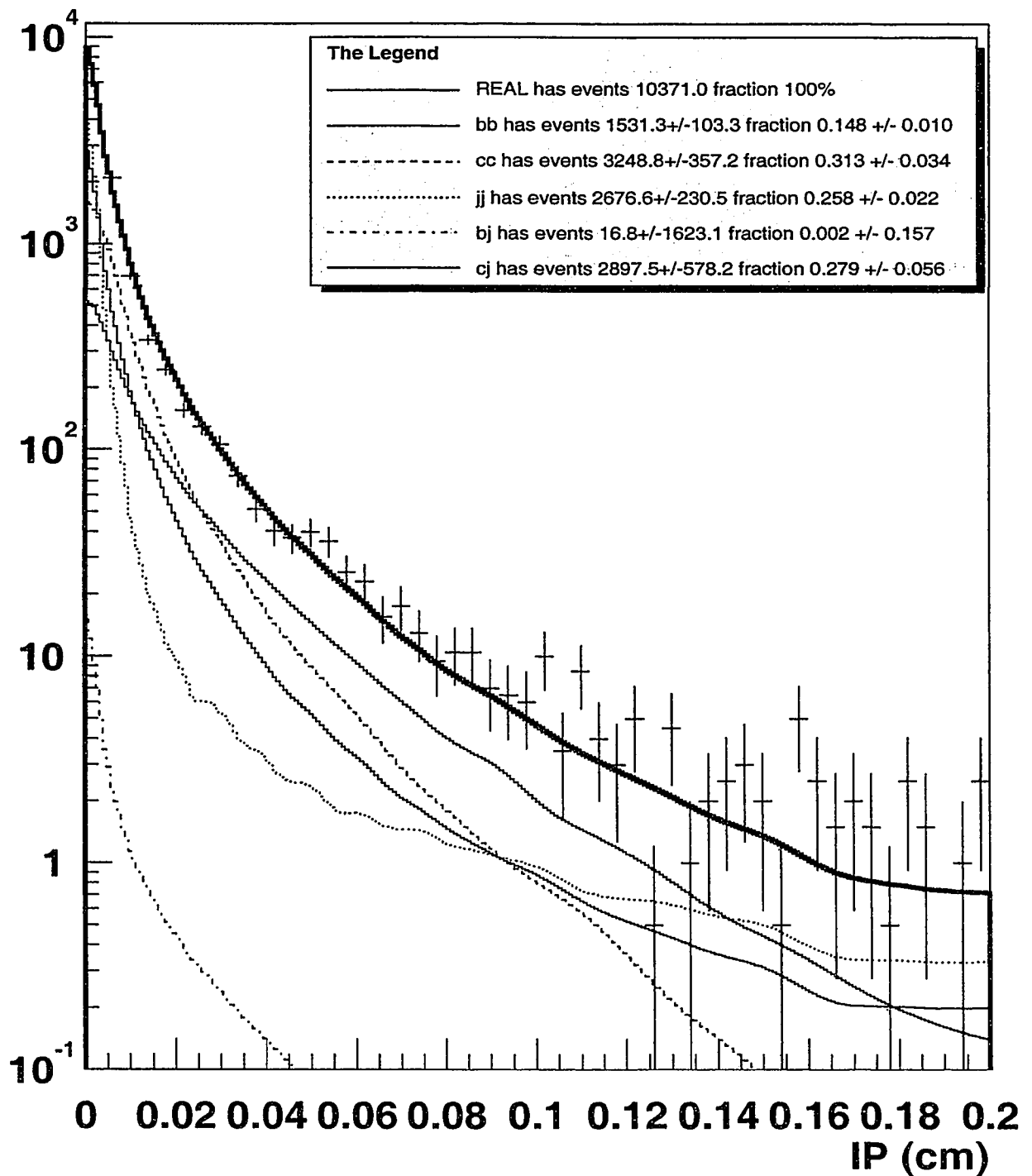


Figure 6.8: Impact parameter fit for the opposite-sign dimuon data with both legs CMP fiducial and having CMU hits, we fit the subset of only 1 CMP hit (this plot) and the subset of 2 CMP hits (next plot) to obtain the b-muon fractions and calculate $P(\mu)$.

The Opposite-Sign fitting results(5par): (Projected to one dim)

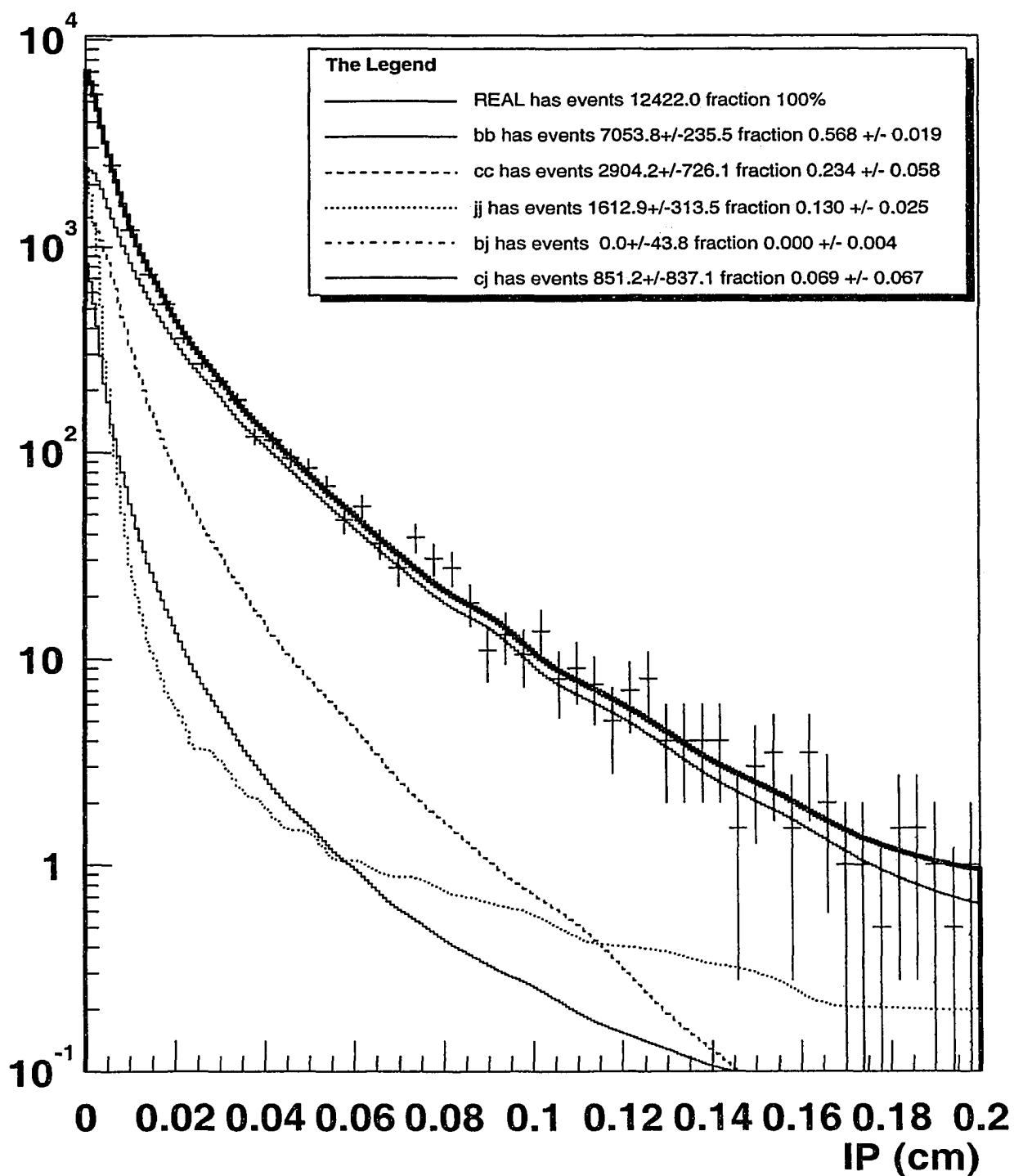


Figure 6.9: Impact parameter fit for the opposite-sign dimuon data set with both legs CMP fiducial and having CMU hits, we fit the subset of only 1 CMP hit (last plot) and the subset of 2 CMP hits (this plot) to obtain the b-muon fractions and calculate $P(\mu)$.

$P(\mu)$ is different for these two cases. Since there are more dimuon events from $b\bar{b}$ in the OS case than in LS case, while the number of fake events should be the same in LS and OS, we should expect $P(\mu)$ to be higher in OS events. In other words, the chance for a b-like track in the OS events to be a b-muon is larger than the chance for a b-like track in the LS events to be a b-muon.

	LS	OS
Number of $b\bar{b}$ events from the fitting ($N_{b\bar{b}}$)	4805 ± 151	8396 ± 203
$P(\mu)$	0.956 ± 0.015	0.966 ± 0.012
Number of real dimuon events $\hat{N}_{b\bar{b}}$	4389 ± 196	7836 ± 271
Number of fake dimuon events	416 ± 196	540 ± 271

Table 6.9: The number of real $b\bar{b}$ dimuon events (\hat{N}) is the number of $b\bar{b}$ events from the impact parameter fit (N) times $P^2(\mu)$. We can see that the number and fraction of fake dimuon events for LS and OS are equal within the uncertainties.

We expect to have the same number of fake dimuon events (i.e. dimuon events with at least one fake muon) in LS and OS under the assumption that fake muons are randomly distributed in charge. The results obtained in Figure 6.9 are consistent with this expectation. LS and OS have a similar number of fake events within uncertainties.

The combined $P^2(\mu)$ for both LS and OS is 0.926 ± 0.030 according to Table 6.9.

6.3.7 Calculating the Cross Sections

The actual numbers of dimuons from $b\bar{b}$ in the three dimuon data subsets are obtained by fitting the impact parameter distributions of each subset with a linear combination of bb , cc , jj , bj and cj signals described in Chapter 4.

Since the impact parameter distributions are slightly different for muons at different p_T bins, we use a convolution of b muons IP distributions in different bins as our template. (Equation 6.6)

$$\begin{aligned}
 f_{bb}^{(3-5)} &= (f_b(x)^{(3-5)} \times f_b(y) + f_b(x) \times f_b(y)^{(3-5)})/2 \\
 f_{bb}^{(5-7)} &= (f_b(x)^{(5-7)} \times f_b(y) + f_b(x) \times f_b(y)^{(5-7)})/2 \\
 f_{bb}^{(7-\infty)} &= (f_b(x)^{(7-\infty)} \times f_b(y) + f_b(x) \times f_b(y)^{(7-\infty)})/2
 \end{aligned} \tag{6.6}$$

The 3-5 GeV fitting results(5par): (Projected to one dim)

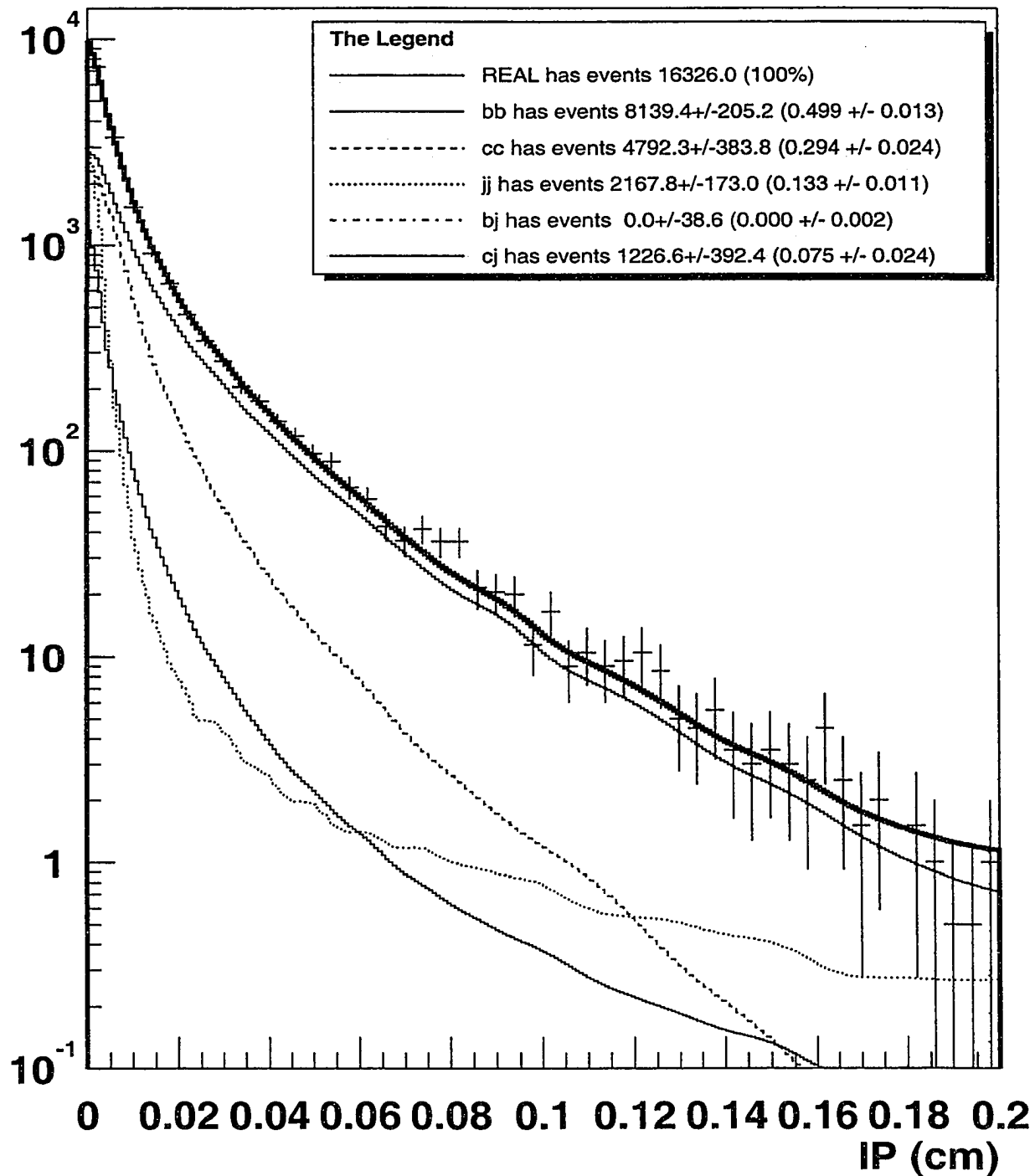


Figure 6.10: Impact Parameter Fitting in the First Subset. We use the convoluted bb muon impact parameter template in the fitting.

The 5-7 GeV fitting results(5par): (Projected to one dim)

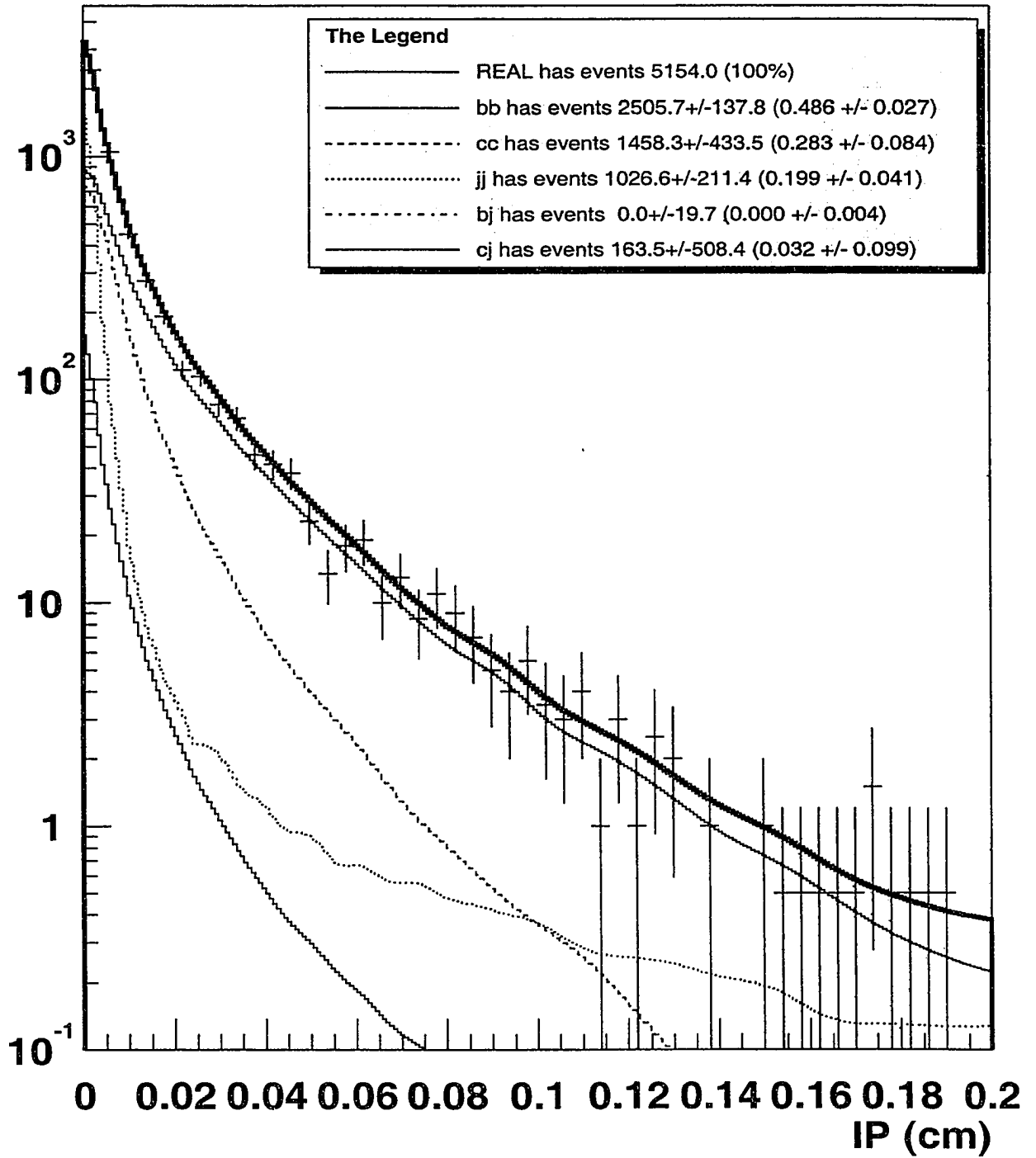


Figure 6.11: Impact Parameter Fitting in the Second Subset. We use the convoluted bb muon impact parameter template in the fitting.

The 7- GeV fitting results(5par): (Projected to one dim)

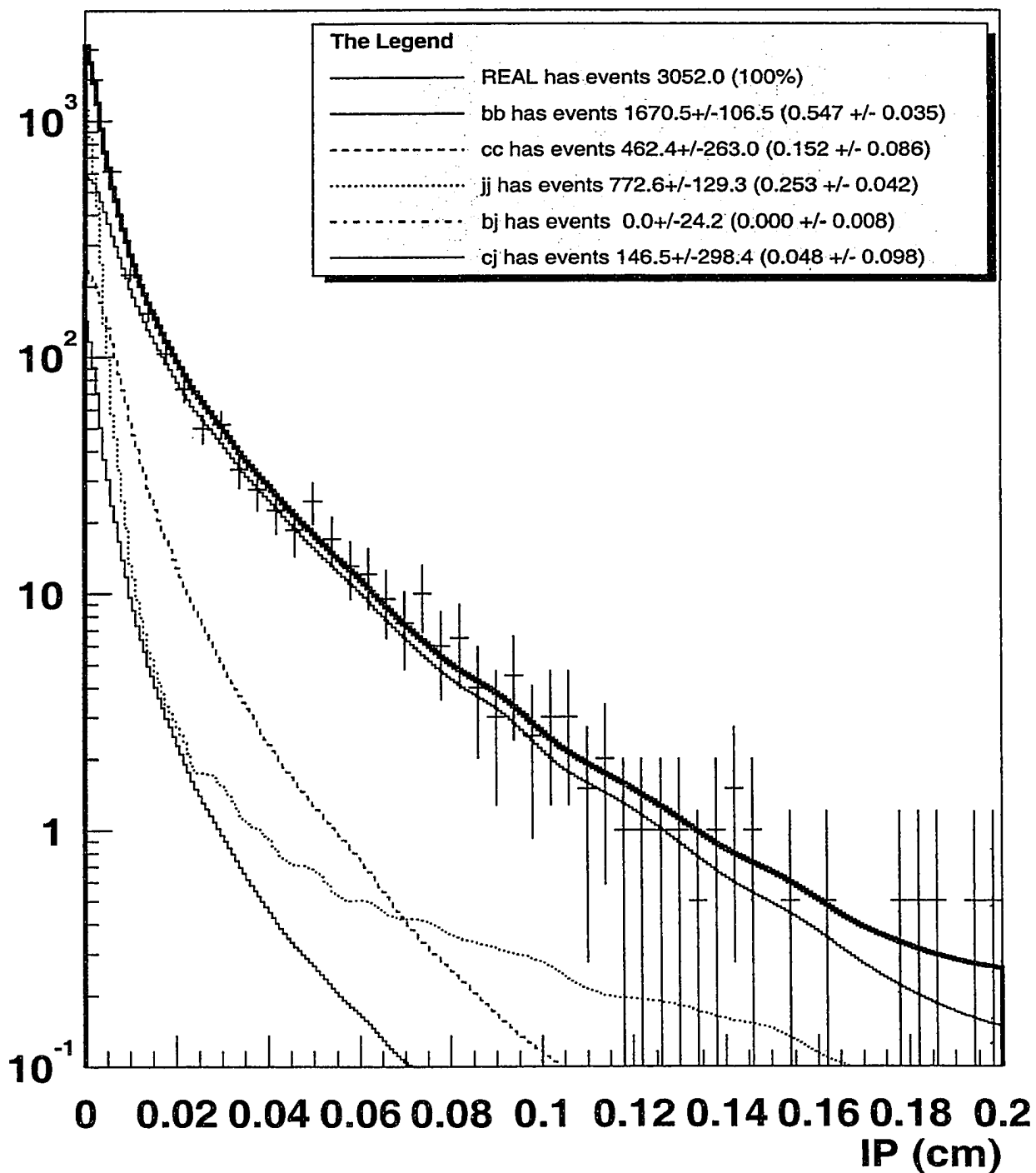


Figure 6.12: Impact Parameter Fitting in the Third Subset. We use the convoluted bb muon impact parameter template in the fitting.

Here $f_b(*)$ is the overall IP distribution of b muons and $f_b(*)^{(3-5)}$ is the IP distribution of b muons in the (3, 5) GeV/c momentum bin. Similar rule holds for $f_b(*)^{(5-7)}$ and $f_b(*)^{(7-\infty)}$. The $f_{bb}^{(3-5)}$ is our 2-d IP template for $p_T(\mu_1) > 3$ and $p_T(\mu_2) \in (3, 5)$. Similar for $f_{bb}^{(5-7)}$ and $f_{bb}^{(7-\infty)}$.

By fitting these templates into the three subsets. We obtain the Figures 6.10, 6.11 and 6.12. The number of $b\bar{b}$ muon pairs are listed in Table 6.10.

Second Muon p_T Criteria	Value	Uncertainty
3 – 5 GeV/c	8139	205
5 – 7 GeV/c	2506	138
7 – ∞ GeV/c	1671	107

Table 6.10: $N_{b\bar{b}}$ from the fittings in Figures 6.10, 6.11 and 6.12

We can use the $P^2(\mu)$ for the whole dimuon data set to calculate the actual number of $b\bar{b}$ muons in each of these bins (Table 6.11) because in $p_T > 3$ GeV/c region, the detector efficiencies (ϵ_μ and ϵ_f) are not sensitive to p_T . $\tilde{N}_{b\bar{b}}$ is the actual number of $b\bar{b}$

Second Muon p_T Criteria	Value	Uncertainty
3 – 5 GeV/c	7537	314
5 – 7 GeV/c	2321	149
7 – ∞ GeV/c	1547	111

Table 6.11: $\tilde{N}_{b\bar{b}}$ is from $N_{b\bar{b}}$ after accounting for the fakes.

muons in our dimuon data. Using Equation 4.1 and propagating all the uncertainties, we obtain the results displayed in Table 6.12.

In Table 6.12, the systematic uncertainties are presented separately:

- Luminosity Uncertainty: the systematic uncertainty from uncertainty of luminosity measurement.
- Branching Ratio Uncertainty: the systematic uncertainty from uncertainty of branching ratios listed in Table 5.3.

$p_T(b)$	$\geq 6.5 \text{ GeV}/c$	$\geq 6.5 \text{ GeV}/c$	$\geq 6.5 \text{ GeV}/c$
$p_T(b)$	$> 6.5 \text{ GeV}/c$	$> 8.75 \text{ GeV}/c$	$> 12.25 \text{ GeV}/c$
Cross Section (μb)	1.876	1.154	0.533
Statistical Uncertainty	0.047	0.064	0.034
Total Systematic Uncertainty	0.235	0.147	0.071
Luminosity Uncertainty	0.075	0.046	0.021
Branching Ratio Uncertainty	0.064	0.039	0.018
Efficiency Uncertainty	0.181	0.111	0.051
Acceptance Statistical Uncertainty	0.084	0.047	0.024
Uncertainty from b-hadron Species	0.041	0.044	0.026
Uncertainty from Cascades	0.019	0.013	0.005
Uncertainty Due to Fake Muons	0.061	0.037	0.017

Table 6.12: The $b\bar{b}$ cross sections and assigned uncertainties in the three independent p_T bins.

- Efficiency Uncertainty: the systematic uncertainty from uncertainty of Efficiencies measurements.
- Acceptance Statistical Uncertainty: the systematic uncertainty due to the Monte Carlo statistical uncertainty in the acceptance calculations.
- Uncertainty from b-hadron Species Fractions: the systematic uncertainty from the uncertainties of the world average b-hadron Species Fractions.
- Uncertainty Due to Fake Muons: the systematic uncertainty from the uncertainty of $P(\mu)$ estimation.

Figure 6.1 shows the comparison of our measured cross sections, Run IA measurements and NLO QCD predictions. Both Run IA and Run IB results are higher than the NLO QCD predictions.

Cross Section

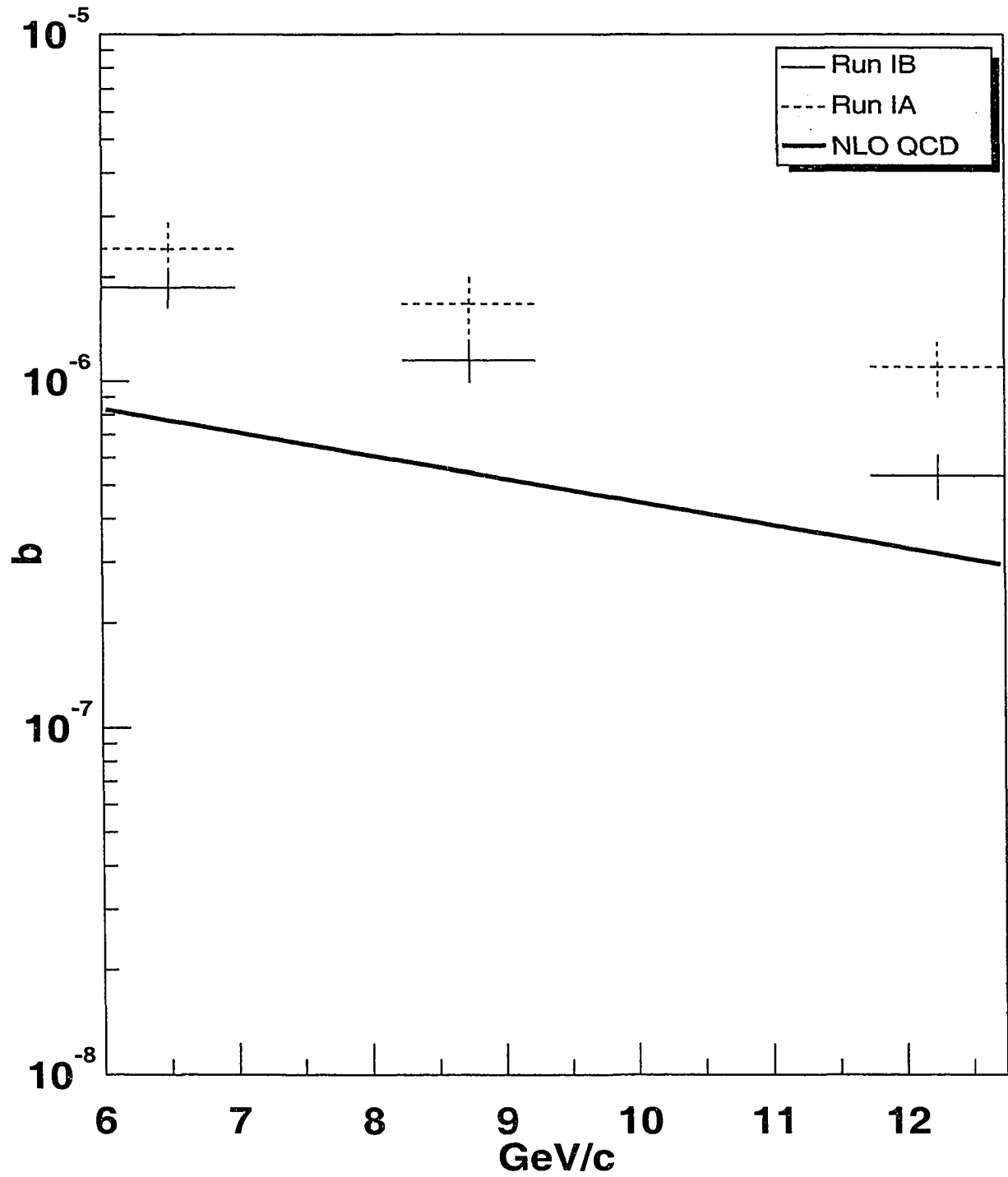


Figure 6.13: The Cross Sections Measured in Run IB compared to Run IA and the NLO QCD prediction. The x axis is the lower boundary of the b quark p_T . The y axis is the cross section.

Chapter 7

The Time-Integrated $B\bar{B}$ Mixing Parameter $\bar{\chi}$

In Chapter 4, we discussed the method for calculating the $B\bar{B}$ mixing parameter. According to Equation 7.1, we need to know the wrong-sign cascade muons ratio r_{ws} , the number of like-sign $b\bar{b}$ muons N_{ls} and the number of opposite-sign $b\bar{b}$ muons N_{os} to calculate $\bar{\chi}$.

$$R = \frac{N_{ls}}{N_{os}} = \frac{2r_{ws}(\bar{\chi}^2 + (1 - \bar{\chi})^2) + 2\bar{\chi}(1 - \bar{\chi})(1 + r_{ws}^2)}{(\bar{\chi}^2 + (1 - \bar{\chi})^2)(1 + r_{ws}^2) + 4r_{ws}\bar{\chi}(1 - \bar{\chi})} \quad (7.1)$$

7.1 Wrong-Sign Cascade Muons Ratio r_{ws}

The definition of the wrong-sign cascade muons ration r_{ws} is

$$r_{ws} = N_{ws}/N_{rs} \quad (7.2)$$

where N_{ws} is the number of muons that carry an opposite electric charge from its ancestor b quark and N_{rs} is the number of the muons that carry the same sign of electric charge as its ancestor b quark.

We calculate the r_{ws} using a similar generator level Monte Carlo simulation as Chapter 6. We use Pythia and QQ to generate $b\bar{b}$ events. We choose a low b quark p_T threshold (4.0 GeV) and a rapidity constraint $|y(b)| < 1$ in Pythia. We use the dimuons passing the selection criteria:

- At least 2 muons are produced in each event; muons from direct and cascade decays are all counted.
- Both muon's $p_T > 3 \text{ GeV}/c$
- The dimuon mass is required to be $\geq 5 \text{ GeV}/c^2$
- Both muons are required to be CMU and CMP fiducial (CMUSWM is employed with energy loss and multiple scattering turned off).

The muons' lineage information is recorded during the simulations, therefore we are able to count N_{ws} and N_{rs} separately in the Monte Carlo results. However, due to the difference between the most updated B semileptonic branching ratios and relative B species fractions and Pythia/QQ's default values, we again have to reweight the hadrons in the simulations to get a more accurate N_{ws} and N_{rs} . The reweighting is done in the same way as described in Section 6.2.1 using the recorded muon lineage information. The systematic uncertainties are calculated by retossing the B semileptonic branching ratios and relative B species fractions away from their central values with Gaussian distributions set by their uncertainties. The result for r_{ws} is given in Table 7.1. For reference we can determine the sequential (or cascade) fraction,

r_{ws}	0.135
Uncertainty	0.007
Uncertainty due to Monte Carlo statistical uncertainty	0.005
Systematic uncertainty: from b-hadron Species Fractions	0.003
Systematic uncertainty: from Cascades Branching Ratio	0.004

Table 7.1: The result for r_{ws} and its uncertainties

normally defined as:

$$f_{seq} = \frac{N_{cascades}}{N_{all}} \quad (7.3)$$

in which $N_{cascades}$ is the number of cascade decays (right-sign and wrong-sign) and N_{all} includes all of the direct and cascade decays. Using the same Monte Carlo sample as we have used in the r_{ws} calculation, the result for f_{seq} is given in Table 7.2.

f_{seq}	0.154
Uncertainty	0.008
Uncertainty due to Monte Carlo statistical uncertainty	0.006
Systematic uncertainty: from b-hadron Species Fractions	0.003
Systematic uncertainty: from cascades	0.005

Table 7.2: The value for f_{seq} and its uncertainties

In fact r_{ws} and f_{seq} are similar in their definitions and sometimes confusing. When we have a sequential decay, in most cases it generates a wrong-sign muon ($b \rightarrow c \rightarrow \mu X$). However, there exist many special cases such as the one in Figure 4.1 or $b \rightarrow \tau \rightarrow \mu$. Since sometimes a sequential decay could generate a right-sign muon, we have to use r_{ws} when dealing with Like-Sign and Opposite-Sign dimuon analysis.

7.2 N_{ls} and N_{os}

Equation 4.2 also needs another input: R . We have defined R to be the ratio of number of like-sign $b\bar{b}$ muon (N_{ls}) to opposite-sign $b\bar{b}$ muon pairs (N_{os}). To obtain N_{ls} and N_{os} , we do the same impact parameter fitting to the like-sign part and the opposite-sign part of the dimuon data set. We do not require dimuon trigger (DIMUTG) in the dimuon data set to reduce the statistical uncertainties. The purpose of the dimuon trigger is to apply measured triggering efficiency curves to data. Since triggering efficiency are almost the same for LS and OS events, the ratio $R = N_{ls}/N_{os}$ is insensitive to whether DIMUTG is applied. We also remove the upsilon mass regions in the dimuon data sets because these regions are dominated by dimuons from Υ decays which are considered a background to our $b\bar{b}$ muons. Removing these signals helps reducing the uncertainties in the fittings.

The Figures 7.1 7.2 and 7.3 show the IP fittings with the whole dimuon data set, LS dimuon data set and OS dimuon data set. The fitting results are shown in the upper-right corners of the figures. We are only interested in the $b\bar{b}$ fractions.

Although the fittings for the whole dimuon data set is not necessary for deriving

R, we do Figure 7.1 as a double check of our method. Table 7.3 shows the consistency of the fittings. The sum of the LS and OS dimuon numbers are close to the dimuon number from the fitting for the whole data set.

	Value	Uncertainty
$b\bar{b}$ dimuons from LS fitting N_{ls}	4505	150
$b\bar{b}$ dimuons from OS fitting N_{os}	8396	203
Sum of $b\bar{b}$ dimuons from LS and OS fitting $N_{ls} + N_{os}$	12901	252
$b\bar{b}$ dimuons from fitting of the whole data set N_{All}	13215	250

Table 7.3: Results of the fittings accounting for fakes.

The LS and OS dimuon pair numbers are adjusted by $P^2(\mu)$ to account for fake muons. \tilde{N} is the number of $b\bar{b}$ dimuon events correcting for fakes. ($\tilde{N}_{ls} = N_{ls} * P_{ls}^2(\mu)$ and $\tilde{N}_{os} = N_{os} * P_{os}^2(\mu)$; refer to Table 6.9, Figure 7.2 and 7.3)

The value found for R is given in Table 7.4.

R	0.563
Over-All Uncertainty	0.036
Statistical Uncertainty	0.024
Systematic: All	0.027
Systematic: from b-hadron Species	0.014
Systematic: from Cascades	0.014
Systematic: from $P(\mu)$	0.019

Table 7.4: The value for R and the assigned uncertainties.

Here, the systematic uncertainty are due to the uncertainties of the world average b-hadron species and cascade branching ratios. Also the uncertainty of $P(\mu)$ measurement causes part of the systematic uncertainty.

With R and r_{ws} available, solving Equation 4.2, we obtain the result for $\bar{\chi}$ given in Table 7.5.

The All fitting results(5par): (Projected to one dim)

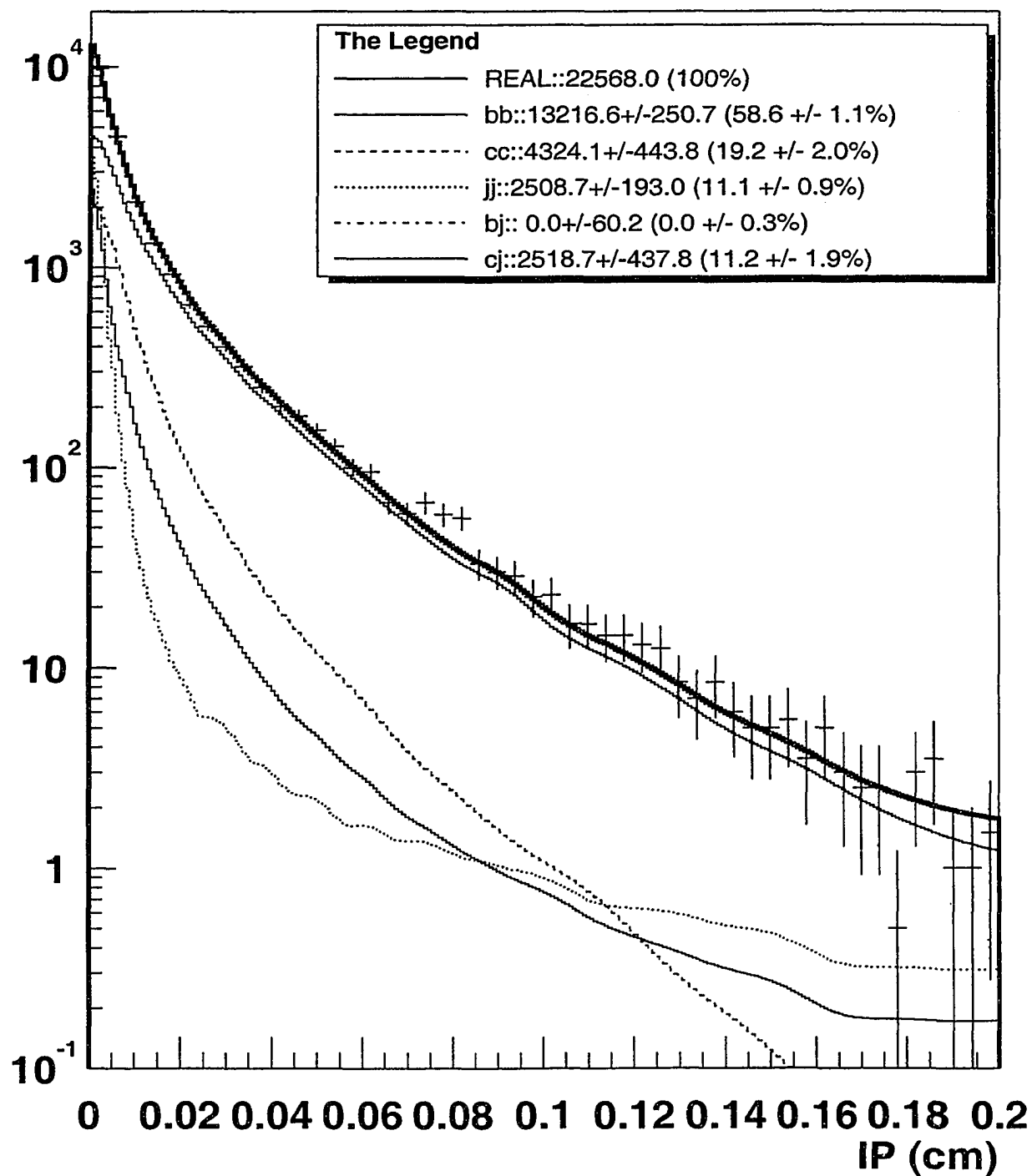


Figure 7.1: The impact parameter fit for all events (LS + OS)

The Like_Sign fitting results(5par): (Projected to one dim)

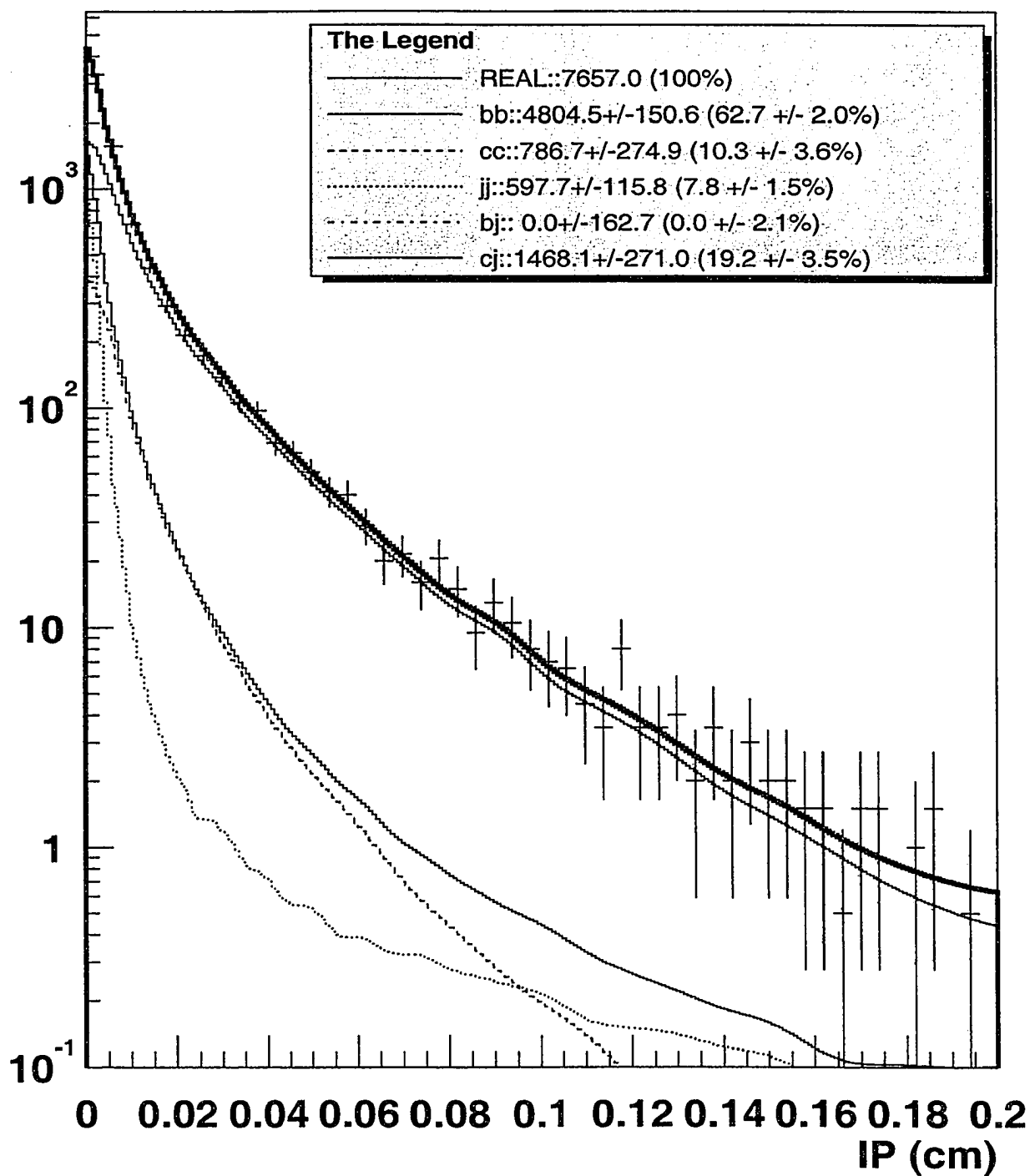


Figure 7.2: The like-sign impact parameter fit

The Opposite-Sign fitting results(5par): (Projected to one dim)

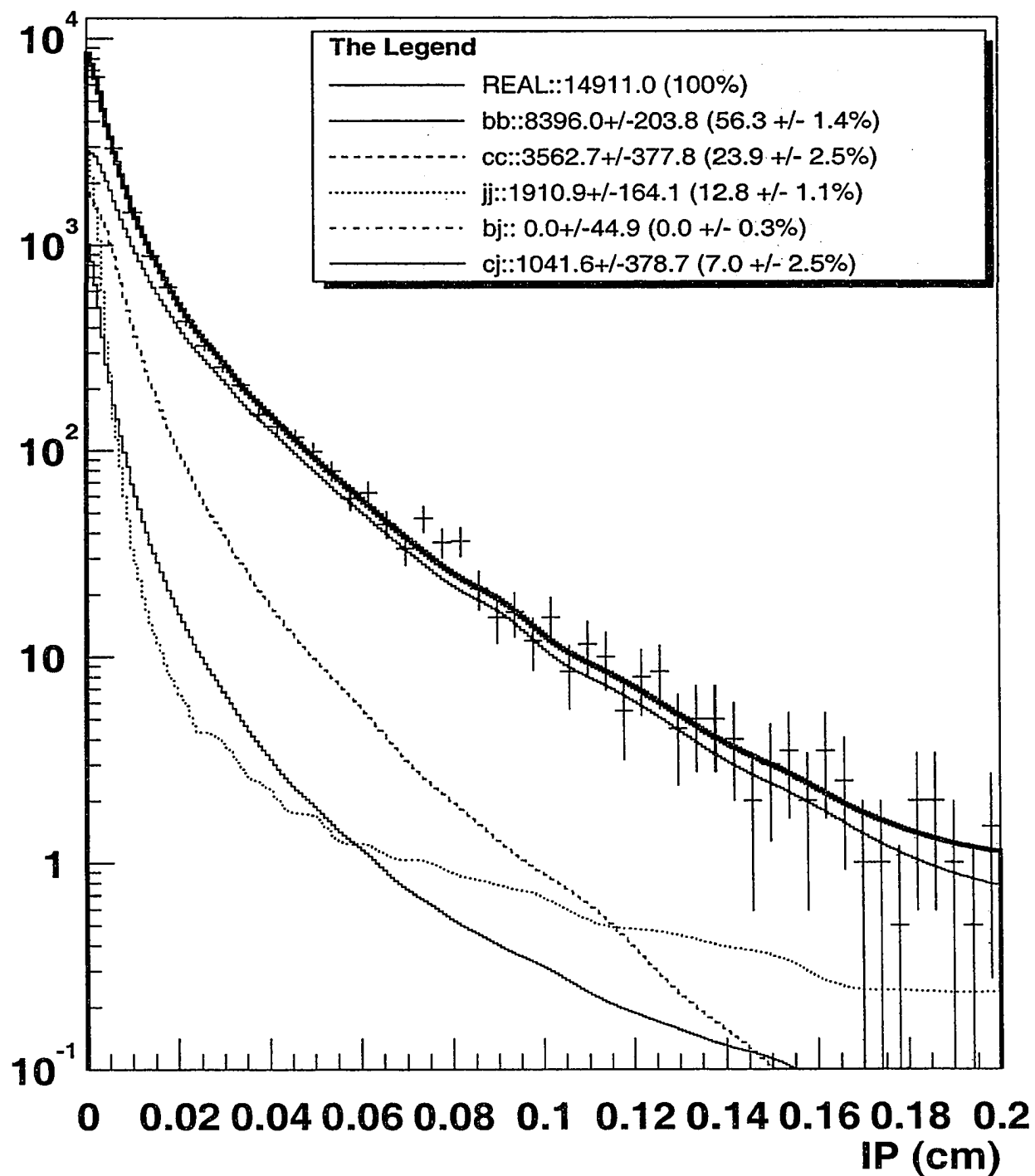


Figure 7.3: The opposite-sign impact parameter fit

$\bar{\chi}$	0.153
Uncertainty	0.019
Statistical Uncertainty	0.012
Systematic: All	0.015
Systematic: from Monte Carlo Tossing	0.004
Systematic: from b-hadron Species Fractions	0.007
Systematic: from Cascades	0.008
Systematic: from Fakes	0.010

Table 7.5: The value for $\bar{\chi}$ and the assigned uncertainties.

7.3 Comparisons with Other Analysis

Intae Yu obtained a result for $\bar{\chi}$ using Run IA dimuon data: $\bar{\chi} = 0.131 \pm 0.022(stat) \pm 0.016(sys)$. This result was consistent with the world average value of $\bar{\chi} \approx 0.133$ of that time. The world average has so far changed to $\bar{\chi} \approx 0.118 \pm 0.005$ [72]. Our measurement of $\bar{\chi} = 0.153 \pm 0.019$ is within two standard deviations of the world average. Paolo Giromini et al. [73] made an independent measurement of $\bar{\chi}$ using a similar Run I dataset but a different method and obtain the result: $\bar{\chi} = 0.152 \pm 0.007(stat) \pm 0.011(sys)$, which is consistent with our measurement.

Chapter 8

Conclusion

We have measured the the $b\bar{b}$ production cross section in $p\bar{p}$ collisions at $\sqrt{s} = 1.8$ TeV and the time-integrated average mixing parameter ($\bar{\chi}$) of B^0 and B_s^0 using Fermilab Run IB dimuon data in this analysis. These results sit between the Fermilab Run IA dimuon analysis done by Intae Yu [1] and the upcoming Run II dimuon analysis. The luminosity obtained in Run IB is about $88.0pb^{-1}$. Compared to the $20pb^{-1}$ luminosity in Run IA, it has about 4 times the data. The enhancements in the hardware, such as the implementation of SVX' and faster electronics, and the use of improved software and methodology in Run IB also help produce results with higher precision.

Our results give $b\bar{b}$ production cross sections consistent with those obtained in the Run IA analysis[74], but both results are consistently higher than the NLO QCD theory. The relative ratios between the cross sections with different quark p_T lower bounds, in both Run IA and Run IB, however, agrees with the NLO QCD theory well, that is the shape of the distribution is in good agreement with the predictions.

The other measurement, $\bar{\chi}$, taking into account of the uncertainties, agrees with the world average within two standard deviations. It should be noted that the world average is dominated by measurements at LEP operating at the Z^0 as is the value for the B_s fraction f_s . A larger value for $\bar{\chi}$ as found in the dimuon result presented in this thesis is not inconsistent with the known value for χ_d and the limits on χ_s and a somewhat larger fraction of B_s hadrons as has been measured in an analysis of CDF data.[75]

In Fermilab Run II, we expect to have an increase of an addition 20 times of luminosity and even more advanced hardware and software. Therefore, we expect that the next version of b production cross section and $\bar{\chi}$ measurement using Run II data will reveal more about the perturbative QCD as well as the whole Standard Model. In particular, the upgraded detector will have the capability to trigger on and fully reconstruct hadronic decay modes for both charm and bottom hadrons, so that measurements with a completely different set of systematics can be employed in understanding the mystery of the discrepancy between data and theory for hadronic production of charm and bottom. Additional statistics for measurements such as the one reported in this thesis and other related methods should also allow for tests of the QCD predictions for correlations in $b\bar{b}$ production (*e.g.* transverse opening angle) which can be helpful in understanding the relative importance of specific parton interactions[31].

Appendix A

The Maximum Likelihood Fitting Method and Smoothing Technique used in the Impact Parameter Fitting Method

A.1 The Choice of Impact Parameter Fitting Method

In our impact parameter fitting method, we need to find the optimum fractions, c_i 's, in the model:

$$f_{\mu\mu} = c_0 \times f_{bb} + c_1 \times f_{cc} + c_2 \times f_{jj} + c_3 \times f_{bj} + c_4 \times f_{cj} \quad (\text{A.1})$$

where $f_{\mu\mu}$ is the dimuon data IP distribution and the other f_* 's are the IP distributions of each of the components in the model (bb , cc , jj , bj , and cj). All the f 's are normalized and the constraint on the optimization is

$$c_0 + c_1 + c_2 + c_3 + c_4 = 1 \quad (\text{A.2})$$

To do the optimization, we have several methods to choose from:

1. Divide the data into bins and do a simple linear regression to obtain the c_i 's.

2. Divide the data into bins and do a χ^2 fit.
3. Divide the data into bins and do a maximum likelihood fit with the likelihood function:

$$L = \prod_i (l_i \times e^{-l_i} / n_i!) \quad (\text{A.3})$$

where

$$l_i = c_0 N_{bb} + c_1 N_{cc} + c_2 N_{jj} + c_3 N_{bj} + c_4 N_{cj} \quad (\text{A.4})$$

N_{**} 's are the number of events of each component in the i th bin and n_i is the actual number of dimuon events in the i th bin.

4. Do an unbinned likelihood fit as described in Chapter 4.

The first two methods would work well if our impact parameter distribution did not change dramatically in the measured range. However, the actual dimuon impact parameter distribution density has a difference of 10^4 times between the low IP region and high IP region. In this case, by using the first two methods, we underestimate the influence of the high IP region. Only by using the maximum likelihood fitting method can we account fully for the high IP region and have an unbiased estimation of the c_i 's.

The third method, like the first two methods, is based on dividing the impact parameter distribution region into equal or unequal-sized bins and using histograms based on the number of events falling in each bin to approximate the IP distributions. This method relies heavily on the art of binning. With too wide bins, we lose important statistical information within each bin. With too narrow bins, we encounter large statistical fluctuations which lead to large uncertainties in the final results. We also lose geometric correlation information by using narrow bins in the fit.

The unbinned likelihood fitting method does not rely on binning. It uses the full statistical information provided by the dimuon data. Also its likelihood function accounts fully for both the low IP region and the high IP region. Therefore we have chosen the unbinned likelihood fitting method as our impact parameter fitting method.

A.2 Motivation for Smoothing

In our unbinned likelihood impact parameter fitting, there is a very important step: we need to get a smooth distribution function from the Monte Carlo results.

The Monte Carlo results for a one-dimensional IP distribution, due to the low statistics in the high-IP area, is not smooth and has statistical fluctuations, especially around bins with only a few events (high IP region). If we were to use the binned likelihood fit without smoothing the IP distribution as the previous analysis (Run IA) did [1], we would have to generate the IP distribution histogram by creating equal-sized IP bins and count the number of events in each bin. The disadvantage of doing this is that the distribution becomes a step function with nontrivial fluctuations over the IP spectrum as shown in Figure A.1. These non-physical effects in the IP distribution can cause systematic uncertainties to the IP fitting method and our final calculations. Also, the important statistical information within the IP bins is wasted. We therefore need to find a better way to fully use the Monte Carlo data and have a more physical estimation of the distributions in the high-IP area.

A.3 The Smoothing Technique

To estimate a given function $y = f(x)$, we make N measurements and have N pairs of data (X_i, Y_i) with $i = 1 \dots n$. Assume the uncertainty in the i th measurement is ϵ_i . We have:

$$Y_i = f(X_i) + \epsilon_i, (i = 1 \dots N) \quad (\text{A.5})$$

There are many ways to derive an estimation $\hat{f}(x)$. We can express the function $\hat{f}(x)$ as a simple histogram (step function) or a linear interpolation between the neighbouring points. Or, based on a theoretical model, we can assume a multi-parameter function and fit the data to the model to estimate these parameters. [76] However, when we know no adequate parametric model to which $f(x)$ belongs, nonparametric methods can provide reliable estimation tools. Although we could calculate the IP distribution of muons from B mesons in the ideal environment (shown in Equation

A small section of b muon IP Distribution

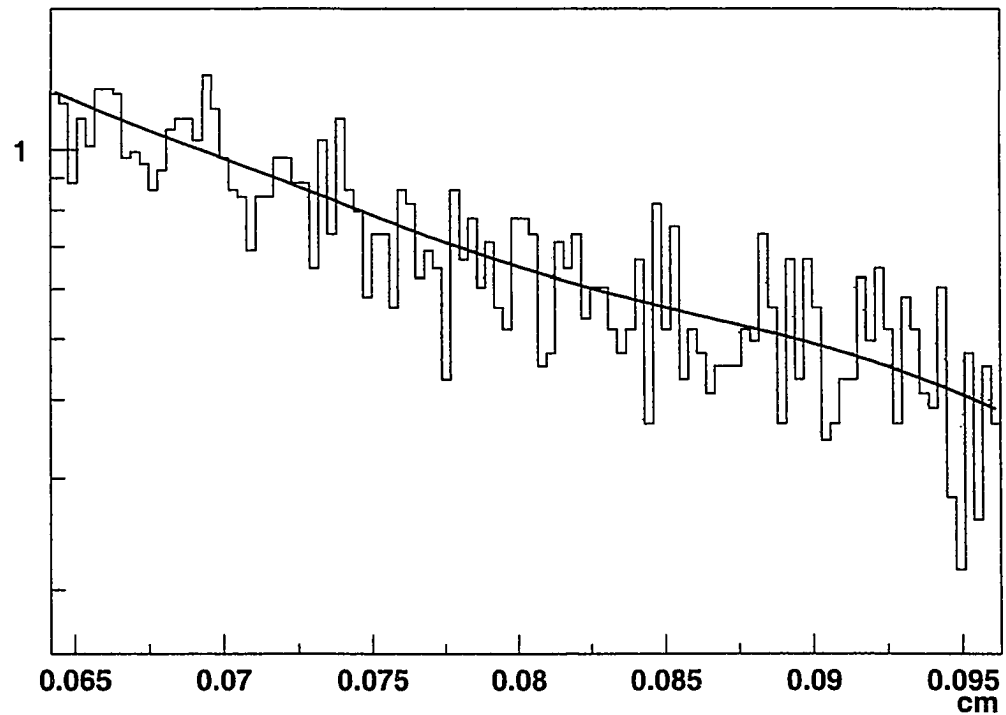


Figure A.1: This is a small section of our $b\bar{b}$ dimuon histogram sample (magnified). We can see there are statistical fluctuations in the bins. These fluctuations are more obvious when we go to higher IP or smaller bins. The smoothing technique makes better use of our knowledge of the physical distribution and provides a better approximation of the IP distribution.

4.4), the Monte Carlo results we obtain can not be approximated with a simple analytic function. That is due to the nonuniformity in the geometric coverage of the detector, non-linearity in the subsystem efficiencies and other experimental factors. We therefore choose to use a non-parametric estimator.

There are several non-parametric models to choose from: Nadaraya-Watson, k -th Nearest Neighbour, Spline Estimators, Gasser-Müller, Local Polynomial, Local Parametric, etc. Our smoothing technique is derived from the Nadaraya-Watson Kernel Smoothing method. The basic idea of kernel smoothing method is to use a weighted average of the Y_i 's close to the estimation point x :

$$\hat{f}(x) = (\sum_{i=1}^n Y_i K(\frac{x - X_i}{b})) / \sum_{i=1}^n K(\frac{x - X_i}{b}) \quad (\text{A.6})$$

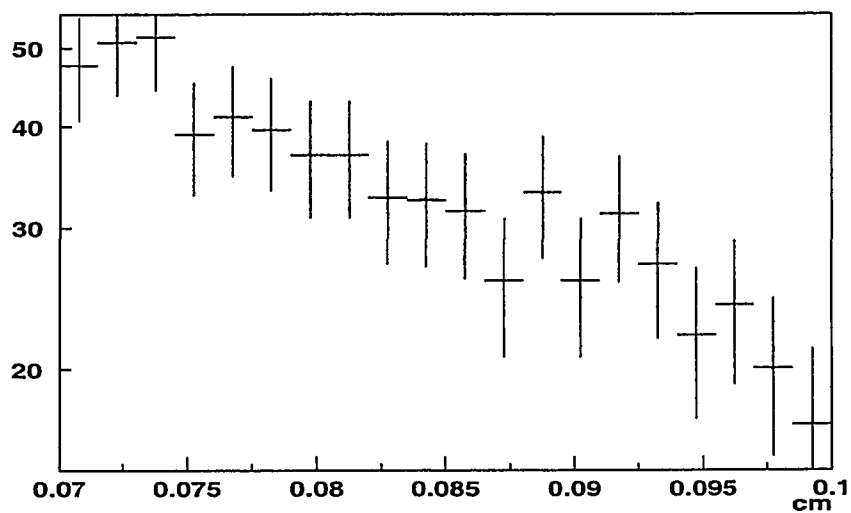
Here $K(x)$ is called the Kernel Function. b is called the Kernel Width, which is in fact the variation of $K(x)$. Which kernel function to choose depends on the application. Some literature suggests that the choice of kernel function shapes do not affect the final results significantly. We use a normal distribution as our Kernel Function.

The other factor, b , is more important. Around regions where the second derivative $f''(x)$ is large, the estimation has non-trivial systematic uncertainties due to the symmetric properties of the kernel functions. We need to choose small b 's in such regions. In our analysis, the b 's are manually chosen.

Another technique we used in the smoothing is to use $\log(Y)$ instead of Y in the estimations. As mentioned earlier in this chapter, the difference in f between the high IP region and low IP region could be up to 10^4 times. By taking the logarithm of f , we obtain a distribution that is closer to a linear distribution. This new distribution has relatively small second order derivative and causes less systematic uncertainties for the smoothing.

Figure A.2 is a diagram of the smoothing process. The result of the process is the curve shown in Figure A.1. The curve is later used in the unbinned likelihood fitting method.

A small section of b muon IP Distribution



Use the Gaussian Kernel to smooth the function.

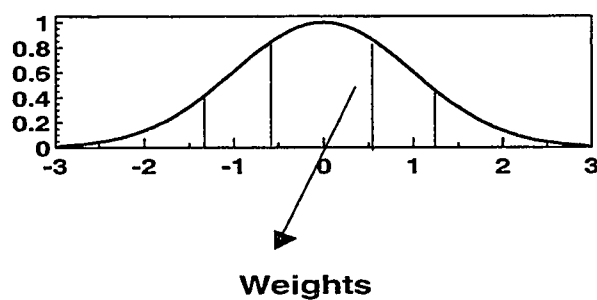


Figure A.2: The way we do the smoothing is to take a weighted average of the neighbouring Y_i 's. The weights are chosen to be of a Gaussian shape.

Appendix B

My participation in the CDF experiment

1

I started working for the CDF experiment during the summer of 1998. It was a time when Run I had finished two years before while Run II was still under construction. Although my thesis is based on the CDF Run I data, I also had the opportunity to participate in the construction and a part of the run of the Run II experiment. My contribution to the CDF Run II experiment, besides running shifts before and during the run, focuses on a software package named Trigger Manager (TM).

The Trigger Manager is a software module that lies between the Trigger Supervisor and the Scanner Manager in the trigger system. Figure 3.14 shows the Run I trigger system but has a similar structure as Run II. We can see from Figure 3.14 the position of TM in the whole trigger system. The main purpose of the Trigger Manager is to pass trigger information between 8 Trigger Supervisors and 1 Scanner Manager. The other purposes of Trigger Manager include monitoring of the events and performing certain run-control functions.

Figures B.1 and B.2 are the demonstration of the communication protocol between the Trigger Manager and the Scanner Manager. During a normal run, the Trigger

¹This chapter is not related to our analysis and was added per the request of the thesis defense committee.

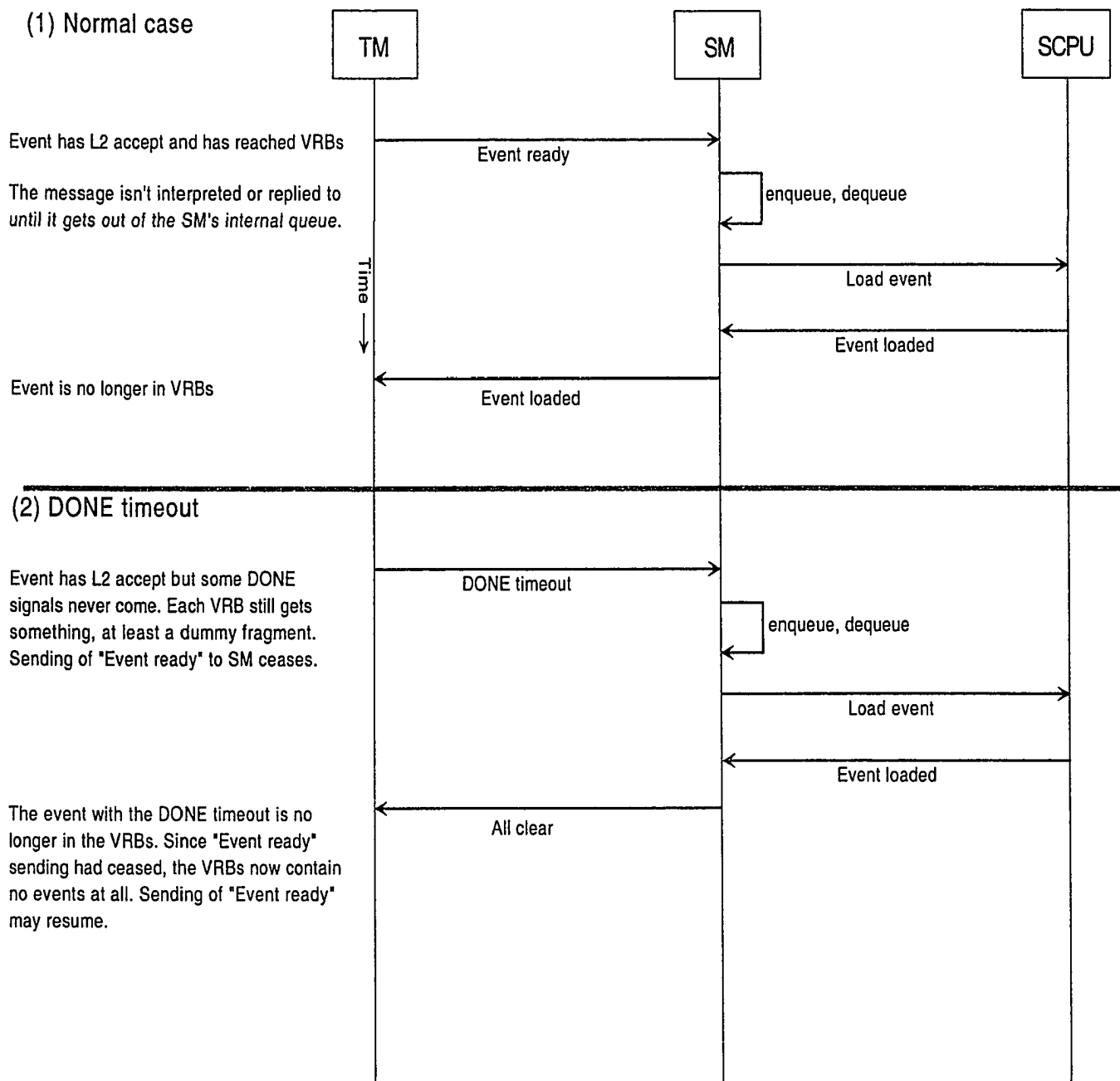


Figure B.1: The protocol between the Trigger Manager and the Scanner Manager.
(1)

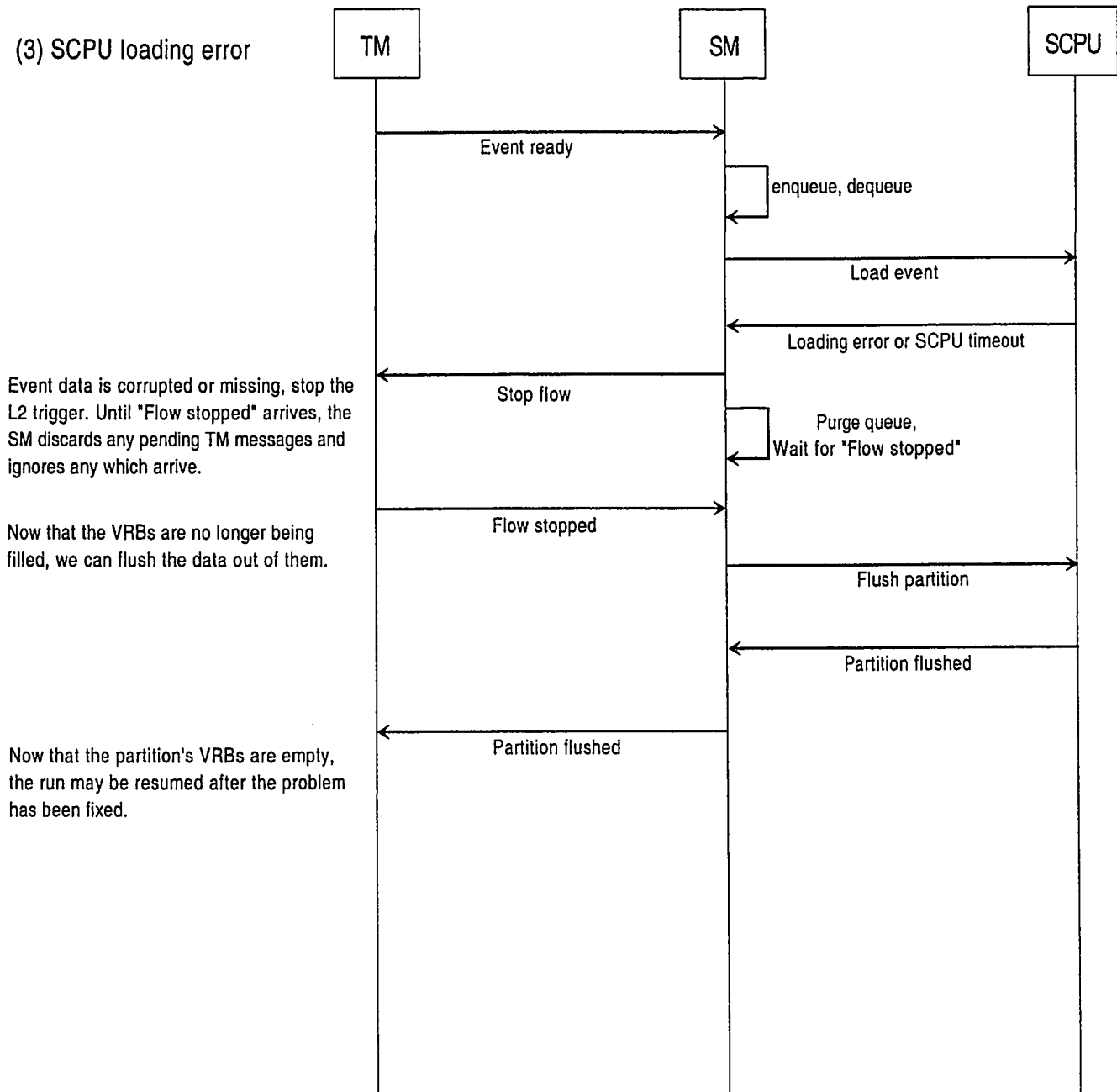


Figure B.2: The protocol between the Trigger Manager and the Scanner Manager.
(2)

Manager collects “Event Ready” information from the 8 Trigger Supervisors and parses the information to a readable format before sending it to the Scanner Manager. The Scanner Manager receives the “Event Ready” information, processes it, and replies with a “Event Loaded” to the TM and finishes the cycle. However, when there are abnormalities in the run such as a timeout or a scanner CPU loading error, the Trigger Manager and the Scanner Manager needs to respond to such cases and make certain communications with other parts of the system.

The other important functions of the TM are its monitoring of the trigger system and usage in run-control. The TM keeps records of the numbers of normal events, events with timeout, and events with SCPUs errors, etc. These numbers are readable through a Java interface or through a run-control interface. When the operator of the experiment sees abnormalities in the events, he can decide to pause or stop the current run. In such situations, the TM can be controlled from the run-control panel and halts or resumes the data flow.

The Trigger Manager is an important part of the trigger system and is currently running in the CDF Run II experiment when this thesis is being written.

Bibliography

- [1] I. Yu, Ph.D. Thesis (1995).
- [2] ALEPH *et al.*, SLAC-PUB-8492 (2000).
- [3] S. Holmes, Fermilab-conf-87/160 .
- [4] M. Gell-Mann and A. Pais, Phs. Rev. **97**, 1387 (1955).
- [5] K. Lande *et al.*, Phs. Rev. **103**, 1901 (1956).
- [6] R. Feynman, Phs. Rev. Lett. **23**, 1415 (1969).
- [7] J. Bjorken, Phs. Rev. **179**, 1547 (1969).
- [8] M. Mangano *et al.*, Nucl. Phys. **B373**, 295 (1992).
- [9] Laozi, *Dao De Jing (The Bible of Taoism)* (China, 500 B.C.).
- [10] J. Ellis, [arXiv:hep-ph/0110192v1](#), (2001).
- [11] E. Farhi and L. Susskind, Phys. Rept. **74**, 277 (1981).
- [12] K. D. Lane, [arXiv:hep-ph/0007304](#), 277 (2000).
- [13] L. Everett, G. Kane, S. Rigolin, and L. Wang, Phys. Rev. Lett. **86**, 3484 (2001).
- [14] http://www.cap.bnl.gov/mumu/mu_home_page.html, .
- [15] J. Ellis *et al.*, [arXiv:hep-ph/0007304](#), .
- [16] J. Collins and D. Soper, Ann. Rev. Nucl. Part. Sci. **35**, 107 (1985).

- [17] P. Nason, S. Dawson, and R. Ellis, Nucl. Phys. **B237**, 49 (1988).
- [18] CDF Collaboration, Phys. Rev. Lett. **71**, 500 and 2396 (1993).
- [19] CDF Collaboration, Phys. Rev. Lett. **75**, 1451 (1995).
- [20] D0 Collaboration, Phys. Lett. **B487**, 264 (2000).
- [21] CDF Collaboration, Phys. Rev. **D65**, 052005 (2002).
- [22] C. Albajar *et al.*, Phys. Lett. B **256**, 121 (1991).
- [23] C. Albajar *et al.*, Z. Phys. C **61**, 41 (1994).
- [24] C. Albajar *et al.*, Phys. Lett. B **369**, 46 (1996).
- [25] P. Nason, S. Dawson, and R. Ellis, Nucl. Phys. **B 327**, 49 (1989).
- [26] P. Nason, S. Dawson, and R. Ellis, Nucl. Phys. **B 335**, 260 (1989).
- [27] CDF Collaboration, Phys. Rev. **D66**, 032002 (2002).
- [28] S. Frixione, M. Mangano, P. Nason, and G. Ridolfi, hep-ph/ **9702287**, (1997).
- [29] P. Nason *et al.*, hep-ph/ **0003142**, (1999).
- [30] M. Cacciari and P. Nason, Phys.Rev.Lett. **89**, 122003 (2002).
- [31] R. Field, Phys. Rev. **D65**, 094006 (2002).
- [32] Particle Data Group, Particle Physics Booklet (2000).
- [33] M. Kobayashi and T. Maskawa, Prog. Theor. Phys. **49**, 652 (1973).
- [34] L. Wolfenstein, Phys. Rev. Lett. **51**, 1945 (1984).
- [35] A. Ali and D. London, CERN-TH-94-7408 (1994).
- [36] D. Buskulic *et al.*, Phys. Lett. B **322**, 441 (1994).
- [37] D. Buskulic and *etal.*, Phys. Lett. B **313**, 498 (1993).

- [38] R. Akers and et al, Phys. Lett. B **327**, 441 (1994).
- [39] R. Akers and et al, Phys. Lett. B **336**, 585 (1994).
- [40] P. Abreu and et al, Phys. Lett. B **338**, 409 (1994).
- [41] J. Bartelt and et al, Phys. Lett. B **71**, 1680 (1993).
- [42] ALEPH Collab., Z. Phys. **C75**, 397 (1997).
- [43] DELPHI Collab., Z. Phys. **C76**, 579 (1997).
- [44] L3 Collab., Eur. Phys. J. **C5**, 195 (1998).
- [45] OPAL Collab., Z. Phys. **C72**, 377 (1996).
- [46] OPAL Collab., Z. Phys. **C76**, 401 (1997).
- [47] ALEPH Collab., Eur. Phys. J. **C4**, 367 (1998).
- [48] CDF Collab., Phys. Rev. Lett. **82**, 3576 (1999).
- [49] DELPHI Collab., Phys. Lett. **B414**, 382 (1997).
- [50] OPAL Collab., Eur. Phys. J. **C11**, 587 (1999).
- [51] SLD Collab., SLAC-PUB **8225**, (1999).
- [52] Fermi National Accelerator Lab, <http://www.fnal.gov>.
- [53] D. Patternson, Fermilab Internal Note (1986).
- [54] J. Thompson, Fermilab-TM-1901 (1994).
- [55] H. Minemura *et al.*, Nucl. Instrum. and Methods Phys. Res. **A238**, 18 (1985).
- [56] W. Badget *et al.*, CDF Internal Note 2527 (1994).
- [57] L. Balka *et al.*, Nucl. Instrum. Methods **A267**, 301 (1988).

- [58] CDF Collaboration, *The Collider Detector at Fermilab* (Nucl. Instr. and Meth. A., North-Holland, 1988).
- [59] F. James, MINUIT Reference Manual **D506**, .
- [60] G. Foster *et al.*, Nucl. Instrum. Methods **A269**, 93 (1988).
- [61] C. Gay *et al.*, CDF Note **3751**, .
- [62] S. P. PAPPAS, CDF Note **3537**, (1996).
- [63] P. Sphicas, CDF Note **2655**, .
- [64] G. Feild *et al.*, CDF Note **5027**, .
- [65] A. Clark *et al.*, CDF Note **3715**, .
- [66] G. Feild, J. Lewis, and M. Schmidt, CDF Note **4769**, .
- [67] T. A. Keaffaber *et al.*, CDF Note **4768**, .
- [68] T. LeCompte and J. Lewis, CDF Note **2588**, .
- [69] T. LeCompte, CDF Note **2700**, .
- [70] C. Anway-Wiese, CDF Note **1986**, .
- [71] C. Gay *et al.*, CDF Note **3791**, (1996).
- [72] E. Berger *et al.*, hep-ph **0103145**, **0012001**, (2001).
- [73] G. Apollinari, P. Giromini, F. Happacher, and F. Ptohos, hep-ph **0103145**, **0012001**, (2001).
- [74] CDF Collaboration, Phys. Rev. **D55**, 2546 (1997).
- [75] CDF Collaboration, Phys. Rev. Lett. **84**, 1663 (2000).
- [76] A. Bowman and A. Axxalini, *Applied Smoothing Techniques for Data Analysis* (Oxford, London, 1997).



2017 ProQuest Distribution Agreement

This Agreement is between the author (Author) and ProQuest LLC, through its ProQuest Dissertation Distribution business (formerly ProQuest/UMI). Under this Agreement, Author grants ProQuest certain rights to preserve, archive and distribute the dissertation or thesis (the Work), abstract, and index terms provided by Author to ProQuest.

Section I. License for Inclusion of the Work in ProQuest Publishing Program

Grant of Rights. Author hereby grants to ProQuest the **non-exclusive**, worldwide right to reproduce, distribute, display and transmit the Work (in whole or in part) in such tangible and electronic formats as may be in existence now or developed in the future. Author further grants to ProQuest the right to include the abstract, bibliography and other metadata in the ProQuest Dissertations & Theses database (PQDT) and in ProQuest Dissertation Abstracts International and any successor or related index and/or finding products or services.

ProQuest Publishing Program - Election and Elements. The rights granted above shall be exercised according to the publishing option selected by Author in Section III, Author Options, and subject to the following additional Publishing Program requirements:

- **Distribution of the Work.** Except as restricted by Author in the publishing option selected, the rights granted by Author automatically include (1) the right to allow sale and distribution of the Work, in whole or in part, by ProQuest and its sales agents and distributors and (2) the right to make the Abstract, bibliographic data and any meta data associated with the Work available to search engines and harvesters.
- **Restrictions.** ProQuest will use commercially reasonable efforts to restrict the distribution of the Work as provided under the publishing option selected by Author or *as later elected by Author* through direct contact with ProQuest. Such election is subject to Author's Degree Granting Institution Directives. With respect to restrictions requested after submission of the Work, Author acknowledges that ProQuest cannot recall or amend previously distributed versions of the Work.
- **Removal of Work from the Program.** ProQuest may elect not to distribute the Work if it believes that all necessary rights of third parties have not been secured. Refer to the website http://www.proquest.com/products_umi/dissertations/ for information about copyright and your dissertation or thesis. If Author's degree is rescinded, and/or the degree-granting institution so directs, ProQuest will expunge the Work from its publishing program in accordance with its then current publishing policies.
- **Degree Granting Institution Directives.** Author is solely responsible for any conflict between policies and directions of Author's degree-granting institution, Author's choice of publishing model, and/or any restriction Author places on the use of the Work. For the avoidance of doubt, ProQuest is not responsible for access to the Work that is provided by Author's degree-granting institution through its library or institutional repository. Author must work directly with Author's degree granting institution to ensure application of any restrictions to access relating to the Work by Author's degree granting institution.

Delivery of the Work. Author shall provide to ProQuest the Work and all necessary supporting documents during the online submission process, according to the Instructions accompanying this agreement.

Rights Verification. Author represents and warrants that Author is the copyright holder of the Work and has obtained all necessary rights to permit ProQuest to reproduce and distribute third party materials contained in any part of the Work, including all necessary licenses for any non-public, third party software necessary to access, display, and run or print the Work. Author is solely responsible and will indemnify ProQuest for any third party claims related to the Work as submitted for publication.

Open Access Publishing Plus

- ✓ I want the broadest possible dissemination of my work, and I want to provide free global access to the electronic copy of my work via the internet.
- ✓ I understand that I will not be eligible to receive royalties.

I want major search engines (e.g. Google, Yahoo) to discover my work. Learn more: <http://www.proquest.com/en-US/products/dissertations/google.shtml>

- ✓ Yes
- No

Acknowledgment: I have read, understand and agree to this ProQuest Publishing Agreement, including all rights and restrictions included within the publishing option chosen by me as indicated above.

REQUIRED Author's

signature_____

Date_____8/9/17_____

(Print Name) _____Zhaoou Yu_____

Institution conferring degree _____Yale University_____

This page must accompany your manuscript and the rest of the submission materials

Please check type of manuscript:

Dissertation/Master’s Thesis Submission Form

Please print clearly in block letters

___ M (Master’s Thesis)

___ D (Dissertation)

Personal Information

Last Name _____YU_____

Middle Name or Initial _____

First Name _____Zhaoou_____

Country (ies) of Citizenship _____

Degree & Dissertation Information

Title of Dissertation/ Thesis _____

Institution conferring degree _____

Degree awarded (abbreviate; e.g., Ph.D.) _____

College, School, or Division _____

Year degree awarded _____

Department or Program _____

Year manuscript completed _____

Advisor/Committee Chair _____

Committee Member	_____	Committee Member	_____
Committee Member	_____	Committee Member	_____
Committee Member	_____	Committee Member	_____

Language of manuscript _____

Primary Subject Category: Enter the 4-digit code and category name from the Subject Category Guide that most closely describes the area of your research. Code _____ Category _____

You may suggest two additional subject categories that may aid in the discovery of your work in our digital database.

Code _____ Category _____ Code _____ Category _____

Provide up to 6 keywords or short phrases for citation indices, library cataloging, and database searching.

Current Contact Information Current Email Address _____ zhaoou.yu@aya.yale.edu _____

Street Address _____ PO BOX 295, Pluckemin, NJ 07978 _____

Please provide your postal address if you are interested in receiving royalties on sales of your thesis.

City _____ Province _____ Daytime Phone _____ 201-490-9617 _____

Country _____ Postal Code _____ Evening Phone _____

Permanent Contact Information

Permanent Email Address _____ zhaoou.yu@aya.yale.edu _____

Street Address (line 1) _____ PO BOX 295, Pluckemin, NJ 07978 _____

City _____ Province _____ Future Phone _____

Country _____ USA _____ Postal Code _____ Alternate Future Phone _____

THIS PAGE MUST ACCOMPANY YOUR MANUSCRIPT AND THE REST OF YOUR SUBMISSION MATERIALS

Subject Categories

The ProQuest Dissertations & Theses (PQDT) database and the ProQuest citation indices are arranged by subject categories. Please select the one category below that best describes your field of research or creative work. You may add one or two additional categories on your submission form that will also be associated with your work as secondary subjects.

Arts, Business, Education, Humanities, and Social Sciences

AREA, ETHNIC, AND GENDER STUDIES

African American studies	0296
African studies	0293
American studies	0323
Asian American studies	0343
Asian studies	0342
Baltic studies	0361
Black studies	0325
Canadian studies	0385
Caribbean studies	0432
Classical studies	0434
East European studies	0437
Ethnic studies	0631
European studies	0440

French Canadian culture	0482
Gender studies	0733
GLBT studies	0492
Hispanic American studies	0737
Holocaust studies	0507
Islamic culture	0512
Judaic studies	0751
Latin American studies	0550
Middle Eastern studies	0555
Native American studies	0740
Near Eastern studies	0559
North African studies	0560
Pacific Rim studies	0561
Regional studies	0604
Scandinavian studies	0613
Slavic studies	0614
South African studies	0654

South Asian studies	0638
Sub Saharan Africa studies	0639
Women's studies	0453

BUSINESS

Accounting	0272
Arts management	0424
Banking	0770
Business	0310
Entrepreneurship	0429
Finance	0508
Management	0454
Marketing	0338
Sports management	0430

COMMUNICATIONS AND INFORMATION SCIENCES

Communication	0459
Information science	0723
Journalism	0391
Library science	0399
Mass communication	0708
Technical communication	0643
Web studies	0646

FINE AND PERFORMING ARTS

Art criticism	0365
Art history	0377
Cinematography	0435
Dance	0378
Design	0389
Film studies	0900
Fine arts	0357
Music	0413
Performing arts	0641
Theater	0465
Theater history	0644

EDUCATION

Adult education	0516
Art education	0273
Bilingual education	0282
Business education	0688
Community college education	0275
Continuing education	0651
Curriculum development	0727
Early childhood education	0518
Education	0515
Education finance	0277
Education policy	0458
Educational administration	0514
Educational evaluation	0443
Educational leadership	0449
Educational psychology	0525
Educational technology	0710
Educational tests & measurements	0288
Elementary education	0524
English as a second language	0441
Foreign language instruction	0444
Gifted education	0445
Health education	0680
Higher education	0745
Higher education administration	0446
History of education	0520
Home economics education	0278
Industrial arts education	0521
Instructional design	0447
Language arts	0279
Mathematics education	0280
Middle school education	0450
Multicultural education	0455
Music education	0522
Pedagogy	0456
Performing arts education	0457
Philosophy of education	0998
Physical education	0523
Reading instruction	0535
Religious education	0527
School counseling	0519
Science education	0714
Secondary education	0533
Social sciences education	0534
Sociology of education	0340
Special education	0529
Teacher education	0530
Vocational education	0747

HUMANITIES

HISTORY

African history	0331
American history	0337
Ancient history	0579
Asian history	0332
Black history	0328
Canadian history	0334
European history	0335
History	0578
History of Oceania	0504
History of science	0585
Latin American history	0336
Medieval history	0581
Middle Eastern history	0333
Military history	0772
Modern history	0582
Russian history	0724
World history	0506

LANGUAGE & LITERATURE

African literature	0316
American literature	0591
Ancient languages	0289
Asian literature	0305
British and Irish literature	0593
Canadian literature	0352
Caribbean literature	0360
Classical literature	0294
Comparative literature	0295
English literature	0593
French Canadian literature	0355
Germanic literature	0311
Icelandic & Scandinavian literature	0362
Language	0679
Latin American literature	0312
Linguistics	0290
Literature	0401
Literature of Oceania	0356
Medieval literature	0297
Middle Eastern literature	0315
Modern language	0291
Modern literature	0298
Rhetoric	0681
Romance literature	0313
Slavic literature	0314

PHILOSOPHY AND RELIGION

Aesthetics	0650
Biblical studies	0321
Canon law	0375
Clerical studies	0319
Comparative religion	0618
Divinity	0376
Epistemology	0393
Ethics	0394
Logic	0395
Metaphysics	0396
Pastoral counseling	0397
Philosophy	0422
Philosophy of Religion	0322
Philosophy of science	0402
Religion	0318
Religious history	0320
Spirituality	0647
Theology	0469

LAW AND LEGAL STUDIES

Alternative dispute resolution	0649
Intellectual property	0513
International law	0616
Law	0398
Patent law	0562

SOCIAL SCIENCES

Archaeology	0324
Area planning and development	0341
Criminology	0627
Cultural anthropology	0326
Demography	0938
Economic history	0509
Economic theory	0511
Economics	0501
Economics, Commerce-Business	0505
Economics, Labor	0510
Folklore	0358
Forensic anthropology	0339
Geography	0366
Individual & family studies	0628
International relations	0601
Labor relations	0629
Military studies	0750
Organization theory	0635
Organizational behavior	0703
Peace studies	0563
Physical anthropology	0327
Political Science	0615
Public administration	0617
Public policy	0630
Recreation and tourism	0814
Social research	0344
Social structure	0700
Social work	0452
Sociolinguistics	0636
Sociology	0626
Transportation planning	0709
Urban planning	0999

INTERDISCIPLINARY

Alternative energy	0363
Biographies	0304
Climate change	0404
Cultural resources management	0436
Energy	0791
Food science	0359
Home economics	0386
Information technology	0489
Multimedia	0558
Museum studies	0730
Sustainability	0640
Textile research	0994
Wood sciences	0746

Behavioral, Natural, and Physical Sciences**AGRICULTURE**

Agriculture	0473
Agronomy	0285
Animal diseases	0476
Animal sciences	0475
Fisheries and aquatic sciences	0792
Forestry	0478
Horticulture	0471
Plant pathology	0480
Plant sciences	0479
Range management	0777
Soil sciences	0481
Urban forestry	0281
Wildlife management	0286

ARCHITECTURE

Architecture	0729
Architectural engineering	0462
Landscape architecture	0390

BEHAVIORAL SCIENCES

Animal behavior	0602
-----------------	------

Behavioral sciences	0384
Clinical psychology	0622
Cognitive psychology	0633
Counseling psychology	0603
Developmental psychology	0620
Experimental psychology	0623
Occupational psychology	0624
Personality psychology	0625
Physiological psychology	0989
Psychobiology	0349
Psychology	0621
Quantitative psychology and psychometrics	0632
Social psychology	0451

BIOLOGICAL SCIENCES

Biochemistry	0487
Bioinformatics	0715
Biology	0306
Biomechanics	0648
Biophysics	0786
Biostatistics	0308

Cellular biology	0379
Developmental biology	0758
Endocrinology	0409
Entomology	0353
Evolution & development	0412
Genetics	0369
Histology	0414
Limnology	0793
Microbiology	0410
Molecular biology	0307
Morphology	0287
Neurosciences	0317
Parasitology	0718
Physiology	0719
Plant biology	0309
Systematic biology	0423
Virology	0720
Zoology	0472

ECOSYSTEM SCIENCES

Ecology	0329
Macroecology	0420
Paleoecology	0426

ENGINEERING

Aerospace engineering	0538
Artificial intelligence	0800
Automotive engineering	0540
Biomedical engineering	0541
Chemical engineering	0542
Civil engineering	0543
Computer engineering	0464
Computer science	0984
Electrical engineering	0544
Engineering	0537
Geological engineering	0466
Geophysical engineering	0467
Geotechnology	0428
Industrial engineering	0546
Mechanical engineering	0548
Mining engineering	0551
Naval engineering	0468
Nanotechnology	0652
Nuclear engineering	0552
Ocean engineering	0547
Operations research	0796
Packaging	0549
Petroleum engineering	0765
Plastics	0795
Robotics	0771
System science	0790

ENVIRONMENTAL SCIENCES

Conservation biology	0408
Environmental economics	0438
Environmental education	0442
Environmental engineering	0775
Environmental geology	0407
Environmental health	0470
Environmental justice	0619
Environmental law	0439
Environmental management	0474
Environmental philosophy	0392
Environmental science	0768
Environmental studies	0477
Land use planning	0536
Natural resource management	0528
Water resources management	0595
Wildlife conservation	0284

**MATHEMATICAL AND
PHYSICAL SCIENCES**

Acoustics	0986
Analytical chemistry	0486
Applied mathematics	0364
Astronomy	0606

GEOSCIENCES

Aeronomy	0367
Atmospheric chemistry	0371
Atmospheric sciences	0725
Biogeochemistry	0425
Biological oceanography	0416
Chemical oceanography	0403
Continental dynamics	0406
Geobiology	0483
Geochemistry	0996
Geographic information science and geodesy	0370
Geology	0372
Geomorphology	0484
Geophysics	0373
Hydrologic sciences	0388
Marine geology	0556
Meteorology	0557
Mineralogy	0411
Paleoclimate science	0653
Paleontology	0418
Petroleum geology	0583
Petrology	0584
Physical geography	0368
Physical oceanography	0415
Planetology	0590
Plate tectonics	0592
Remote sensing	0799
Sedimentary geology	0594

**HEALTH AND MEDICAL
SCIENCES**

Aging	0493
Alternative medicine	0496
Audiology	0300
Dentistry	0567
Epidemiology	0766
Gerontology	0351
Health care management	0769
Health sciences	0566
Immunology	0982
Kinesiology	0575
Medical ethics	0497
Medical imaging and radiology	0574
Medicine	0564
Mental health	0347
Nursing	0569
Nutrition	0570
Obstetrics and gynecology	0380
Occupational health	0354
Occupational therapy	0498
Oncology	0992
Ophthalmology	0381
Osteopathic medicine	0499
Pathology	0571
Pharmaceutical sciences	0572
Pharmacology	0419
Physical therapy	0382
Public health	0573
Public health occupations education	0500
Speech therapy	0460
Surgery	0576
Toxicology	0383
Veterinary medicine	0778

Astrophysics	0596
Atomic physics	0748
Chemistry	0485
Condensed matter physics	0611
Electromagnetics	0607
High temperature physics	0597
Inorganic chemistry	0488
Low temperature physics	0598
Materials science	0794
Mathematics	0405
Mechanics	0346
Molecular chemistry	0431
Molecular physics	0609
Nanoscience	0565
Nuclear chemistry	0738
Nuclear physics	0756
Optics	0752
Organic chemistry	0490
Particle physics	0798
Physical chemistry	0494
Physics	0605
Plasma physics	0759
Polymer chemistry	0495
Quantum physics	0599
Statistics	0463
Theoretical mathematics	0642
Theoretical physics	0753